EXPERIMENTAL FRACTURE MECHANICS OF CEMENT BASED MATERIALS: A NEW METHODOLOGY FOR THE ACCURATE MEASUREMENT OF MATERIAL TOUGHNESS

Thiago Melo Grabois

Tese de Doutorado apresentada ao Programa de Pós-graduação em Engenharia Civil, COPPE, da Universidade Federal do Rio de Janeiro, como parte dos requisitos necessários à obtenção do título de Doutor em Engenharia Civil.

Orientadores: Romildo Dias Toledo Filho
Guilherme Chagas Corderio
Laurent Ponson

Rio de Janeiro
Outubro de 2016

EXPERIMENTAL FRACTURE MECHANICS OF CEMENT BASED MATERIALS: A NEW METHODOLOGY FOR THE ACCURATE MEASUREMENT OF MATERIAL TOUGHNESS

Thiago Melo Grabois

TESE SUBMETIDA AO CORPO DOCENTE DO INSTITUTO ALBERTO LUIZ COIMBRA DE PÓS-GRADUAÇÃO E PESQUISA DE ENGENHARIA (COPPE) DA UNIVERSIDADE FEDERAL DO RIO DE JANEIRO COMO PARTE DOS REQUISITOS NECESSÁRIOS PARA A OBTENÇÃO DO GRAU DE DOUTOR EM CIÊNCIAS EM ENGENHARIA CIVIL.

Examinada por:

Prof. Romildo Dias Toledo Filho, D.Sc.

Prof. Guilherme Chagas Cordeiro, D.Sc.

Prof. Laurent Ponson, Ph.D.

Prof. François Hild, Ph.D.

Prof. Luis Marcelo Marques Tavares, Ph.D.

Prof. Eduardo de Moraes Rego Fairbairn, D.Ing.

RIO DE JANEIRO, RJ – BRASIL
OUTUBRO DE 2016

Grabois, Thiago Melo

Experimental fracture mechanics of cement based materials: A new methodology for the accurate measurement of material toughness/Thiago Melo Grabois. – Rio de Janeiro: UFRJ/COPPE, 2016.

XVII, 108 p.: il.; 29, 7cm.

Orientadores: Romildo Dias Toledo Filho
Guilherme Chagas Corderio
Laurent Ponson

Tese (doutorado) – UFRJ/COPPE/Programa de Engenharia Civil, 2016.

Bibliography: p. 91 – 102.

1. fracture. 2. cement based materials. 3. toughness. 4. recycled inclusions. 5. construction and demolition waste. 6. crack propagation. I. Toledo Filho, Romildo Dias *et al.* II. Universidade Federal do Rio de Janeiro, COPPE, Programa de Engenharia Civil. III. Título.

Agradecimentos

Arquiteto de formação, e coração, encontrei no laboratório de estruturas e materiais da COPPE, um novo horizonte profissional na área da pesquisa científica. Mais espcificamente, em ciência dos materiais. Comecei essa jornada ainda no mestrado, aqui no mesmo laboratório, acreditando no potêncial da interdiciplinaridade para encontrar alternativas inteligentes para os novos desafios da arquiteura e engenharia contemporânea. Devo confessar que essa busca continua, que este trabalho aguçou ainda ainda mais minha curiosidade e meu interesse por diversas técnicas e disciplinas. Como resultado disso, além do acesso à excelente infraestrutura laboratorial e de alguns laboratórios parceiros na UFRJ, tive a oportunidade de fazer minha pesquisa em regime de doutorado sanduíche na *Université Pierre et Marie Curie* (UPMC), em Paris. Tudo isso me proporcionou experiências únicas, além do convívio com pessoas igualmente importantes, dentro e fora da esfera da pesquisa, que definitivamente devem ser lembradas e merecem todo o meu agradecimento.

Preciso começar agradecendo individualmente à meus orientadores e amigos, Romildo, Guilherme e Laurent, por aceitarem o desafio, pelo incentivo, pelo apoio e pela resposabilidade à mim dada para desenvolver esta pesquisa. Ao professor Romildo, especialmente, por seus conselhos e idéias instigantes que se refletem nos resultados obtidos desde os tempos de mestrado, além disso, me incentivou e deu suporte para participar de conferências internacionais e projetos de pesquisa, contribuindo ainda mais para meu crescimento como cientista. Posso dizer que é um privilégio trabalhar, desde 2010, com o Prof. Guilherme Cordeiro que além de ser meu "mentor científico" é um amigo, apoiando até em questões pessoais. Seus conselhos brilhantes sempre enriquecem nossas discussões, que são valiosas para o pleno desenvolvimento deste trabalho e de minha carreira. Enfim, agreadeço profundamente ao Prof. Laurent Ponson, pelo convite e pela cordial acolhida como membro de seu grupo de pesquisa no *Institut Jean le Ronde d'Alembert* na UPMC. Sua contribuição foi fundamental no desenvolvimento deste trabalho.

Sou particularmente grato à Nathalia, minha fiel companheira, pelo seu amor e apoio incondicionais durante nossa longa e duradoura jornada. Mais um trabalho se conclui, definitivamente, graças à sua presença em minha vida. Não posso deixar de agradecer à nossa pequena Maria Clara, nossa filha, que chegou em nossas vidas

nesse último ano, nos enchendo de alegria.

Não posso deixar de agradecer à meus pais, Gloria e Eduardo, pelo amor, carinho e dedicação na formação de seus filhos e por todo o apoio durante minha trajetória pessoal e profissional. Ao meu irmão, Marcos, pelo carinho e amizade.

A todos os amigos de laboratório (LabEst / NUMATS) na COPPE pela coloaboração e apoio prestados durante as atividades; em especial, aos companheiros Saulo, Fabrício, Marco e Visar pela sincera amizade construida ao longo desses anos. Também agradeço aos valisos compaheiros Otávio, Samantha e Camila. E aos colegas Bartosz, Iolanda, Dimas, Tina, Adriana, Andrielli, Marco Antonio, Oscar, Carol, Mayara, Tamara, Yassin, Alfredo e Florian.

A aluna Nathália, pelo seu esforço e apoio irrestrito durante todas as atividades de pesquisa. Aos demais alunos de iniciação cintifica com os quais tive o prazer de trabalhar em diversos assuntos de pesquisa em engenharia civil, Juliana, Renata, Pedro e Kathelyn.

Particularmente, durante minha jornada fazendo pesquisa na Paris VI, no ano de 2015, algumas pessoas foram fundamentais. Agradeço aos valisos amigos Julien pela amizade e acolhida inicial, além de sua futura esposa, Luciana. Ao querido Emilien por sua amizade desde o tempo em que esteve no Brasil, e sua acolhedora família. Aos colegas de laboratório, Bahrat, Geoffrey, Mehdi, Jan, David, Paul e Omar. Em especial agradeço ao grande amigo Aditya, com quem tive o privilégio de trabalhar no tema de minha tese, por seu apoio irrestrito e por nossas valiosas discussõe que contribuiram muito no desenvolvimento deste trabalho. Preciso agradecer aos meus vizinhos e e queridos amigos de *Maison du Brésil*; em especial, aos companheiros Daniel, Fabio, Fabio Cardoso, Rodrigo e Raphael. As queridas Priscila e Carine. Aos amigos Fabiano, Urbano, Marcos, Martha e aos casais Igor e Julia; e Rafael e Franscine.

Sou, também, particularmente grato ao Prof. François Hild por aceitar que eu fizesse parte de minha pesquisa no *Laboratoire de Mecaniqué et Technologie* na ENS Cachan, e principalmente pela cordial acolhida. Nesse tempo, tive o prazer de conhecer e trabalhar com o pesquisador Jan, à quem sou especialmente grato. Não poderia deixar de agradecer ao Rafeal Vargas, um aluno brasilerio que me ajudou incondicionalmente nesta etapa.

Ao CNPq pelo suporte que garantiu minha dedicação exclusiva ao doutorado. E à Capes pelo suporte durante todo o ano de 2015, em meu doutorado sanduíche, na França.

Resumo da Tese apresentada à COPPE/UFRJ como parte dos requisitos necessários para a obtenção do grau de Doutor em Ciências (D.Sc.)

EXPERIMENTOS EM MECÂNICA DA FRATURA APLICADOS À PASTAS DE CIMENTO: UMA NOVA METODOLOGIA DE DETERMINAÇÃO DA TENACIDADE DO MATERIAL

Thiago Melo Grabois

Outubro/2016

Orientadores: Romildo Dias Toledo Filho
Guilherme Chagas Corderio
Laurent Ponson

Programa: Engenharia Civil

Apresenta-se, nesta tese, uma metodologia experimental para caracterizar os fenômenos relacionados à fratura de materiais frágeis sob tensão. Em particular, objetiva-se entender os mecanismos que governam a propagação de fissura em materiais à base de cimento, ainda mais especificamente, quando modifca-se sua composição regular introduzindo micro particulas provenienetes da reciclagem de resíduos de construção e demolição (RCD). A primeira parte do estudo é dedicada à validação de um aparato experimental para uma nova geometria projetada usando corpos-de-prova de *tapered double cantilever beam* (TDCB). Inicia-se, assim, solucionando o problema geometricamente à partir do método dos elementos finitos. Em seguida, testes de fratura são realizados em amostras de polimetil-metacrilato (PMMA), um arquétipo de material visco-elástico. Enfim, um método que explora uma gama de velocidades para vários valores de energia de fratura em um único experimento é apresentado. À partir de técnicas experimentais para caracterizar os mecanismos de hidratação, a evolução da resistência à compressão e a estrutura porosa, a influência da inclusão de cada tipo de partícula na microestrutura das pastas de cimento é descrita apresentando sinais de atividade pozolânica para os resíduos originados de cerâmica vermelha, em contraponto aos rsíduos de concreto, que apresentaram semelhanças aos grãos de inertes de quartzo. Por fim, à partir da metodologia experimental de fratura, desenvolvida inicialmente, observa-se que a energia de fratura das pastas de cimento aumentou com a inclusão das diferentes partículas, o que foi ainda mais evidenciado pelas micro partículas não reativas.

Abstract of Thesis presented to COPPE/UFRJ as a partial fulfillment of the requirements for the degree of Doctor of Science (D.Sc.)

EXPERIMENTAL FRACTURE MECHANICS OF CEMENT BASED MATERIALS: A NEW METHODOLOGY FOR THE ACCURATE MEASUREMENT OF MATERIAL TOUGHNESS

Thiago Melo Grabois

October/2016

Advisors: Romildo Dias Toledo Filho
Guilherme Chagas Corderio
Laurent Ponson

Department: Civil Engineering

In this Thesis, we propose an experimental methodology to characterize fracture phenomena of brittle media in tension. In particular, our goal is to understand the mechanisms that govern crack propagation in cement based materials when modifying its regular composition with micro particles from recycled construction and demolition waste (CDW). The first part of the study is devoted to validate an experimental approach for the new geometry designed using tapered double cantilever beam (TDCB) specimens. Thus, we initiate solving the problem geometrically using finite element method, and then perform fracture tests on samples of Poly-methyl methacrylate (PMMA), an archetype of homogeneous visco-elastic material. We show a study that explores a range of velocities for different fracture energies in one single test. The remaining of the work is devoted to understand the effects of the partial substitution of cement (10% wt.) by micro particles of recycled CDW in the behavior of cement pastes. Using experimental techniques to characterize the hydration mechanisms, the strength development, and the pore structure; the influence of each type of inclusion in the microstructure of the pastes is firstly depicted, presenting signs of pozzolanic activity for the wastes from red ceramics, in contrast to particles of recycled concrete that shows similarities to inert particles of quartz. Finally, applying our fracture methodology to these cement pastes, we show that the fracture energy of cement pastes increases when substituting cement by different particles, which is even more highlighted by the inclusion of non reactive micro particles.

Contents

List of Figures **x**

List of Tables **xvi**

Introduction **1**

1 Context and motivation **3**

1.1 Fracture of brittle materials: The linear elastic fracture mechanics framework 4

1.2 The experience of fracture mechanics approach to cement based materials 10

1.3 Cement-based materials: Environmental concerns 13

2 A new methodology for the characterization of tensile fracture properties **20**

2.1 A review on mode I fracture test geometries 21

2.2 Numerical study of the modified tapered double cantilever beam . . . 24

2.3 Experimental implementation 31

2.3.1 Implementation of the method on PMMA 33

2.4 Alternative approaches for estimating material toughness and crack tip position 41

2.5 Concluding remarks 50

3 Hydration properties of cement pastes with recycled inclusions **52**

3.1 Materials and methods 53

3.1.1 Recycling procedure 53

3.1.2 Characterization of the supplementary cementitious materials (SCM) 55

3.1.3 Mix proportions and preparation of specimens 59

3.1.4 Methods of characterization of the hydration-related properties of cement pastes 59

3.2 Effect of the powders inclusion on the properties of cement pastes . . 62

3.3 Concluding remarks 68

4 Fracture Properties of cement pastes 70

4.1 Materials and methods 71
4.2 Fracture behavior of hardened cement paste 74
4.3 Effects of inert quartz particles inclusion 77
4.4 Effects of recycled concrete particles inclusion 80
4.5 Effects of recycled ceramic brick particles inclusion 81
4.6 Discussion 82

Conclusion 88

Bibliography 91

A An extension in the IDIC algorithm for out-of-plane motions 103

B Mix-design and mechanical characteristics of the recycled concrete beam 106

C Publications 108

List of Figures

1.1 Idealized solids description for fracture phenomena: flawless model submitted to external stress σ (a); plate containing an elliptical cavity subjected to uniform applied tension (b); and a static plane system, presenting crack extension. 4
1.2 The modes of rupture: mode I, opening; mode II, shearing; and mode III, tearing. 7
1.3 Local coordinates system in the vicinity of the crack tip. 8
1.4 Optical micrographs of C_3S paste hydrated for 14 days. The bright areas are the crack that appears to be largely in the C-S-H region. . . 12
1.5 Optical micrographs of C_3S paste thin slabs after fracture. Examples after 1 and 28 days hydration (left and right, respectively). The bright areas are CH-rich regions (Courtesy of Berger *et al.* 12
1.6 Construction and demolition waste collected by regions in tons/day (figure adapted from Panorama 2013. 16

2.1 Literature review of different geometries for mode I fracture. (a) Single Edge Notched Beam (SENB) in 3 point loading; (b) Compact Tension (CT); (c) Double Cantilever Beam (DCB); and (d) Double Torsion (DT). 22
2.2 The procedure for toughness measurement. 24
2.3 Tapered double cantilever beam specimen geometry and its dimensions. 25
2.4 Finite element mesh for the TDCB specimen. The upper half coarse mesh used for the analyses has $\sim$ 9x10^3 nodes and $\sim$ 1.8x10^4 dof (a). The fine mesh has $\sim$ 1.4x10^5 nodes and $\sim$ 2.5x10^5 dof; in (b) the deformed configuration after unit force applied in y direction; in (c) the refinement strategy closer to the initial crack tip position of the order of $1e^{-11}$mm and; (d) represents the mesh refinement surrounding the hole where the force is applied. 26

2.5 Variation of the normalized compliance with crack length. The white circles are the FE results, while the black solid line is the exponential fit of the compliance using Eq. (2.1), and black shade circles are obtained from the cyclic experiment presented in Fig. 2.6. 27
2.6 Experimental force-displacement curves for different loaded/unloaded states for the TDCB geometry. The inverse of the slope in the elastic limit gives the compliance which have been shown in Fig.2.5. 28
2.7 Figure shows the variation of the non-dimensional specimen compliance with non-dimensional crack length for different specimen geometries. The simulations are carried out for two different geometries with the same tapering angle α but with different l_x and h_1. Geometry 1 is represented by triangles and has dimensions $l_x = 90e_x, h_1 = 160e_y$ while geometry 2 is represented by circles with dimensions $l_x = 60e_x, h_1 = 120e_y$. The black solid line shows the exponential fit for geometry 2 and length $L = 400e_x$ 29
2.8 log-log representation of vertical displacements u_y as function of the position r as obtained from the FE simulation. Then K_I is calculated from the fit of this curve using Eq. (2.6) (see black solid line). The present example corresponds to a crack length of 36.5mm and gives $K_I = 22.8\text{MPa.m}^{1/2}$. 30
2.9 Variation of the non-dimensional elastic energy release rate g as a function of the crack length using different approaches. The figure is plotted for a specimen with $l_x = 22.5$mm, $L = 100$mm and $h_1 = 40$mm 31
2.10 Experimental test setup used to perform quasi-static fracture tests. The electromechanic machine was equipped with a load cell sensor of 1kN, and a clip gauge device of 5 mm maximum opening to measure the applied force and the crack opening displacement, respectively. . . 32
2.11 The different sharpening strategies for the initial notch preparation: razor blade prolongation (a); laser prolongation (b); and laser plus pre-load cracking (c). 32
2.12 Typical force-displacement curves for different experiments on PMMA specimens of initial crack length $c_{ini} = 37$mm. These examples show how different loading rate conditions affect the experimental data results. 34

2.13 Compliance method used to measure the crack position as a function of time. The bottom inset shows the experimentally measured compliance λ_{exp} normalized by Eb as function of time in solid blue line. For a given time t^*=400 s, we have a corresponding λ^*_{exp} highlighted by the red (∘). The top inset shows the the finite element solution of the compliance λ_{th} normalized by Eb *vs* crack length c (solid line). Comparing the position of λ^*_{exp} we can infer c^*_{exp} (red (∘)). The main panel shows in solid blue line the inferred data for c_{exp} as function of time. The red (∘) displays the position of the point corresponding to t^* and c^*_{exp}. 35
2.14 Energy release rate as function of crack length calculated from the area method and the full finite element based method for a specimen under external loading condition of $\dot{\delta} = 0.5\mu$m/s. 36
2.15 Diagram of energy release rate-crack speed ($G - \log v_)$ curve at slow crack propagation regime for brittle fracture. 37
2.16 Log-log representation of the average crack velocity as a function of the applied loading rate. The straight line corresponds to Eq. (2.12), where the parameters $c_0 = 0.021$, $\lambda_0 = 4.81$, and r = 0.8 were calculated from the finite element simulations while the values Gc = 380 J.m^{-2} and $E = 1.82$ GPa are the characteristic fracture energy and Young's modulus for the PMMA as measured in our experiments. The Equation (2.12) is applied in c = 60 mm while the characteristic crack speed for each test is obtained from an average of the instantaneous velocity over the range $37 \lesssim c \lesssim 70$ mm. 38
2.17 Comparison of the fracture response of the TDCB specimen of PMMA as predicted numerically from Eq. (2.15) using the crack growth law parameters G_{c0} = 1.98x10^3 and $\gamma = 0.204$ with the experimental measurements for $\dot{\delta} = 2.5\mu$m/s: $Fvs\delta$ in (a); c *vs* t in (b); v *vs* c in (c); and G *vs* c in (d). In (c) an analytic prediction of crack length according Eq. (2.2) is also displayed. The two thin dashed lines in each graph represent the 10% error bars in respect to the parameters of the numerical fit. 40
2.18 Error plot ϵ as function of the crack growth law parameters (left); and the contour representation of the error, where it is interpreted as heights with respect to the G_{c0}-γ plane (right). This procedure provides the parameters G_{c0} = 1.98x10^3 and $\gamma = 0.204$ used in Fig. 2.17 for a direct comparison between the numerically predicted and the experimentally measured fracture behavior of a TDCB specimen of PMMA at the imposed loading rate $\dot{\delta} = 2.5$ μm/s. 41

2.19 Picture example of a TDCB specimen lateral surface during crack propagation. We use here a transparent material, the PMMA, that enabled the application of this crack tip detection algorithm. Dashed line shows the region of interest selected for the analysis. 42
2.20 (a) Zoomed region of the zone surrounding the crack path. (b) gray level profile along the crack path. 43
2.21 Illustration of the crack tip detection algorithm. 44
2.22 Variation of crack length Δc as function of time for PMMA specimens tested at different loading rates. Comparison of c measured by image analysis, and by the compliance method. 44
2.23 Displacement fields for mode I and II: The ones related to rigid body translations ψ_0^I (a) and ψ_0^{II} (d); the stress intensity factors ψ_1^I (b) and $\psi_1^{II}(e)$; and the so called T-stress ψ_2^I (c) and rigid body rotation ψ_2^{II} (f). 47
2.24 Williams' fields ψ_{-1}^I (left) and ψ_{-1}^{II} (right) that shows the singularities close to the crack tip (image center). The amplitude of these terms vanishes when the crack tip is located at the proper position. 47
2.25 Stress intensity factor K_I and crack length at different loading phases after crack initiation vs. maximum order n in Williams' fields. 48
2.26 Crack length as function of time (a), stress intensity factor (b) and T-stress (c) as function of crack length obtained by IDIC and compared to the full FE methodology. 50

3.1 Construction components used to produce the mineral additions. Laboratory concrete beam (a), face brick (b), and hollow brick (c). . 54
3.2 X-ray diffraction pattern of the materials. Portland cement (a), recycled concrete (b), face brick (c), hollow brick (d), and quartz (e). . 57
3.3 SEM images of the materials: cement (a), recycled concrete (b), face (c) and hollow (d) bricks, and quartz particles (e). Magnification of 2000x. 58
3.4 Particle size distribution of cement and the supplementary cementitious materials. 58
3.5 Rate of heat flow evolution for a typical Portland cement pastes determined by isothermal conduction calorimetry. 60
3.6 Cylindrical samples setup for the 28 days compressive strength experiments: (i) wire connection to the data acquisition system, (ii) extensometer for longitudinal displacements measurement and, (iii) extensometers to measure the transversal displacements (a); Setup positioning of extensometers (on right). 61

3.7 Effect of the different powders inclusion on the hydration kinetics of Portland cement paste. Bottom inset shows in detail the transition from the induction to the acceleration period, and the top inset displays a zoom at the main peaks (2) and (3). The main panel display the whole heat flow up evolution to 50 hours. 64
3.8 Effect of the different powders inclusion on the released heat normalized by the amount of Portland cement at 23^{o}C up to 7 days. 64
3.9 Compresive strength evolution of cement pastes. Pastes with recycled concrete and bricks are confronted to the reference paste and to paste with inert quartz. 66
3.10 Compressive stress as function of axial and lateral strain of all cement pastes at 28 days. 67
3.11 Mercury intrusion porosimetry experimental results for all cement pastes. 68

4.1 Steel mold for cementitious TDCB specimen's preparation. In (a) an exploded view: where the dashed giding lines indicate the fixing screw points; (i) is the bottom base with pointing tip for notch's induction; (ii) the tapered sides; (iii) front and back sides; and (iv) two stainless steel pins for hole's preparation. (b) shows an inside view of the mold assembly. 71
4.2 Geometrical changes designed for cement paste specimens (all dimensions in mm): Fixed initial crack length of 36.5, hole with larger diameter of 12.4, and the two steel plates for clip gauge connection. Attention must be paid for the variability of Δ due to manual fixing. 72
4.3 Typical experimental F-δ curve of the reference cement paste loaded at a displacement rate of machine crosshead of 0.01 mm/min. Top right inset displays the crack length evolution as function of COD. . . 73
4.4 (a) A typical example of the rather straight crack path and surface of the cement pastes after fracture test in a TDCB specimen (a). (b) Irregular path chosen by the crack due to large defects presented in cement microstructure that lead to invalid experiments (b). 74
4.5 Fracture behavior of the reference paste. (a) Crack velocity as function of crack length, and (b) the variations of energy release rate with crack length. 76

4.6 SEM micrograph of an void into the reference cement paste microstructure. It highlights to the very complex system with the unhydrated cement particles (in light gray), a dense matrix composed by hydration products (dark gray), and in particular, a large void of about 100 μm of diameter (highlighted in the center) nucleating several microcracks. 77
4.7 Typical F-δ curve of the cement pastes with quartz powder inclusion in comparison to the reference paste. 78
4.8 Effects of the Portland cement's substitution by quartz on the variations of energy release rate G with crack length c. 79
4.9 Typical example of SEM image of the Portland cement paste with fine particles of quartz. Magnification of 200x (a) and 600x (b), image size of 1280 x 1040 px (8445 x 688 μm). Light gray areas are the unhydrated cement grains (c), dark gray regions are the quartz grains (q), dark (black) zones are voids, and the more homogeneous gray zone are the hydrated cement matrix. The red arrows point out a microcrack extending from the interface zone to the matrix. 79
4.10 Typical F-δ curve of the cement pastes with concrete waste powders in comparison with the cement paste with no inclusion. 80
4.11 Effects of the Portland cement's substitution by recycled concrete waste on the variations of energy release rate G with crack length c. . 81
4.12 Typical $F - \delta$ curves of the cement pastes with red ceramic powder inclusions in comparison with the reference mixture. The right inset displays the variations of crack length with crack opening displacements δ for all three pastes. 82
4.13 Effects of the Portland cement's substitution by recycled red ceramic bricks on the variations of energy release rate G with crack length c. . 83
4.14 Correlation between the toughness and strength of the cement pastes (Plotted results correspond to data of Tab. 4.3). ($\circ$) Reference; Quartz paste ($\bullet$); ($\square$) Concrete paste; ($\triangle$) Face brick paste; ($\triangledown$) Hollow brick paste. The slope of the dashed line is 1.7. 86

A.1 Description of the tilt rotations of a flat surface along $\underline{y}$ (right) and $\underline{x}$ (left). R^+ and R^- denotes the positive and negative angle region, respectively. 104

B.1 Beam production phases. From left to right: first, the regular prismatic beam; the reinforcement casting procedure; and finally, the strengthened beam completed (courtesy of Vaz). 106

List of Tables

1.1 Comparison between the experimental and theoretical strength of different materials. Of particular interest, the theoretical strength values of the cement-based materials are about 1000 times larger than the ones measured experimentally. 5

1.2 Fracture parameters for a short selection of brittle materials. Fracture energy G_{Ic}, and toughness K_{Ic} (data were extracted from the Ref., an exception for the PMMA data). 9

1.3 Quality requirements according Japanese standard for the use of recycled aggregate and recycled concrete aggregate. (Extracted from B.C.S.J). 15

2.1 Dimensions of the TDCB geometry used for the finite element simulation (in e_x) and their respective values (in mm) for the specimen adopted in the experimental analysis. 25

2.2 PMMA sheet general properties (information from the manufacturer). 33

3.1 Particle size d classification (in mm) and schematic description of the fractions generated by the crushing and homogenization process. The materials highlighted in bold are the ones to be investigated in the present work. 54

3.2 Physical characteristics of the materials: (ρ) Specific gravity; (BET) BET specific surface area; (d) D_{50} particle size. And the chemical composition (wt.%) in terms of oxides of the raw materials. 56

3.3 Compressive strength evolution with time of cement pastes (standard deviation values indicated within parenthesis). 65

3.4 Mechanical characteristics of cylinder specimens tested in compression at 28 days for all cement pastes (standard deviation values indicated within parenthesis). 67

3.5 Pore size classification from porosimetry results for the cement pastes - (gel) gel pores and hydrated phases; (M) medium capillary pores; (L) large capillary pores; (air) big capillary pores and air content; and (ϕ) the total porosity. 68

4.1 Summary of TDCB fracture experiments on Portland cement pastes: (y) means that test are valid; and (-) represents the discarded ones. . 74
4.2 Fracture energy (G_c) experimentally measured on TDCB specimens with the compliance method, and the rough determination of the fracture energy (G_c^A) as the total work of fracture determined from the area under the experimental $F - \delta_F$ curve. G_c is computed as the average of G in the reliable range of crack length $40 \leq c \leq 70$ mm for the specimens presented in figures 4.8, 4.11 and 4.13. 76
4.3 Parameters for calculating process zone size (l_{pz}) according Eq. (4.1): (K_{Ic}) Toughness; (σ_t) estimated splitting tensile stress (lower bound). We also highlight here the median size (d) of the particles of cement (common to all mixtures, displayed in the line corresponding to the Reference) and the inclusions in respect to each corresponding mixture. 85

B.1 Concrete mix proportions of reinforced beams in kg/m^3. Different aggregate size classes were used in each phase. Coarse aggregate with D_{max} of 9.5 mm (CA1) in beam phase, and coarse aggregate of D_{max} = 19 mm (CA2) in reinforced phase. Fine aggregates (FA) were the same for both phases. Data is a courtesy of Vaz. 107
B.2 Initial static properties of he concrete beams (courtesy of Vaz). 107
B.3 Concrete properties when reinforced beams were submitted to cyclic load and failure (courtesy of Vaz). 107

Introduction

Predicting and so preventing fracture is a central question in material science and structural engineering. A good assessment of the failure risk of a structure goes with the accurate determination of the mechanical properties like fracture toughness for materials involved in civil engineering applications.

Nowadays, cement based materials are increasingly more complex: (i) from structural engineering standpoint, new cement based composites [1] for high mechanical performance, extreme temperatures, and several others challenging applications have been developed; (ii) from an environment-friendly perspective, the cement and concrete industries have been pushed to pursue greener solutions that encourage us to reduce natural resources consumption and the volume of landfill disposal [2, 3]. Therefore, the impact of the microstructural variations on the fracture properties of these materials must be assessed precisely to ensure that it does not affect their performance.

Material fracture properties are highly sensitive to microstructural features. Indeed, stress singularity present at the crack tip vicinity may greatly enhance the effect of small scale heterogeneities of material on their macroscopic failure response. An important challenge though is to be able to characterize the impact of variations in the cement based composition on their macroscopic performance.

In this thesis, I have focused on the design of an experimental methodology that allows an accurate characterization of the fracture behavior of brittle solids in tension. I have used concepts from fracture mechanics in the characterization of civil engineering materials. The main goal is therefore to investigate the fracture parameters that govern the failure behavior of cement based materials. In particular, we design a study - theoretical and experimental - that explores a range of velocities for different energy release rate values in one single test and, eventually, understands the R-curve behavior (when toughness increases with crack extension). We will illustrate and validate our experimental approach on a synthetic polymer material that has the advantage to have well known fracture properties [4]. We will then apply our method to the characterization of regular cement pastes, and modified ones - containing powders coming from different construction and demolition wastes (CDW) and quartz. For both aspects of the project, we will realize experimental fracture

tests that allow us to characterize the materials' toughness and their variations with its composition and the cracking velocity.

At last, we could present a few promising results for fracture tests in cement based pastes with different inclusions as partial substitutes of cement, which brings promising perspectives for a greener civil engineering construction and building industry.

The present manuscript is organized into four chapters. In the first chapter, We give the context and motivation of this research project starting with the basis of fracture mechanics in brittle medium. This section is then, followed by an historical background about fracture studies in cement based materials. Finally, I review the panorama of the recycling of demolished structure as crucial solution for the cement and concrete industry. This introduces the reader to the two main subjects of this work: (i) fracture behavior of brittle materials and; (ii) environmental issues involving the industry of cement and concrete materials. Thus, setting the scene for the remainder of the manuscript.

The chapter 2 is devoted to the development of a fracture test methodology and its validation. But, we briefly review a few test geometries usually adopted for experimental investigations in mode I fracture before describe the whole method. Though we design a new geometry for mode I tensile fracture experiments and provide new insights on stable-unstable crack propagation of brittle material. This part of the project will help us to understand and interpret the results obtained on more traditional materials like cement pastes where the microstructure and heterogeneities are less controlled.

Chapter 3 is dedicated to present the cement pastes production and characterization. First, I expose the recycling procedure of the demolition waste as well as raw material properties. Then, the early hydration properties, the compressive strength behavior, and the pore structure of the cement pastes are assessed experimentally. This allow us to understand the new microstructural features developed in the presence of the powder inclusions.

Finally, in the fourth chapter, the failure properties of cement pastes with different powder inclusions is discussed. In particular, we analyze how heterogeneity introduced at the small scale in the microstructure of cement blends using recycled or inert powders affect and modify their resistance to crack propagation.

Chapter 1

Context and motivation

During the nineteenth century, structural engineers agreed that the failure of a material should occur when it stressed beyond some critical level. However, in the first years of the last century, this critical stress criterion became more questionable, and the first steps to understand materials failure were taken. Two remarkable studies were the ones of Grifitth [5], giving the basis to a solid framework of the present-day fracture mechanics, and its precursor in 1913, Inglis [6] that provided the first real insight into the mechanism of fracture in a solid. Based on an energy theorems of classical mechanics and thermodynamics, the Linear Elastic Fracture Mechanics (LEFM), developed all over the last century, brings a solid theoretical framework to describe how crack propagates in homogeneous solids. Nevertheless, this approach yet presents uncertainties on the fracture of heterogeneous ideal media; neglecting the role of its disorders - at macro and microscopic level - on crack propagation.

In spite of cracking of hardened cement paste and concrete, it was only about the early 60s that the concepts of fracture mechanics were finally applied to them. However, as we are talking about a highly complex and heterogeneous system [7], much controversy as to the real efficiency of LEFM principles to these solids still remains. Considering the many questions that yet exist about the precise nature of its cracking process it is comprehensible that no agreement as to which fracture mechanics criteria best characterize the failure of cement based materials, or which test methods are most suitable.

The possible effects caused on the behavior of cement blends by the inclusion of different micro-structural disorders are the central point of our investigation. After a brief introduction to the principles of fracture mechanics, we will review the topic focusing on the failure of cement based material, and briefly present the challenging questions about produce them with recycled construction and demolition waste for a greener civil engineering industry. This serves to introduce the reader to many of the basic concepts of fracture and link it with some of the most recent civil engineering

issues and thus to set the scene for the reminder of the manuscript.

1.1 Fracture of brittle materials: The linear elastic fracture mechanics framework

The pioneer work of Griffith [5] stated that: in an ideal elastic solid, the crack starts to grow when the energy released by the crack advance is sufficient to balance the energy needed to create new surfaces. Let us first describe an ideal situation, simply exemplified by a flawless solid (Fig. 1.1(a)) modeled as a network of springs of length a. The spring bonds stretch over the length $\delta a = a\sigma/E$, when submitted to an external stress σ. Assuming now, from quantum-mechanical calculations [8], that two adjacent atoms deforming from their original spacing a_0 at a relationship of $\delta a_0 = a/5$ break a bond, we have the critical stress at material failure equals to $\sigma = E/5$. When comparing this hypothetical application with experimental strengths in real materials (Table 1.1), the conclusion was that the strength of the materials were typically lower by two orders of magnitude. Of particular interest, the same comparison in cement based materials reveals three orders of magnitude, and only one order in PMMA. Therefore, it is clear that the bonding energies concept does not directly provide the materials' strength, and behind these huge discrepancies is the existence of flaws in real materials.

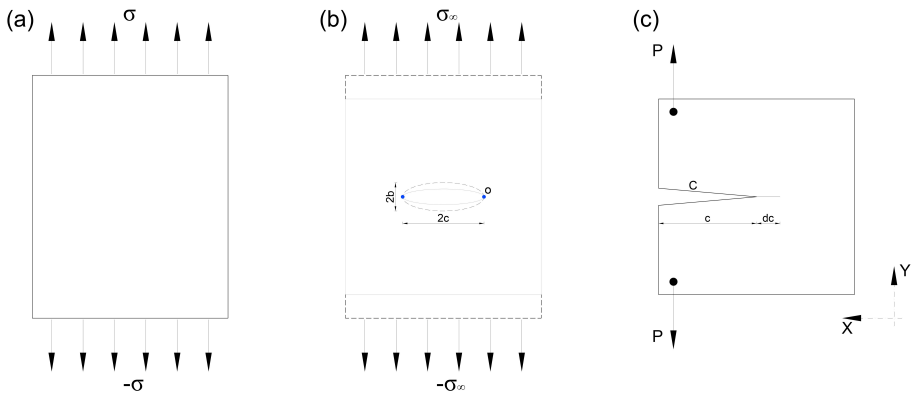

Figure 1.1: Idealized solids description for fracture phenomena: flawless model submitted to external stress σ (a); plate containing an elliptical cavity subjected to uniform applied tension (b); and a static plane system, presenting crack extension.

The theory of introduction of flaws

Now, changing the way to face the problem, the precursor work of Inglis [6] proposed the stress analysis of a solid introducing an elliptical cavity of semi-axes b < c in a uniformly stressed plate, *i.e.* Inglis introduced a flaw (see Fig 1.1(b)). Under

Table 1.1: Comparison between the experimental and theoretical strength of different materials. Of particular interest, the theoretical strength values of the cement-based materials are about 1000 times larger than the ones measured experimentally.

Material	Experimental strength	Theoretical strength	Young's modulus
Glass	0.3 GPa	14 GPa	70 GPa
Al_2O_3	0.1 GPa	80 GPa	400 GPa
Steel	0.5 GPa	40 GPa	200 GPa
PMMA	0.05 - 0.07 GPa	0.35 - 0.6 GPa	1.7 - 3.1 GPa
Concrete	0.003 - 0.005 GPa	6 GPa	30 GPa
Cement paste	0.003 - 0.005 GPa	3 GPa	15 GPa

uniform applied tension at infinity σ_∞ along the Y axis on the body boundaries, he showed that the greatest concentration of stress occurs at the extremities of the ellipse's major axis (blue dot o in Fig. 1.1(b)) where the radius of curvature $\rho_c = b^2/c$ is minimal, and it follows

$$\sigma_c = \sigma_\infty(1 + 2(c/\rho_c)^{1/2}) \tag{1.1}$$

For the interesting case where b $\ll$ c corresponding to a sharp defect, this equation reduces to

$$\frac{\sigma_c}{\sigma_\infty} \simeq 2(c/\rho_c)^{1/2} = 2c/b \tag{1.2}$$

This resulting elastic ratio of eq. 1.2 in the vicinity of the hole, the *stress-concentration factor*, may explain the disparities of table 1.1. Thus, considering a narrow flaw it is clear that σ_c/σ_∞ can take results larger than unity, and so we can conclude that is the shape of the hole rather than its size that rules the factor [9].

The energy-release-rate, G

In his paper of 1920, Grifitth faced to the failure problem with an energy method, which can be derived from the thermodynamic principles [9, 10]. One considers a linear elastic material containing a crack of length c and surface area C loaded at the outer boundaries (see Fig. 1.1(c)). Here we seek only the equilibrium position of the crack, which is defined as the position that minimize the total energy U in the system. Then, let us write U associated with individual energy terms - mechanical or surface - that depends only on the crack position.

$$U = U_M + U_S \tag{1.3}$$

where $U_M = U_E + U_A$ is the mechanical energy, U_E the strain potential energy stored, U_A the potential energy of the external applied loading system, and U_S the

potential surface energy. Lets now suppose that the crack extends itself and sweeps a surface dC, thus the total energy released during this process reads

$$dU = \left(\frac{\partial U_M}{\partial C} + \frac{\partial U_S}{\partial C} \right) dC \tag{1.4}$$

This rate of energy released, which is a finite quantity even in a slit crack geometry where the stress diverges, provides a driving force for crack advance. In qualitative terms, for crack extension to occur under the influence of an applied stress, the decrease in mechanical energy must compensate the increase in surface energy due to crack extension dc. Noting dU_M the mechanical energy of the body released during this process, the energy balance then reads as

$$dU_M = 2U_S dC \tag{1.5}$$

It describes the energy required to create two new surfaces of unit area by taking into account the atomic bond energy. Accordingly, to the applied stress level at the material boundary, the energy balance of Eq. 1.5 gives a critical condition for the crack propagation in terms of rate at which mechanical energy is flowing in the crack tip region. It is accordingly convenient to define a quantity G called the energy-release-rate

$$G = -\left(\frac{\partial U_E}{\partial C} \right)_\delta = -\left(\frac{\partial U_M}{\partial C} \right)_P = -\left(\frac{\partial U_E}{\partial C} + \frac{\partial U_A}{\partial C} \right)_P \tag{1.6}$$

where the minus sign denotes decrease in the total mechanical energy, the indexes specifies the conditions at infinity: imposed load P, or imposed displacement δ. The unit of G is J.m^{-2}, and it coincides with the units of fracture surface energy G_c defined as

$$G_c = \frac{\partial U_S}{\partial C} \tag{1.7}$$

With this, the so called Griffith's criterion for crack propagation finally follows the conditions below:

$$\begin{cases} G_I < G_{Ic} & \text{Stable crack} \\ G_I \geqslant G_{Ic} & \text{Propagating crack} \end{cases} \tag{1.8}$$

Local linear elastic field and stress intensity factor, K

From the symmetry of the elastic stress field in the vicinity of the slit crack tip, we usually distinguished three rupture modes (see e.g. Fig. 1.2): The mode I, *i.e.* opening mode, corresponds to the separation of the lips of the crack under a tensile stress action; The mode II corresponds to the shearing of the crack lips perpendicular

to the crack front; and the tearing mode III corresponds to an out of plane shearing, *i.e.* the shear of the crack lips parallel to the front. These rupture modes are defined locally at the the crack tip level, thus the stress field near the slit crack tip in an elastic media can be written as the sum of the contributions of each one, irrespective of the loading condition applied to it. As mode I *"is by far the most appropriate to crack propagation of highly brittle materials"* [9], in the following, we stick on pure mode I tensile fracture.

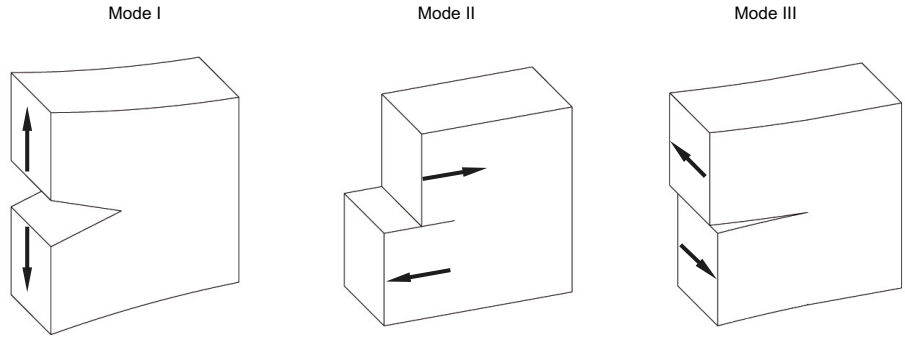

Figure 1.2: The modes of rupture: mode I, opening; mode II, shearing; and mode III, tearing.

Let us consider an infinity media presenting and straight crack. In relation to the coordinate system of Figure 1.3, the elastic stress and displacement fields' solution [11] in the vicinity of the crack tip may follow the summation of the three modes' contribution by simple forms, such as

$$\sigma_{ij} = \frac{1}{\sqrt{2\pi r}} \sum_{I}^{III} K.f_{ij}(\theta) \tag{1.9}$$

and

$$u_i = \frac{1}{2E}\sqrt{\frac{r}{2\pi}} \sum_{I}^{III} K.f_i(\theta) \tag{1.10}$$

respectively. Here, K is the so called stress intensity factor(SIF) associated to the three modes of rupture expressed in $\mathrm{Pa}\sqrt{\mathrm{m}}$. It depends both on the geometry and on external loading condition at infinity. On the other hand, the universal functions of θ, f_{ij} and f_i, and the singularity $r^{-\frac{1}{2}}$ are independent of the limiting conditions. Therefore, the three stress intensity factor determine the entire elastic filed in the vicinity of the crack tip.

For instance, the stress intensity factor in tensile mode K_I will be shown to determine the stability of a crack while the value of K_{II} will determine the path followed by the crack for two-dimensional systems. For an infinite specimen under a uniform applied tensile stress σ involving a double-ended slit straight crack (similar to the example of Fig. 1.1(b)), one follows

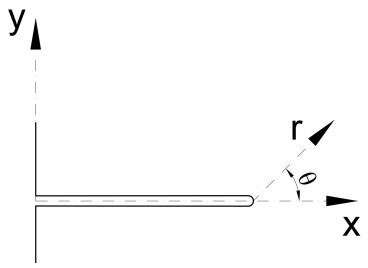

Figure 1.3: Local coordinates system in the vicinity of the crack tip.

$$K_I = \Psi\sigma\sqrt{c} \tag{1.11}$$

where c is the crack length and Ψ is a dimensionless geometry term that takes the form

$$\Psi = \sqrt{\pi} \tag{1.12}$$

For different crack systems under uniform loading conditions as well, only Ψ will differ (see examples in Ref. [9]). Nevertheless, for more complex geometries and loading conditions, K factors should be found in technical handbooks (*e.g.* Refs. [12, 13]) or fully calculated using finite element methods. The latter was chosen for this research project.

Equivalence between G and K

Let us simply describe what the Irwin's calculation in 1957 stated: the idea is to identify the amount of mechanical energy released by a solid during the crack extension on a infinitesimal length dc; for instance, we may take into account the work done by imposed surface tractions during the closure of this slit crack on dc. In other words, he concluded that the energy-release rate G is proportional to the work done by the singular terms of the elastic field - on equations 1.9 and 1.10 - during the crack closure. Then, proceeding to the limit $dc \to 0$ this relation may be written as [9]

$$G = \frac{K_I^2}{E} + \frac{K_{II}^2}{E} + K_{III}^2 \frac{1+\nu}{E} \tag{1.13}$$

Considering a solid in pure mode I tensile loading when a crack propagates, the above eq. 1.13 reduces to

$$G_I = \frac{K_I^2}{E} \tag{1.14}$$

From this, one gets another criterion of crack propagation - equivalent to the Griffith's one of (1.8). The crack will propagate only if the stress intensity factor K_I at

least balance the local toughness $K_{Ic} = \sqrt{G_{Ic}E}$

$$K_I \geqslant K_{Ic} \tag{1.15}$$

Finally, let us simply present some typical fracture toughness and fracture energy values for different brittle materials in Table 1.2.

Table 1.2: Fracture parameters for a short selection of brittle materials. Fracture energy G_{Ic} and toughness K_{Ic} (data were extracted from Ref. [9], an exception for the PMMA data [4, 14]).

Material	G_c (J.m^{-2})	K_{Ic} (MPa.m$^{1/2}$)
Silica - Sio_2(glass)	8	0.75
Sapphire - Al_2O_3(1010)	25	3
Steel - Fe + additives	50 - 50000	20 - 100
PMMA		0.7 - 1.6
Concrete	30 - 80	1 - 1.5
Cement paste	10	0.5

Limitations on the slit crack concept: The existence of a process zone

The general concepts of the LEFM discussed so far provided a powerful method to predict when a crack will extend in a perfectly brittle medium. Briefly, based on an energy balance concept, the mechanical energy, in which the material is submitted when loaded, must balance with the surface energy required to create two new surfaces. Nevertheless, this approach has not to tell about how the crack may advance. The divergence of the elastic stress field at the crack tip location is physically unrealistic. Thus, we deal here with the lack of some vital elements against the description of the crack propagation in real solids.

Real materials develop plastic deformation or damage when its intrinsic strength σ_c is exceeded in the vicinity of the crack tip. First, this explain why mechanisms relaxing this stress are expected in a sort of extended process zone near the tip location. Let us note that the size of this process zone depends on the material. Then, it yet explains the existence of highly dissipative process highlighted by the large values of experimental fracture energy G_c, *i.e* fracture energy is always greater than the energy needed to create new surfaces. Therefore, we must take into account for nonlinear and irreversible elements in the basis of LEFM to better understand the behavior of structural brittle materials.

With this in mind, let us tell about the *small scale zone* concept However. Its assumption incorporate these dissipative processes in a zone of finite extent in the

vicinity of the crack tip [1]. This process zone size l_{pz} involves the maximum distance from the tip where the stress imposed by the presence of the crack is sufficient to induce irreversible deformations. A rough approximation may follow the relation

$$\sigma_c \sim \frac{K_c}{\sqrt{l_{pz}}} \tag{1.16}$$

We should also highlight an approach derived from this concept: called cohesive-zone model [15]; with constant cohesive strength σ_c, it predicts

$$l_{pz} = \frac{\pi}{8}\left(\frac{K_{Ic}}{\sigma_c}\right)^2 \tag{1.17}$$

Let us rapidly introduce the powerful mathematical work of Rice [16] that associate fracture description at macroscopic and microscopic levels: defined as the Rice line integral J, or J-integral. For instance, if l_{pz} is smaller than any structural length, *e.g.* the crack length, G now interprets the energy flow going to the crack tip region that yet is defined from local stress field in the vicinity of the crack tip, but using the concept of J-integral. The path-independent characteristic of the J-integral can be used to determine G as the crack driving force, from the presence of some localized process zone at the tip under small scale zone conditions.

When considering real material applications, any heterogeneity into the microscale may affect its structure in a catastrophic manner. This is, therefore, a crucial issue for the next section since we have considered ideal homogeneous brittle solids. The following section is devoted to present some attempts of using the LEFM framework to understand the fracture mechanisms of cement based materials.

1.2 The experience of fracture mechanics approach to cement based materials

The study of fracture in cement based materials was primarily centered on the interface aggregate-cement paste or aggregate-mortar, *i.e.* their bond behavior, since it should be considered as the weakest link or the major source of Griffith's flaws, which allow cracks to propagate. Nevertheless, during the 1970s, the earlier literature in this filed primarily reviewed by Radjy *et al.* and a few relevant studies [17–21] showed why the influence of the complex cementitious microstructure should not be neglected since crack propagation could take place through the hardened cement paste.

Since the pioneering work of Kaplan [22], a great effort of the scientific community has been carried out in this area. Tough they have been extensively reviewed

[1] In other words, it incorporates dissipative work terms into a composite surface energy [9]

back in the 1980s by Mindess [23], and more recently in 2002 by Bazant [24] focusing on testing and modeling of concrete materials. Despite these great number of models and experiments that have been reviewed, we restrict here to summarize a few relevant matters. Although we might rapidly present some reports about the macroscopic behavior of concretes, the main goal of this investigation that is centered on the microstructural features of hydrated cement pastes as considered in last paragraph. This will reflect on the discussion of this section emphasizing the fracture studies on cement pastes.

Fracture mechanics in concrete materials was first applied in 1961 by M. F. Kaplan . Since then, many authors have been discussing the concepts usually applied to fracture of brittle solids in order to understand fracture mechanisms in cement paste, mortar and concretes. Radjy *et al.* [25] summarize the aims of fracture tests relating them to evaluate the following parameters: the elastic energy release rate G, the stress intensity factor K and the fracture surface energy Gc. Theoretical and experimental works on cement pastes were individually confronted and some remarkably concluding were described: fracture occurs by a single straight crack (tests with 3 point loading in single edge notched beam), K decreases with increasing water/cement ratio and air content, the fracture parameters are insensitive to curing time, but an exception to very early ages were highlighted. A word may be added here, it is well known that the strength of Portland cement materials increases with time due to the early hydration reactions that takes place after mixed with water; this rate growth is even more pronounced during the first weeks up to the material maturity. Thus, the insensitivity of fracture phenomena to curing time regards to pastes already considered as mature (after 28 days old). Let us take Figure 1.4[2] [23] as example, it displays that up to 2 weeks the cracks propagate preferentially through the high porosity zone of calcium silicate hydrate (C-S-H)[3] [18, 27], since at early stages of hydration both the unhydrated cement particle and the calcium hydroxide ($Ca(OH)_2$ or CH)[4] - the other early reaction product - correspond to zones of low porosity at that scale, *i.e.* phases acting as rigid inclusions.

In 1972, the remarkably study of R. L. Berger stated that the role of calcium hydroxide and clinker grains should be considered when analyzing experimental data, and assume cement paste as homogeneous material was not reasonable. In 1973,

[2]Image is courtesy of personal archive of R.L Berger to the Ref. [23].

[3]The C-S-H is one of the two main hydration products formed when Portland cement reacts with water. It is a nearly amorphous calcium silicate hydrate with properties of a rigid gel. The dashes on its nomenclature represent no particular composition implied, and are necessary because in cement chemistry notation it denotes material specifically of composition $CaO \cdot SiO_2 \cdot H_2O$. It is usually adopted a "C-S-H gel" term to distinguish the compound formed in cement [26].

[4]A word should be added here about the common cement chemistry notation, though the one that we adopted for the reminder of this manuscript: C = CaO; S = SiO_2; A = Al_2O_3; F = Fe_2O_3; H = H_2O; $\check{S}$ = SO_3

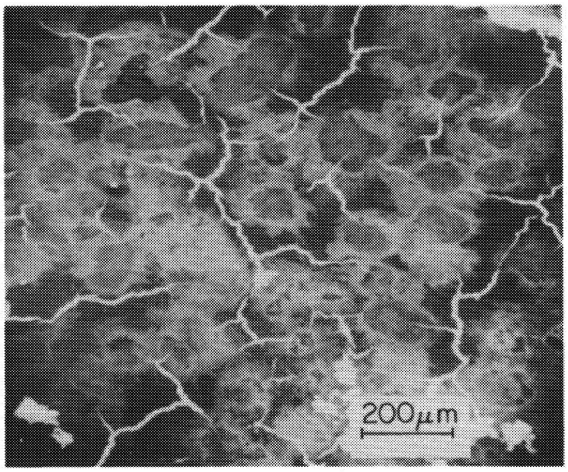

Figure 1.4: Optical micrographs of C_3S paste hydrated for 14 days. The bright areas are the crack that appears to be largely in the C-S-H region [23].

Berger *et al.* presented optical micrographs of thin slabs of tricalcium silicate (C_3S) pastes[5], after failure under bending (see Fig. 1.5). They showed that the fracture path after 1 day passed around CH crystal areas, and through the matrix - the outer-product calcium silicate hydrate that bonds C_3S particles together. At 28 days, CH crystals cover the majority of the paste area, and the fracture pattern smoothly occurred through the CH rich areas and C-S-H phase, since it was impracticable to determine a non CH area.

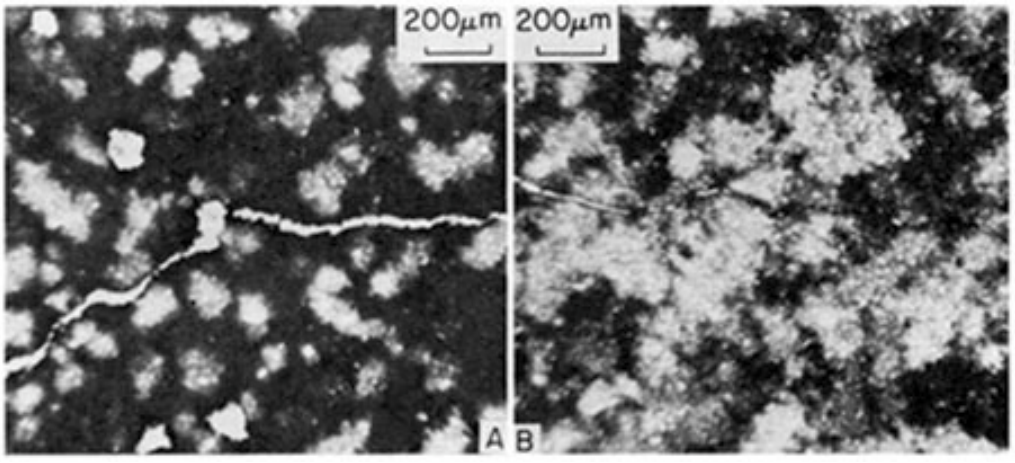

Figure 1.5: Optical micrographs of C_3S paste thin slabs after fracture. Examples after 1 and 28 days hydration (left and right, respectively). The bright areas are CH-rich regions (Courtesy of Berger *et al.* [18]).

[5]Regarding the strength development, the most important of the four major constituents that make up Portland cement is by far tricalcium silicate such as of original chemical formula of Ca_3SiO_5 [26]. It was often used as a simplified model system to enable one to interpret the mechanisms controlling the hydration and engineering properties when investigating the microstructure of Portland cement [18, 27].

1.3 Cement-based materials: Environmental concerns

Actually, concrete - classically the material composed by Portland cement, aggregates, and water - is the most used material in the world. It plays a fundamental role on the basis of civil and structural engineering of modern times. Its consumption is increasing so fast that in 2050 it is predicted to reach about four times the level of 1990; we already produce it in such a large scale of over 2 billion tonne quantities per year [28].

The annual production of cement was about 4 million tons in 2013 [28], and estimations about the CO_2 emission from the cement industry accounts globally for 5-8% of total emissions worldwide [29]. Therefore, it seems natural to associate cement and concrete industry to high environmental impacts, and it has been indeed. These context definitely lead us to ask some questions: why do we keep using cement and concrete materials? Don't we have any other material option? Nevertheless, we shall look for answers when comparing it with the other material options that we may have. Let us here present a few considerations of Prof. K. Scrivener [29]: (i) For instance, by measures of carbon dioxide emissions per ton, concrete is considered as more environmentally friendly than wood; (ii) *"Looking forward, especially to the developing regions of the world, it is the only material that can satisfy the demand for decent low-cost housing and infrastructure"*;

Working on a greener development of cement based materials is therefore the way the cement and concrete community shall face the issue. Considering this, we have addressed this work to one specific matter: the recycling of construction and demolition waste as alternative to produce cement compositions, though it is the main subject discussed in this section.

Construction and demolition waste (CDW): An historical background and its present situation

Wastes provided by the demolition of building and civil infrastructures have been seen as an alternative for the production of aggregates for new cement based materials since the World War II period. The first technical reports about reuse of construction and demolition waste in concretes are dating back to the middle 1940s when the rubble of demolished buildings were piling up in cities after bombardments [30]. In fact, the construction of the English St. Albans Cathedral[6], which the date of execution is an unknown matter (suggested dates from the mid-300s or

[6]Formally the Cathedral and Abbey Church of Saint Alban, and referred to locally as "the Abbey". It is a Church of England cathedral in St. Albans, England (definition from Wikipedia).

earlier), was realized with building material from the ruins of the Roman city of Verulamium [31].

Germany and Great Britain were the first countries to present well-documented works on the reuse of demolition materials during and just after the World War II. In 1976, Nixon [31] reviewed the most relevant information concluding that in German the debris used to manufacture aggregates for general concrete (discarding high strength concrete) mostly contain brick work (predominant building material at this time), building blocks, pieces of concrete and adherent lime and cement mortar. This reviewed works[7],[8],[9] provided applicable information for usage of recycle aggregate concrete (RCA) in roof and floor slabs, concrete walls and hollow blocks manufacturing. Concluding the German experience, Nixon attempts to a warning described in one of those publications[10]: the fact that where gypsum mortar or plasterboard were present in debris, special attention should be taken to guarantee the sulfate content under 1% and to obtain "better class concrete" wood and organic matter should be excluded. From British documents[11],[12], Nixon extracted information about properties of the most promising materials such as that from the demolitions of shelters, blast walls and defence posts as those were not plastered. After this period, demolition wastes have been rather reused or recycled in real applications. Indeed, the small quantity reused represents base or sub-base in road constructions, while, the remaining constituents are still eliminated in landfills [32].

Inadequate solid wastes disposal is an actual world concern. In United States the Solid Waste Disposal Act of 1965 was the first federal effort in developing waste management safely. Since then, standards and laws related to management of waste and chemical substances from debris have been developed [33]. The solid wastes are classified as hazardous and industrial. Fuels, corrosive, reactive and toxic are some definitions for the hazardous materials ruled in USA by the Environmental Protection Agency (EPA). These materials are unrecovered and non-recycled, needing special and controlled treatments to disposal. On the other hand, industrial waste is defined as non-hazardous trash generated by the goods production, e.g. the construction and demolition waste (CDW).

Regarding the CDW management, which is the main solid waste matter of this

[7]Collection of translations from the German on the utilization of brick rubble, 194415. Ministry of works. London, 1946.

[8]The German Building Industry. British Intelligence Objectives Sub-Committee BIOS Final Report No 575, Item 22, London 1946 (HMSO).

[9]'Building debris in structures', German Building Authorities of Hamburg, *The Builder*, 1946, Vol 104. No 5410, pp 383-384.

[10]Manufacture of broken brick concrete, Board for the economic use of rubble, Berlin-Dahlem 1944.

[11]Reuse of brick rubble from shelters, blast walls, defence posts etc. BRS TC 1413.1945.

[12]A.J. Newman, 'The utilization of brick rubble from demolished shelters as aggregate for concrete', Inst Mun Co Eng J. 1.946, Vol 73 No 2, pp 113-121.

work, some international standards and technical reports already exists to rule its application in structural concretes. In United States, the ASTM C33 [34] considers material from crushing of hydraulic cement concretes in its coarse aggregate definitions for concrete structures since 1982. In the same way, the standard procedure determines fine aggregate as natural sand, manufactured sand or a combination of both. According to ASTM C125 [35], the definition of manufactured sand includes materials from concrete crushing. Moreover, the American Concrete Institute (ACI) Committee 555 [36] reported technical and practical information to produce concretes with recycled aggregate concretes.

In general, European procedures proposing the recycled aggregates (RA) as a concrete constituent were still technical reports or practical recommendations. Hansen [37] marked procedures prescribed in Netherland, United Kingdom, Germany, Russia and Denmark. For example, more than 80% of demolition wastes are recycled in Netherland and, their recommendations of usage are clear which definitely allow to decide if it is valuable adopt recycled material to manufacture concrete from the standard (EN 5905) for natural aggregates [38].

The Building Contractors Society of Japan defined a standard procedure [39] to use recycled aggregates and recycled concrete aggregates. Physical properties (density and water absorption ratio) defined in the standard document are marked in Table 1.3.

Table 1.3: Quality requirements according Japanese standard for the use of recycled aggregate and recycled concrete aggregate. (Extracted from B.C.S.J [39]).

Test method	Recycled coarse aggregate	Recycled fine aggregate
Density (kg/m^3)	≥ 2200	≥ 2000
Water absorption (%)	≤ 7	≤ 13
Solid content (%)	≥ 53	–

Generalizing the Brazilian context, a federal law (n^o 12305) establishes the national policy of solid wastes since 2010 and the first national report that attends to the construction and demolition solid waste question was the *Resolução n^o 307* of CONAMA[13] in 2002 [40]. A few ABNT[14] standards [41–45] rule the construction and demolition solid waste management. Nevertheless, the only one that brings up the recycling of CDW as option for concrete materials [45] limits the topic to the construction of road base or sub-base and non-structural concrete.

The International Solid Waste Association (ISWA) in Brazil[15] provides an annual report summarizing information of solid waste in the country. According to data presented in Panorama 2013 [46], the Brazilian counties collected more than 117

[13] *Conselho Nacional do Meio Ambiente* (National Environment Council of Brazil).

[14] *Associação Brasileira de Normas Técnicas* (Technical Standards Brazilian Association).

[15] The *Associação Brasileira de Empresas de Limpeza Pública e Resíduos Especiais* (ABRELPE) is the representative institution of ISWA in Brazil

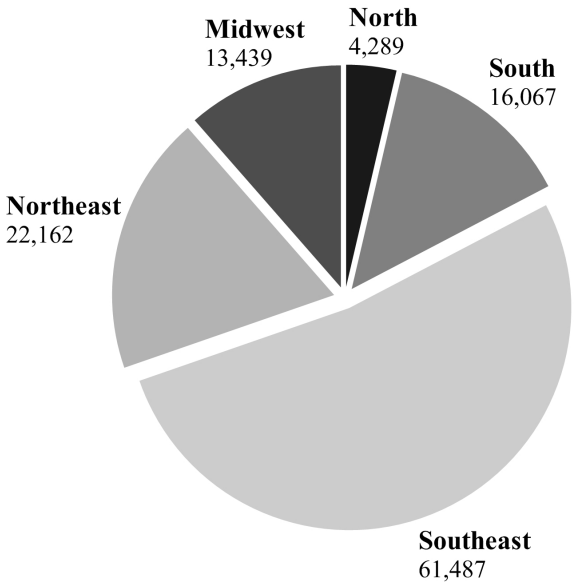

Figure 1.6: Construction and demolition waste collected by regions in tons/day (figure adapted from Panorama 2013 [46]).

thousand tons/day of CDW in 2013, increasing in 4.6% the amount registered in the previous year. Figure 1.6 shows the amount of CDW collected in different Brazilian regions. It is remarkable the high content presented by the south region, where two global metropolis, *São Paulo* and *Rio de Janeiro*, are located. All this stated still need attention relating to the fact that counties just collect wastes in public grounds, since the management of particular waste generated by private corporations is their own responsibility [46].

Researchers from the post war period that relates the reuse of demolition wastes as aggregates for concretes (recycling demolished concrete and masonry) were summarized in technical state-of-the-art reports until 1978 by Nixo [30] and up to 1990 by Hansen [32, 37]. Furthermore, contemporary studies reviewed by Brito *et al.* [47], Xiao *et al.* [48] from 1985 to 2004 and Xiao *et al.* [49] from 1996 to 2011 exclusively in China also support the use of recycled aggregate as a constituent of concrete components for constructions in recent times.

Recycling masonry and concrete: Some practical applications and material properties

In 1978, Nixon [30] stated that most of researches at that moment were focusing on materials classified by uncontaminated, *e.g.* old laboratory samples. However, these studies already revealed high water absorption by the recycled concrete aggregates due to the adherent cement paste in aggregate particle. Regarding the compressive strength, the researchers agreed that the results were around 20% lower to recycled mixtures with coarse aggregates in comparison to control mixtures with no recycled

constituents. The recycled coarse aggregate did affect the new material Young's modulus and, in fresh state, only the recycled fine aggregates significantly modify the material properties, decreasing its workability. The real influence of the original concrete strength in the new one was an unknown matter, however, when the failure of new recycled concrete occurred it seemed that the old adherent cement paste in the aggregate was the weakest zone in the system. From Nixon's concluding remarks, the recycled concrete aggregates compressive strength decreasing suggested to deeply investigate the properties of original concrete and the fracture mode of the new recycled ones in order to better understand and clarify the inferior results presented.

Completing the prior discussion, Hansen [32, 37] published updated knowledge at that time also including applications with recycled masonry. Compressive, tensile and flexural strength results were still quite lower than control mixtures with natural constituents, nevertheless, some situations at laboratory scale enable to produce recycled concretes in the same strength class or even higher than reference concretes. The author identified that the homogenized constituents provided mixtures with coefficient of variation for strength results equivalent to regular concrete mixtures. Despite some higher Young's modulus results found to mixtures with coarse aggregates, the majority of studies presented lower values due to the rough and porous surface provided by the adherent paste over the crushed aggregate. In general, when the concrete mix-designing used only natural sand it was possible to substitute up to 30% of natural coarse aggregate by recycled ones without significantly affect its mechanical properties.

Recent developments in recycling CDW for use in concrete materials has been reaching important characterization results that encourage its application. Experimental analysis of the mechanical behavior of recycled aggregate concretes (RAC) has been extensively discussed by many authors [47, 50–62].

In general, for both concrete and masonry (ceramic/clay) waste, the results indicate that the material strength decreases when the substitution rate of natural by recycled aggregates increases. The recycled concrete needs more water in order to achieve the desired workability for a designed strength class due to the high water absorption ratio of the recycled aggregates [53, 62]. Moreover, for high substitution rates, e.g. over 50%, the material demands high amount of cement and water content to reach the designed compressive strength which, consequently, makes it more expensive [53]. Etxeberria *et al.* also suggests to not design mixtures above 45 MPa. Cleaning solutions [62] to reduce the amount of adherent paste/mortar from the crushed aggregate have been studied in order to control its porosity and absorption rate.

Nevertheless, none of this studies discard the possibility to produce recycled

mixtures with increased strength. Leite [50] evaluate the substitution rate the effect of coarse and fine recycled aggregate originated from a highly heterogeneous source. The main conclusion was that while coarse inclusion amount reduce the strength, the fine particles could provide strength gains with high substitution ratios. Indeed, it could be explained by the higher amount of fine particles by the recycled fine aggregates which prevent segregation, improves packing density and reduce void content.

Let us insist here that CDW from ceramic and concrete source could be potentially used to produce concrete and mortar as fine and coarse aggregates, and that its production such as its acceptance have been increasing as demonstrated by the extensive literature reviewed till now. Therefore, give alternatives for the remaining dust, *i.e.* the fine powder, generated during the crushing procedure of the debris to produce recycled aggregates is also an environmental issue. A word may be added about recycling CDW with only one crushing action - by a jaw or impact crusher. It is a procedure that produces coarse and fine aggregates in similar proportions of approximately 50 wt% exhibiting high levels of these remaining dust powders (particles < 75 μm) [63].

Relevant, but yet just a few, studies have been carried out to characterize [64, 65] fine ground particles of the recycling of ceramic waste[16] and also their effects [66–71] in cement based materials. Of particular interest, some of them reported about the pozzolanic activity of these particles when introduced in Portland cement mixture compositions [68, 70, 72].

On the other hand, if we consider the context of a more heterogeneous construction and demolition waste, *e.g.* debris from a building demolition, or even from a singular concrete structure, not but a few researches have addressed to the re-use of fine particles as a valuable alternative.

Amorim *et al.* [67] addressed their study to analyze the effects of the specific surface area of fine residues on the mechanical behavior of lime mortars. The recycled material - originated from two different construction sites and form red ceramic industry - was ground for different time interval up to 90 minutes before include them in mortar mixtures. Their findings revealed pozzolanic activity for the various recycled powders; more pronouced for the red ceramic wastes. Then, as expected, it also confirmed that surface area is one of the parameters that govern the effects of pozzolans.

Recent attempts have been made to fully recycle this waste type: In 2012, although the field of application was a geopolymeric binder with fly ashes, Ahmari *et al.* [73] proposed to recycle concrete waste without separating coarse and fine frac-

[16]Not necessarily coming from the recycling aggregate crushing procedure but, however, they definitely correspond to the CDW category.

tion aggregate fraction. Koshiro *et al.* [61] have proposed a fully recycling model for the CDW generated from a building demolition. The coarse and fine particles was used as high quality concrete aggregates while the remaining powder - named by the author as a by-product in the recycling process - as component to produce tiles for a new building. Chen *et al.* [74] also employed the powder from the CDW aggregate crushing process but, however, as filler in asphalt mixtures.

In very recent researches, the recycling of the fine powder from concrete was evaluated to as possible raw material for the Portland cement clinker's production. Schoon *et at.* highlight that the recycled material they obtained would be used as a replacement option, however, considering only amounts lower than 15%. Gastaldi *et at.* achieved promising results; a clinker very similar[17] to the regular clinker could be produced with 30% replacement of regular raw material by recycled one.

To summarize, despite the great interesting in recycling CDW, and more specifically to the fine portion generated during the recycled aggregate production, it is clear that a lack in the scientific knowledge still remains about the properties of cement based materials containing this type of waste. In particular, which concern to its microstructural features and even more specifically to its fracture properties. This study will provide new insight towards this promising category of cement based materials.

[17]Mineralogical composition very close to that of the reference clinker.

Chapter 2

A new methodology for the characterization of tensile fracture properties

Measuring accurately the toughness of of material is a difficult task for several reasons. First, toughness is defined as the critical driving force (or critical elastic energy release rate) at which a crack can propagate. In principle, this means that both the crack position and the total energy released during crack advance must be tracked during the test, rendering the measurement very indirect and prone to multiple causes of experimental errors. A way to circumvent this difficulty is to measure directly the toughness from the displacement field, but this also poses other challenges as discussed in the following. Second, the toughness value G_c may depend crucially on the crack growth velocity v. As a result, an accurate and complete characterization of the failure properties of a solid requires the determination of the so called crack growth law $G_c(v)$. This requires the development of fracture tests where the crack speed can be controlled and tuned over a broad range. Lastly, measuring toughness requires stable fracture, both from the point of view of crack propagation (*i.e.* crack must stop when the external driving is stopped) and trajectory that must be rather straight. This can be particularly challenging in brittle solids like *e.g.* cement paste. The choice of the *geometry* of the fracture test that controls the crack stability then becomes essential.

For these reasons, various fracture test geometries have been proposed that handle these various challenges in different ways. Among the most classical geometries, three or four point bending, double cantilever beam (DCB), double torsion (DT), and compact tension (CT) have been extensively used for fracture toughness characterization. Nevertheless, they present a rather poor stability of the fracture process, as we will see in the following. The Tapered Double Cantilever Beam (TDCB) speci-

men has been used to perform fracture tests in pure mode I loading of adhesive bond joints [75–77] and to study R-curve behavior in quasi-brittle materials like wood [78] due to its stable crack growth ability. In many experiments it has been observed that for this geometry - loaded under displacement control - the compliance increases linearly with crack length, which has been supported by analytic calculations using beam theory [77, 79, 80]. As the energy release rate (G) depends on the derivative of the compliance (see eq. 2.3), when crack propagates, the value of G is constant. The classical test geometry has a straight portion in front of the taper to facilitate the load application and the width-length ratio of the specimen is usually less than 0.4. Furthermore, this is not adapted for brittle isotropic failure like, though we propose here a new geometry inspired from TDCB that is very stable. In our specimen, we first remove the straight portion, as having narrow sections is difficult to machine, and design larger arms because - in the case of cement pastes - the specimen is likely to break in the arms itself.

In addition, we will see that this new geometry allows for a great stability of the fracture process that is well suitable for highly brittle materials like cement paste. Also, it allows for the exploration of a large range of crack growth velocities. Our experimental procedure is dedicated to mode I tensile fracture. This choice has been motivated because in isotropic solids cracks usually seek an orientation that minimizes the mode II loading, leading to a dominant tensile mode. In section 2.1, we first review some classic test methods for fracture toughness characterization. We then detail the proposed methods starting in section 2.2, by a finite element study of the stability of the fracture process in our modified TDCB geometry followed by its practical implementation to a model material - the PMMA - in section 2.3. In particular, we show how several fracture tests performed at different loading rates can be used conjointly during post-treatment to achieve very accurate crack growth law $G_c(v)$ over a wide range of crack speeds. In section 2.4 we show that our fracture test geometry is amenable for a direct determination of the toughness through digital image correlation (DIC). This is an interesting alternative to the prior implementation of our test as it can also measure the local stress intensity factors K_I and K_{II} relevant for anisotropic solids and the amplitude of the non-singular terms like the T-stress.

2.1 A review on mode I fracture test geometries

Since the the theoretical framework proposed by Griffith [5] many experimental procedures have been explored to comprehend the fracture mechanism of a broad range of materials. Some standardized tests such as single edge notch beam (SENB) in three or four point bending load, compact tension (CT) and double cantilever

beam (DCB) have been extensively used to characterize the fracture behavior of solids as well as other classic yet not standard geometries like the double torsion (DT) and tapered double cantilever beam (TDCB). Although, a recommendation of the technical committee RILEM[1] [81] for the determination of fracture energy of concrete by three point bending test, it is worth mentioning that none of these tests are standardized for toughness measurement in cement pastes, mortar, and concrete. This section briefly reviews some relevant test geometries for mode I tensile fracture and presents their strength and limitations.

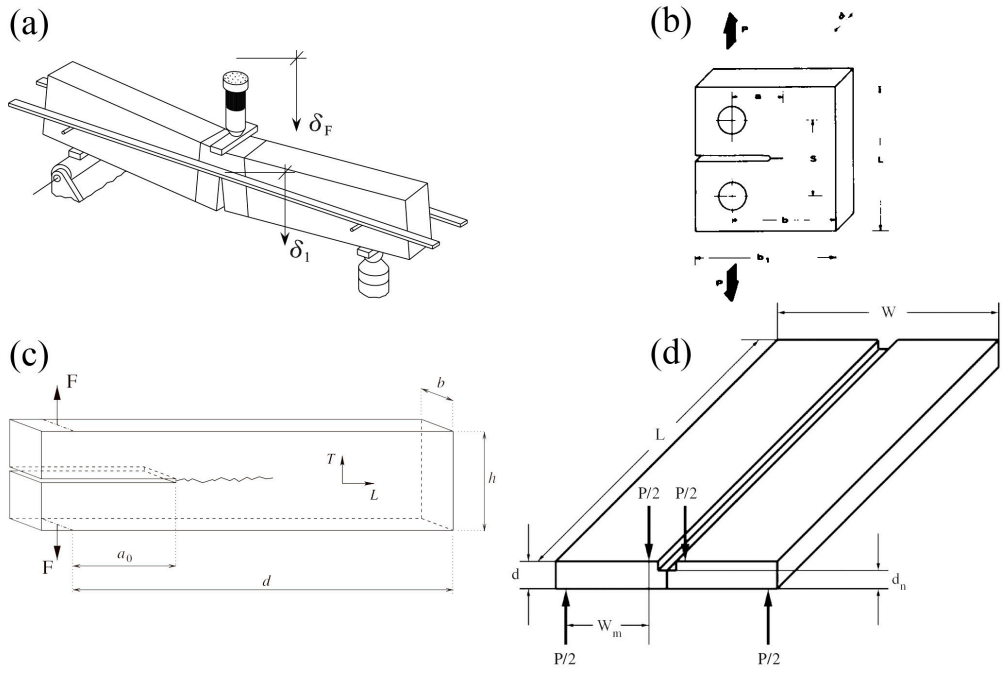

Figure 2.1: Literature review of different geometries for mode I fracture. (a) Single Edge Notched Beam (SENB) in 3 point loading [82]; (b) Compact Tension (CT) [83]; (c) Double Cantilever Beam (DCB) [78]; and (d) Double Torsion (DT) [84].

Flexure specimens like a single edge notched beam in three or four point bending, or tensile ones such as compact tension have been well recommended as standard geometries to determine fracture toughness of metallic materials [85, 86], study stress corrosion in metals and alloys [87], and also measure the fatigue crack growth [88]. The main advantage of SENB, *e.g.* in three point bending test is the rather simple specimen preparation and testing. On the other hand, SENB specimens has a short propagation length and requires a lot of material. It is worth noting that the results obtained with this testing method are sensitive to specimen and loading geometries as well as to the strain rate.

In CT specimen geometry the constraining dimension is the thickness of the material. It is often chosen when the scenario is of shortage availability of material due

[1]International union of laboratories and experts in construction materials, systems and structures

to its compact design. For instance, when testing rolled materials,*i.e.* anisotropic solids, the notch configuration should be aligned in the same direction of the roll. Let us highlight that in brittle and quasi-brittle solids the stress intensity variation at the tip of a growing crack is nearly dramatic in both, SENB and CT, test configurations [89], imposing to an unstable crack growth.

In rock mechanics, for instance, the double torsion (DT) test [90, 91] has been used to measure the relationship between the crack velocity and the energy release rate - $v(G)$ curves. The test configuration consists of symmetric four-point loading around a crack, or a notch on one end of a rectangular plate; this produces torsional deformation in the two plate halves. If this fracture test is relatively practical to implement [89] thanks to its rather simple geometry as well as the presence of lateral grooves that favor a straight crack propagation, this experimental procedure has many drawbacks (see *e.g.* Refs. [89, 92]). At first, crack velocity as well as stress intensity factor are not constant along the crack front, making the interpretation of the results more difficult than for a rock failure by propagation of a straight crack front. In other words, it provides a complex crack front geometry resulting in inhomogeneous crack growth velocity along the front. Then, the load relaxation method [93] used generally for the DT test leads to a deceleration of the crack, limiting the available range of velocity up to the initial imposed velocity, usually of the order of $v \simeq 1$ mm.s^{-1}. Finally, the presence of grooves on one side of the specimen results in systematic errors by imposing a complex and uncontrolled additional loading to the specimens [91].

The double cantilever beam test specimen is described in international test standards (see *e.g.* Ref. [94]) and typically used for the study of the delamination of long fiber reinforced composites [95–97] and adhesive bond joints [98] under dominant Mode I loading. A few attempts have been done with this geometry to study the fracture properties of cement pastes and mortars [20, 99]. The main advantage of using this specimen is that the strain energy release rate decreases with increasing crack length[2] and thus, the crack may be arrested without the specimen break completely providing therefore a range of fracture toughness measures among a single test specimen. Furthermore, it allows to determine the Mode I fracture toughness K_c (or fracture energy G_c) of the material at initiation and crack arrest. Nevertheless, this geometry has small arms that can result in failure near the point of application of the forces. That's why it is mainly limited to anisotropic materials where fracture will preferentially take place along the mid-plane of the specimen.

In this study, we take inspiration from DCB specimens and modify the tapered double cantilever beam geometry. In general, our geometry takes into account for

[2]Under displacement control in fracture experiments. On the other hand, G will increase with crack length under fixed loading conditions [100]

larger arms that will prevent failure of occurring around the loading point and, as previously mentioned, for tapered lateral sides that relies on the fact that they provides more stability during crack propagation (see for example Ref. [101]).

2.2 Numerical study of the modified tapered double cantilever beam

During crack propagation, we measure force and crack opening displacement, however, as the purpose here is to determine the material fracture properties G and v a question may arise: How do we go from the experimentally measured quantities to the material fracture properties? The flowchart of Fig. 2.2 presents the idea behind linking the experiment and finite element method for toughness measurement. Starting with the measure of the experimental compliance and comparing it to the theoretical one $\lambda(c)$ to obtain the crack length. Then, from the force measurement and the crack length, we determine the elastic energy release rate $G = F^2 g(c)$. The crack speed follows from the derivation of the variations of crack length with time. So the objective with the finite element simulation is to extract $\lambda(c)$ and the $g(c)$. In the following paragraphs, the simulation procedure is described as well as its solutions.

This procedure takes inspiration from the compliance method used for example in classic TDCB tests [82, 101]. The method builds on the following assumptions: (i) brittle fracture behavior, *i.e.* the material behaves elastically, except in a zone localized at the crack tip vicinity and small with respect to the sample size; (ii) no time dependent behavior, *i.e.* visco-elastic response of the material is negligible.

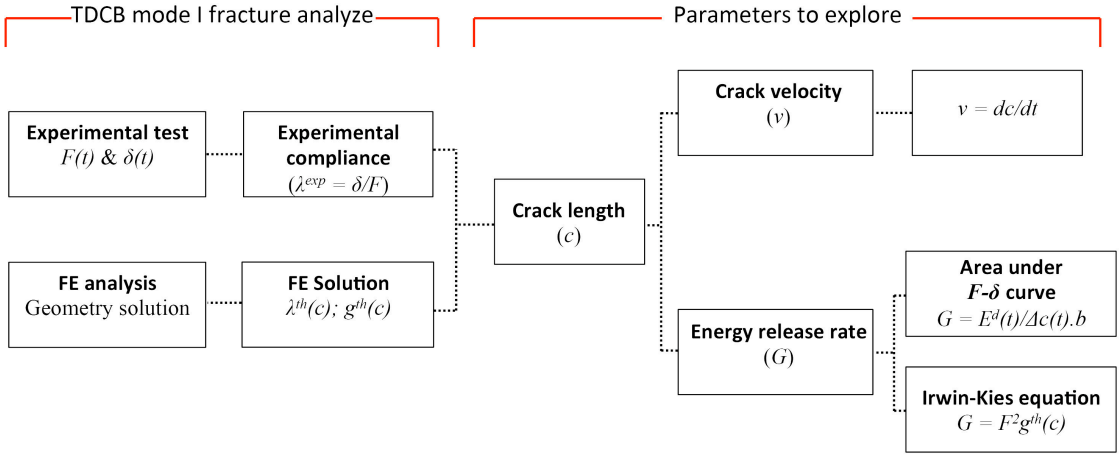

Figure 2.2: The procedure for toughness measurement.

As the specimen's width is relatively wide and then the width/length ratio of 0.45 prevents beam theory to be effectively applied, 2D finite elements calculations

were performed to determine the stress intensity factor (K_I), the compliance λ_F at the point of application of the force as function of the crack length c for the new TDCB geometry. Its dimensions were written as a multiple of the mesh size using quadrilateral square elements of size - in both X and Y directions - denoted as $e_x = e_y$. Geometry is given in Figure 2.3 and Table 2.1 displays the dimensions of the geometrical parameters in e_x units and their corresponding values in millimeter. The tapered shape of this specimen provides a stable crack growth in mode I fracture (see Ref. [102]).

Table 2.1: Dimensions of the TDCB geometry used for the finite element simulation (in e_x) and their respective values (in mm) for the specimen adopted in the experimental analysis.

Units	Geometrical parameters									
	L	c_{ini}	b	R	l_x	l_y	Δ	Δ_F	h_1	h_2
(e_x)	400	148	32	10	51.2	56	30	112	120	180
(mm)	100	37	8	2.5	12.8	14	7.5	28	30	45

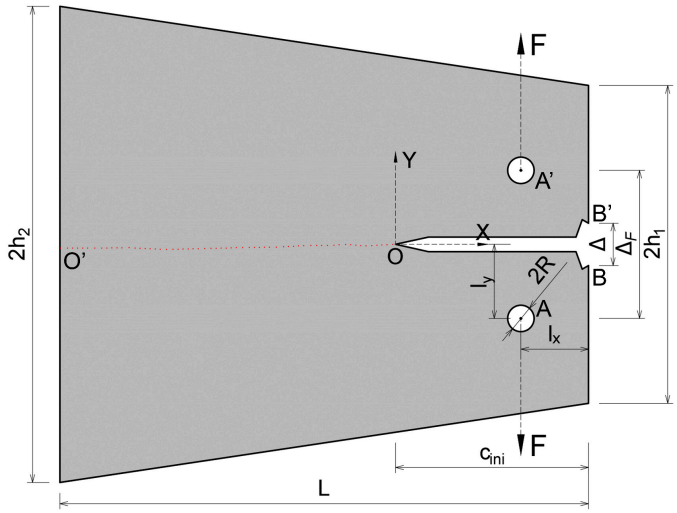

Figure 2.3: Tapered double cantilever beam specimen geometry and its dimensions.

The simulations were carried out in Cast3M®, an open-source finite element package developed by CEA in France. Exploiting the symmetry in the system, the simulations were realized on the upper half of the sample only. A typical mesh configuration used in the analysis is presented in Figure 2.4(a). Unit force along Y-axis is applied in the center of the hole (A') for the pins. This ensures mode I loading of the specimen. Displacements of the ligament OO' (see Fig. 2.4(b)) along the Y-direction are prevented to take into account the sample symmetry. Crack length is increased incrementally and the system is solved for displacements under plane stress and linear elastic conditions. The displacements are extracted at the point

of application of the force A', and at the location of the clip gauge[3] B' (δ_F and δ, respectively). Then, we define a ratio $r = \delta_F/\delta$ and calculate the compliance at these locations (λ_F and λ) relating them by r as well. We perform all our calculations - in the numerical model - using the compliance at the loading point but in the experiments, the displacements are measured at the ligament BB' and, therefore, we use r to calculate the corresponding displacements at the point of application of the force. The relative displacements are denoted as Δ_F and Δ (ligaments AA' and BB', respectively, in Fig. 2.3(a)). The Poisson's ratio ν was set to 0.3, however, as we have plane stress conditions, the compliance and mode I stress intensity factor results are independent of the Poisson's ratio.

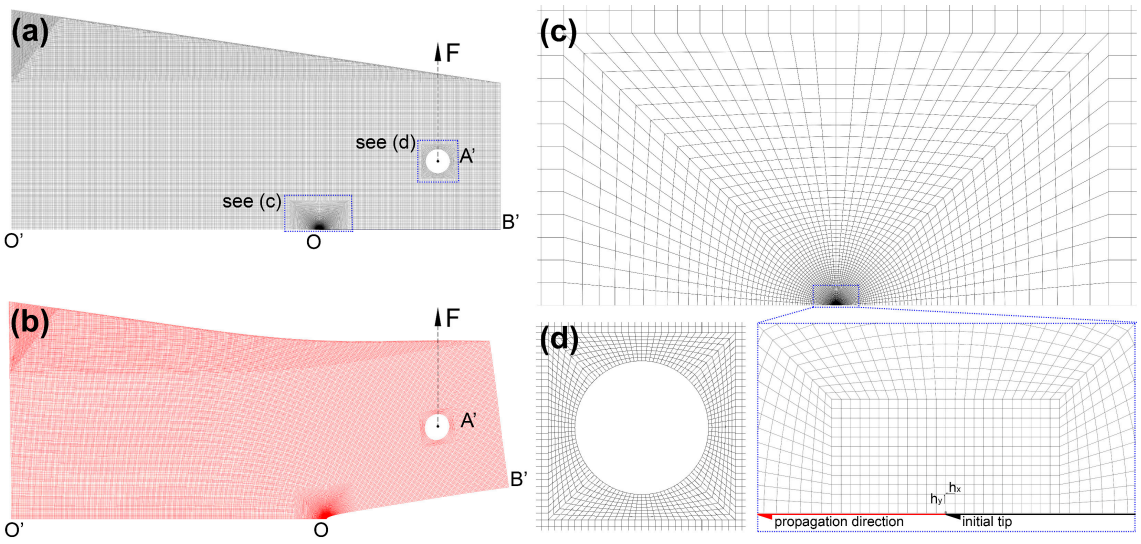

Figure 2.4: Finite element mesh for the TDCB specimen. The upper half coarse mesh used for the analyses has $\sim$ 9x10^3 nodes and $\sim$ 1.8x10^4 dof (a). The fine mesh has $\sim$ 1.4x10^5 nodes and $\sim$ 2.5x10^5 dof; in (b) the deformed configuration after unit force applied in y direction; in (c) the refinement strategy closer to the initial crack tip position of the order of $1e^{-11}$mm and; (d) represents the mesh refinement surrounding the hole where the force is applied.

A semi-log plot of the non-dimensional compliance and crack length obtained from the finite element solution is shown in Figure 2.5. We observe that for a certain range of crack lengths, the dependence of the compliance on the crack length can be fit using an exponential function (solid line in Fig. 2.5) such as

$$\lambda_F = \frac{\lambda_0}{Eb} e^{c/c_0} \tag{2.1}$$

where E is the Young's modulus, b the specimen thickness, λ_0 and c_0 the parameters of the fit. However, the compliance values follow the exponential fit approximately in the mid-range of crack lengths from $L/3 \lesssim c \lesssim 2L/3$. Once the crack comes close

[3]Device used to acquire crack opening displacements during the experimental procedure.

to the boundary, the ligament is already quite small and the compliance increases very rapidly moving away from the exponential curve. An alternative route is to build the compliance vs crack length experimentally by loading, unloading, and reloading the specimen as soon as the crack propagates a few millimeters. We perform such a cyclic loading test by unloading the system manually (the machine has a manual controller) once the force starts to decrease and crack propagates. This cyclic procedure was then repeated 14 times (see Fig 2.6) using specimens made of PMMA. The inverse of the slope in the elastic limit of each $F - \delta$ curve provides the compliance at the respective crack length. The comparison between the normalized compliance results obtained from this experiment and FE result shows suitable agreement (see Fig. 2.5).

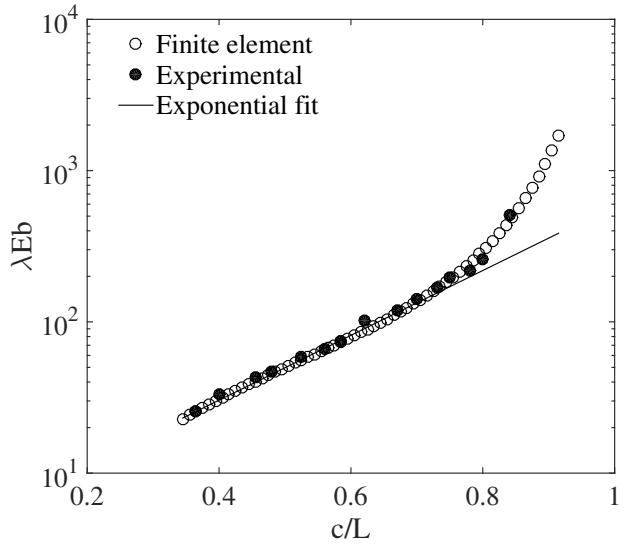

Figure 2.5: Variation of the normalized compliance with crack length. The white circles are the FE results, while the black solid line is the exponential fit of the compliance using Eq. (2.1), and black shade circles are obtained from the cyclic experiment presented in Fig. 2.6.

We then perform a systematic analysis on the scaling of the parameters of the fit by performing simulations for different geometries. We choose two different positions for the holes (for dimensions see Figure 2.7) and we vary systematically the length of the specimen. From the inset in Figure 2.7 we find that the parameter c_0 scales only with L and it scales as $c_0 = 0.39L - 91.6$ where L is given as a multiple of e_x and λ_0 scales as $\dfrac{c_0^2}{h_1 l_x}$. We also observe that this scaling is followed only for a limited range being, $60e_x \leqslant l_x \leqslant 90e_x$, $120e_x \leqslant h_1 \leqslant 160e_x$ and $400e_x \leqslant L \leqslant 1200e_x$. With this scaling, we see that for different geometries in a given range all the curves for the compliance collapse in the region containing the exponential fit. The compliance for any geometry in this range is then given by

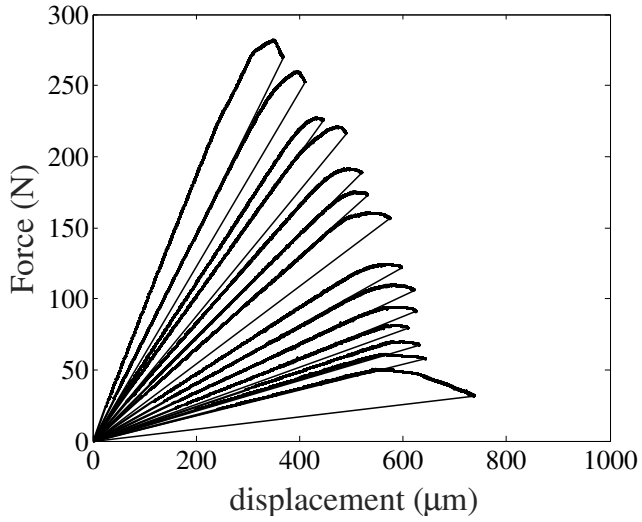

Figure 2.6: Experimental force-displacement curves for different loaded/unloaded states for the TDCB geometry. The inverse of the slope in the elastic limit gives the compliance which have been shown in Fig.2.5.

$$\lambda_F \simeq \frac{1}{Eb}\beta\frac{c_0^2}{h_1 l_x}e^{c/c_0} \tag{2.2}$$

where $\beta \simeq 3.0$ from the numerical fit. This is plotted as a solid black line in Figure 2.7.

G is given by the compliance formula, also referred to in literature as the Irwin-Kies equation

$$G = \frac{F^2}{2b}\frac{d\lambda_F}{dc} = F^2 g \tag{2.3}$$

where g is defined as:

$$g = \frac{1}{2b}\frac{d\lambda_F}{dc} \tag{2.4}$$

On substituting Eq. (2.1) in Eq. (2.4),

$$g = \frac{\lambda_0}{2Eb^2 c_0}e^{c/c_0} \tag{2.5}$$

Since the compliance has already been computed as a function of crack length, it suffices to apply Eq. (2.5) to obtain the elastic energy release rate as a function of c. In the following section, we validate this approach by computing G through two other independent approach.

Once the stress, strain and displacement fields are calculated for the FE mesh corresponding to a given crack length c, the displacement $\mathrm{u_y(r) = u_y(x = r, y = 0)(x > 0)}$ along the crack lip is measured as a function of the

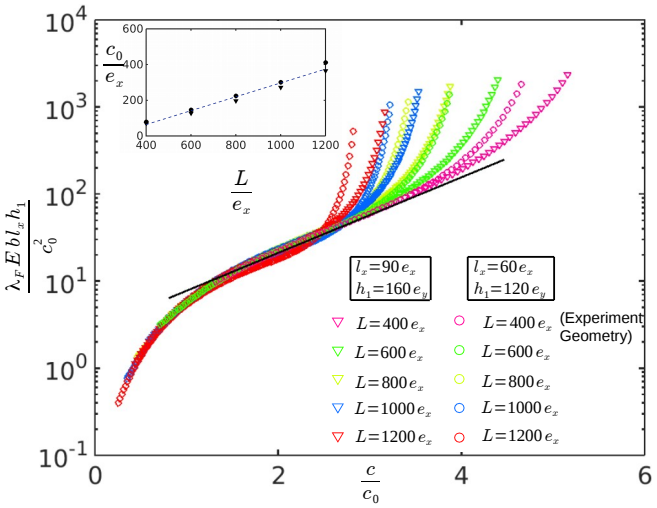

Figure 2.7: Figure shows the variation of the non-dimensional specimen compliance with non-dimensional crack length for different specimen geometries. The simulations are carried out for two different geometries with the same tapering angle α but with different l_x and h_1. Geometry 1 is represented by triangles and has dimensions $l_x = 90e_x, h_1 = 160e_y$ while geometry 2 is represented by circles with dimensions $l_x = 60e_x, h_1 = 120e_y$. The black solid line shows the exponential fit for geometry 2 and length $L = 400e_x$

distance r from the crack tip. The stress intensity factor K_I can then be inferred from the variations of u_y with r very close to the crack tip. From LEFM, we know that $u(x) \sim K_I\sqrt{x}$, so the stress intensity factor is given by fitting the crack-opening displacement solution, u(r) with r, on a log-log plot using the the Irwin equation [9, 104]

$$u(r) = \frac{K_I}{E}\sqrt{\frac{8r}{\pi}} \tag{2.6}$$

The so called Crack Opening Displacement (COD) method is illustrated in Fig. 2.8. Let us now consider the stress solution of the FE that can be written as

$$\sigma_{xx}(r) = \frac{K_I}{\sqrt{2\pi r}} + T + A\sqrt{r} \tag{2.7}$$

where T is the T-stress component. Then, once we have σ_{xx} and K_I, we calculate $\Delta\sigma$

$$\Delta\sigma = \sigma(xx) - \frac{K_I}{\sqrt{2\pi r}} = T + A\sqrt{r} \tag{2.8}$$

and plot it as function of r on a log-log scale. We expect a straight line of slope A, the value of T being where it intersects with the y-axis. Obtained values of T-stress and stress intensity factor will be further discussed in section 2.4 where we confront different approaches.

The energy release rate is then given by $G = K_I^2/E$ (see *e.g* the equivalence

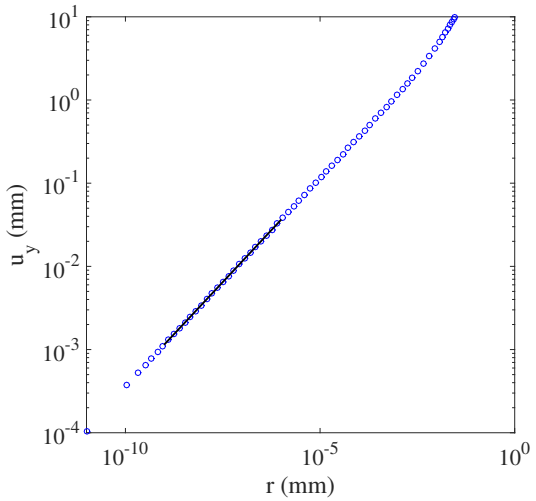

Figure 2.8: log-log representation of vertical displacements u_y as function of the position r as obtained from the FE simulation. Then K_I is calculated from the fit of this curve using Eq. (2.6) (see black solid line). The present example corresponds to a crack length of 36.5mm and gives $K_I = 22.8\text{MPa.m}^{1/2}$.

in Eq. (1.13)) and these values are calculated for different crack lengths. We now introduce a new parameter $g(c) = bG/F$. It takes inspiration from the fact that g only depends on the geometry of the specimen and G can be decomposed into a product of a term depending on the loading amplitude and another one depending on the geometry. For a unit force and thickness, we have $G = g$. We again plot the non-dimensional value of g on a semi-log scale using the scaling observed with Fig. 2.7. Let us now compare three methods: the compliance method introduced by eq. 2.3; the COD method we have just discussed; and the J-Integral (see Ref. [16]). The latter - an accurate method to calculate G using a contour integral surrounding the crack tip position - is calculated using the displacement solution from finite elements. Thus, in Figure 2.9, all three methods are confronted to verify the variations of the geometrical factor g. We find values of G in accordance with the compliance method.

As we measure the compliance, we can go from force constant (dead-weight) loading to displacement constant (fixed-grips) loading and back. If we convert equation to fixed grip loading, then we replace F in equation 2.3 with δ/λ and substituting for λ from Eq. 2.1, we have

$$G = \frac{\delta_F^2}{\lambda_F^2} g = \delta_F^2 \frac{E e^{\frac{-c}{c_0}}}{2\lambda_0 c_0} = \delta_F^2 g_\delta(c) \tag{2.9}$$

From this equation we observe that the geometrical part $g_\delta(c)$ of the elastic energy release rate under displacement controlled conditions G decreases exponentially with crack length, thus allowing us to explore different velocities and fracture energy. As we are going to perform tests with controlled displacement, if we stop it

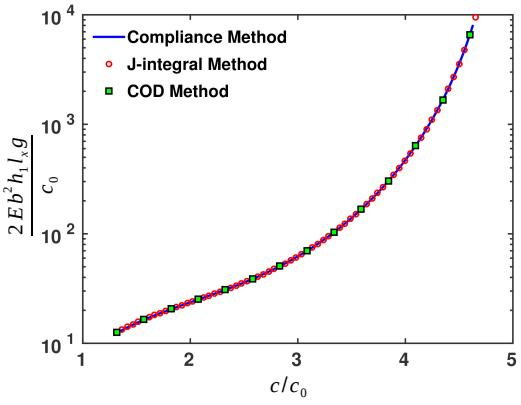

Figure 2.9: Variation of the non-dimensional elastic energy release rate g as a function of the crack length using different approaches. The figure is plotted for a specimen with $l_x = 22.5$mm, $L = 100$mm and $h_1 = 40$mm

the crack propagation will stop as well. Indeed, if c increases then g_δ will decrease very fast so G and the crack will stop. It means that the test is very stable and the faster g_δ decreases with crack length, the more stable the test is. Let us now consider other classical fracture tests like Double Cantilever Beam (DCB), Double Torsion and Compact Tension (CT). In DCB and TDCB, the compliance varies as the cube of crack length, and from equation 2.9 we have the energy release rate varying inversely as the fourth power of crack length (give citation). For the Double Torsion (DT) test, the compliance varies linearly with crack length and the energy release rate varies inversely as the square of crack length (give citation). To have a stable crack growth, it is important that the energy release rate decreases as fast as possible and as the exponential decreases the fastest in comparison to a polynomial function, we will have an extremely stable crack growth. As we will see in the following, this will be used to achieve crack propagation in very brittle solids like cement paste at controlled crack speed.

2.3 Experimental implementation

In this section, we present in detail the experimental technique adopted to study fracture and measure toughness. Experiments were carried out under uniaxial tension using a Shimadzu (model AG-Xplus) universal testing machine of 10kN maximum load capacity in the laboratory of solid and structural mechanics of the *Institut Jean le Rond d'Alembert* at the University *Pierre et Marie Curie* in Paris. Some of these tests were also performed in the laboratory of structures and materials (LabEST) of COPPE at the Federal University of Rio de Janeiro. In this experimental setup (see Figure 2.10), we have a force gauge, *i.e.* a 1kN load cell sensor, measuring the force applied to the specimen through pins located in holes of diameter 2R and a

clip gauge that measures the displacements between the lips of the crack (noted Δ in Fig. 2.3). Two steel grips were connected to the specimen by the pins placed on its both holes. The bottom one is fixed to the base and the top one that is connected to the loading sensor is pushed up by the machine stroke (crosshead). Experiments were controlled by the clip gauge opening at constant velocity, *i.e.* by the crack opening displacement (COD) rate.

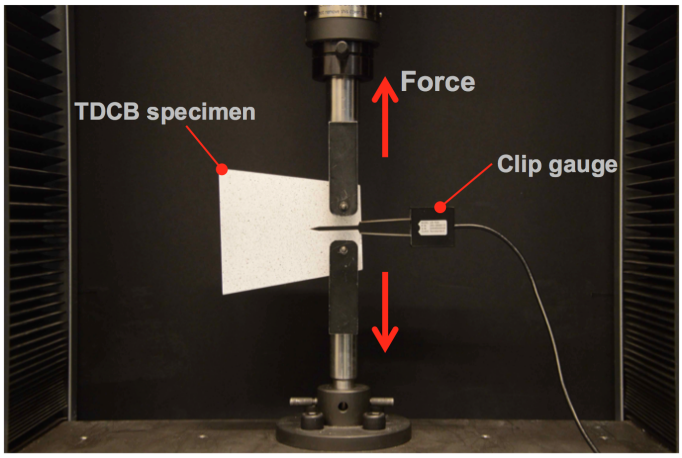

Figure 2.10: Experimental test setup used to perform quasi-static fracture tests. The electromechanic machine was equipped with a load cell sensor of 1kN, and a clip gauge device of 5 mm maximum opening to measure the applied force and the crack opening displacement, respectively.

To allow easy and smooth crack initiation and achieve stable crack propagation, different ways of sharpening the V shape notch - machined from the cutting process - were designed to initiate fracture (see Fig. 2.11): A straight prolongation of approximately 1 millimeter with a razor blade of 0.2 mm thickness; a straight prolongation of 3.5 millimeters using the laser cutting process; and a the laser prolongation allied to a pre-loading procedure of the sample under a constant 0.5 μm/s crack opening rate up to the exact moment when crack initiates. The sample was then unloaded and the new initial crack length (c_{ini} in Fig. 2.3) was recorded.

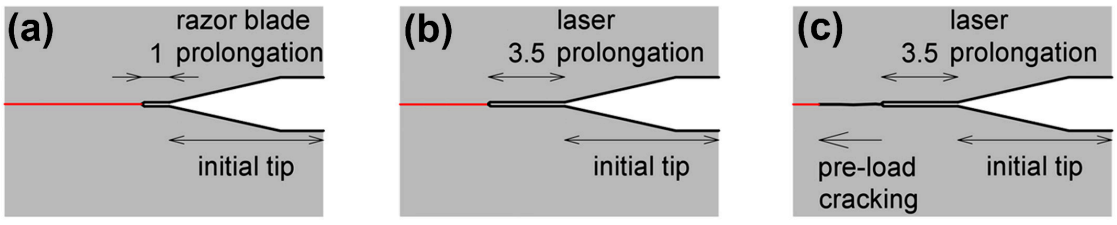

Figure 2.11: The different sharpening strategies for the initial notch preparation: razor blade prolongation (a); laser prolongation (b); and laser plus pre-load cracking (c).

2.3.1 Implementation of the method on PMMA

The objective of this section is to set the scene on the methodology developed. That means, we will describe how we link the experimental results and finite element simulation to calculate the fracture properties that are sought: crack length c, crack velocity v, and energy release rate G. Then, we display some relevant results on polymer samples and discuss the fracture phenomena that takes place.

Fracture tests were performed in a transparent thermoplastic, the so called Polymethyl methacrylate (PMMA)[4], an archetype of brittle amorphous material. Thin PMMA sheets[5] of 1210 x 610 x 8 mm (length x width x thickness) were cut using a laser machine[6] to produce tapered double cantilever beam (TDCB) specimens. Material properties and specifications are listed in Table 2.2.

Table 2.2: PMMA sheet general properties (information from the manufacturer).

Density ρ (g/cm^3)	Working temperature (^{o}C)	Melting point (^{o}C)	thickness (mm)	Color
1.19	-40 to 80	160	8	transparent

Figure 2.12 shows typical $F-\delta$ curves obtained for PMMA specimens tested at different loading rate conditions (0.5, 2.5 and 50.0 μm/s)[7]. From the $F-\delta$ curves it is possible to simply depict the behavior of the material: (i) the initial linear elastic regime corresponding to no crack propagation; then (ii) when it deviates from the linearity, close to peak force, the crack initiates; and (iii) the force decreasing regime corresponding to the crack propagating itself. Yet as the compliance is the inverse of the elasticity the Young's modulus E is then inferred from the theoretical compliance before crack initiation ($\lambda_{\text{ini}}^{\text{th}}$) and the fit of the linear regime of the experimental $F-\delta$ curve with b being the sample thickness, the Young modulus follows

$$E = \frac{\lambda_{ini}^{th} A_{exp}}{b} \tag{2.10}$$

where A_{exp} is the slope of the linear regime. Thus, the average Young's modulus results determined after 35 TDCB experiments and following Eq. (2.10) is 1.9 ± 0.4 where the variation represents one standard deviation. This value is in accordance with the typical modulus of PMMA described in Tab. 1.1 (see *e.g.* Ref. [14]).

Let us note that area under the $F-\delta$ curve represents the total mechanical

[4]The chemical nomenclature (IUPAC name) of PMMA is Poly(methyl 2-methylpropenoate) and its chemical formula is $(C_5O_2H_8)_n$

[5]The material was obtained commercially in France

[6]A CO_2 laser system from the Epilog Laser corporation. Machine model: Epilog Legend Elite Mini (60 Watts). Detailed information can be found at the corporation website (https://www.epiloglaser.com/products/legend-laser-series.htm).

[7]In particular, all these three experiments represent samples of initial notch tip sharpened by the razor blade, which led to a initial crack length of approximately 37 mm.

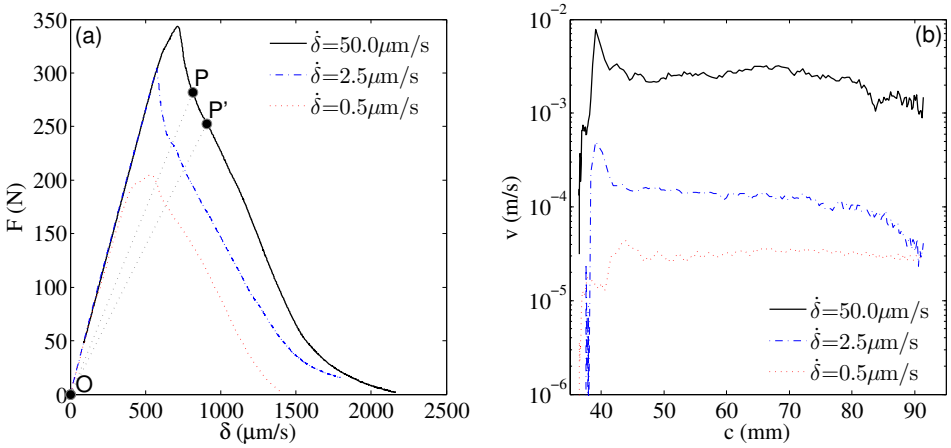

Figure 2.12: Typical force-displacement curves for different experiments on PMMA specimens of initial crack length $c_{ini} = 37$mm. These examples show how different loading rate conditions affect the experimental data results.

energy spent by the specimen during the test, thus providing a rough estimation of the fracture energy. And from the curves of Fig. 2.12(a), one observes that the larger the loading rate, the larger the area under the curve, and consequently the higher the fracture energy. Then, from Fig. 2.12(b) the higher the loading rate, the higher the crack speed. In the following section, we will investigate the variations of G_c with v more quantitatively.

Calculation of crack length and velocity

To measure the crack length (c(t)) at each time in the experiment, we use the finite element results presented in the previous section. we start from the theoretical compliance $\lambda^{FE}(c)$[8] obtained in the finite element solution and compare it with the experimental compliance $\lambda^{exp}(t) = \delta/F$. The Figure 2.13 presents the compliance method used to measure crack length from the comparison between λ^{exp} and λ^{FE}. When comparing the experimentally measured value of the compliance at some time t with the theoretical curve $\lambda^{FE}(c)$, we can infer the crack length c(t).

Once the crack tip position is obtained at each time step the crack growth velocity is then calculated as $v(t) = \dfrac{dc}{dt}$, which is shown in Figure 2.12(b) for three tests at different loading conditions (see Fig.2.12(a)). We observe a fairly constant crack growth velocity with slight variations, suggesting that the TDCB geometry provides a stable test setup indeed. This behavior is even more pronounced for low velocities, see for example the dotted curve for $\dot{\delta} = 0.5\mu m/s$. Let us insist here about the strong effect of the loading rate on the macroscopic response as illustrated on **??**. This comes from the fact that G_c varies with v and a full characterization of the

[8]Measured at the same position where it is the clip gauge device in the experiment.

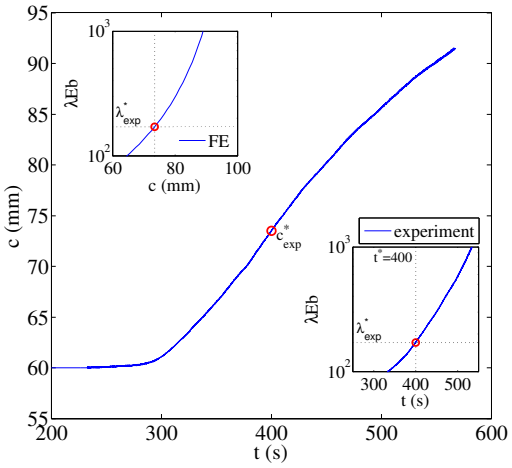

Figure 2.13: Compliance method used to measure the crack position as a function of time. The bottom inset shows the experimentally measured compliance λ_{exp} normalized by Eb as function of time in solid blue line. For a given time t^*=400 s, we have a corresponding λ^*_{exp} highlighted by the red ($\circ$). The top inset shows the the finite element solution of the compliance λ_{th} normalized by Eb *vs* crack length c (solid line). Comparing the position of λ^*_{exp} we can infer c^*_{exp} (red ($\circ$)). The main panel shows in solid blue line the inferred data for c_{exp} as function of time. The red ($\circ$) displays the position of the point corresponding to t^* and c^*_{exp}.

material fracture properties requires the determination of the curve $G_c(v)$, and not only one value of G_c as classically performed.

A word may be added here to the fact that by controlling the loading rate, it is possible to rule the crack speed as well, thus one can measures G_c for different velocities.

Calculation of energy release rate

Once we have the value of crack length, we then have two different methods to calculate the energy release rate. In the first method, we use the full finite element solution together with the J-integral (as elucidated in section section 2.2) to calculate G trough Eq. (2.3). In the second method, let us assume that the system is in the mechanical state P (see Figure 2.12(a)) corresponding to the crack length c and after an instant of time Δt it is $c + \Delta c$ at P'. The mechanical energy release rate is then given by the energy dissipated per unit area of new fracture surface. The energy dissipated E^d during this time interval Δt is equal to the area of the triangle OPP' in Figure 2.12(a). Indeed, if the specimen is unloaded from the position P, it will follow a linear behavior along the straight line (PO), while if it is unloaded from the position P', it will follow a linear behavior along the straight line (P'O). As a result, the energy dissipated in fracture between the state P and P' is well given by the area OPP'. On the other hand, the newly created fracture surface area is Δcb

where b is the specimen's thickness [82]. Thus, $G(t)$ is given by

$$G(t) = \frac{E^d(t)}{\Delta c(t) b} \tag{2.11}$$

Figure 2.14 displays G values as function of crack length computed from both methods.The area method presents higher fluctuation in its results, however, it can be explained by the high frequency of the data acquisition in the experiment. In the following, we will stick on the full FE solution based on the J-Integral as the main methodology to calculate the energy release rate and characterize material fracture properties.

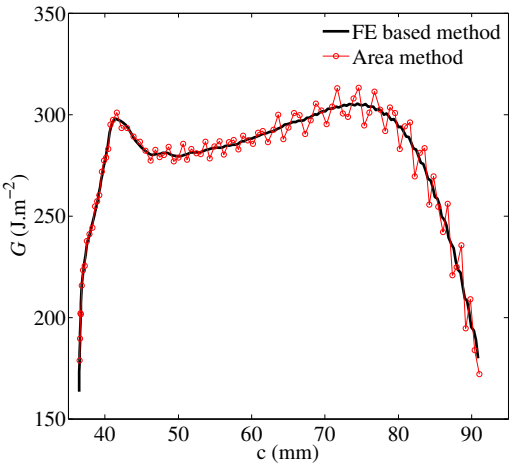

Figure 2.14: Energy release rate as function of crack length calculated from the area method and the full finite element based method for a specimen under external loading condition of $\dot{\delta} = 0.5\mu$m/s.

Variation of fracture energy with crack velocity

A set of experiments tested at different loading rate conditions were used to build a curve of fracture energy's variation as function of the crack velocity (Fig. 2.15) using only experimental data for crack lengths $40 \lesssim c \lesssim 70$ mm that corresponds to the regime with about constant velocity. This curve depicts that G increases with the velocity, as it goes from about 200 J.m^{-2} at 20-50 μm/s to 600 J.m^{-2} at 1-3 mm/s. Finally, we can state that one simple test (*e.g.* test at $\dot{\delta} = 50\mu$m/s) explores a range of G values within velocity varying over about half a decade.

From Eq. (2.2) that describes the exponential decay of the compliance with crack length, we can predict the average crack growth velocity v_m as a function of the loading rate $\dot{\delta}$. This allows us to chose the appropriate loading rate when we want to target some specific crack velocity. Using the fact that the energy release rate does not vary much with crack length (*e.g.* see Fig. 2.14). G is assumed constant

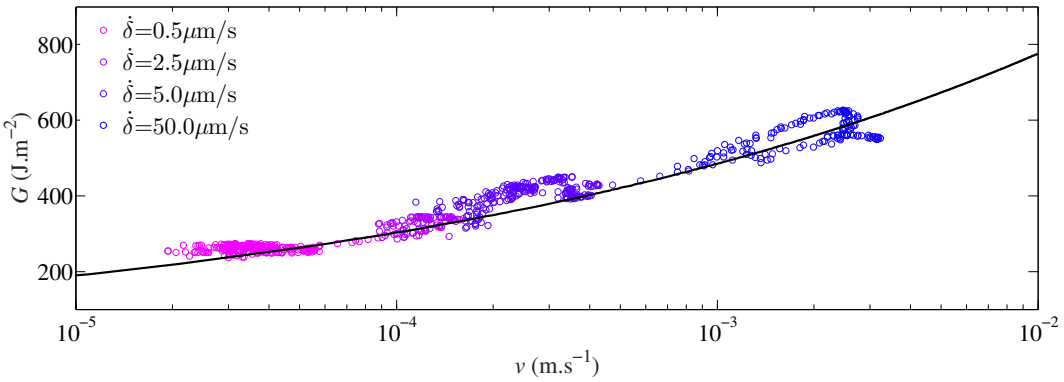

Figure 2.15: Diagram of energy release rate-crack speed ($G - \log v_)$ curve at slow crack propagation regime for brittle fracture.

during the test. The derivation of Eq. (2.9) with respect to time then leads to

$$v_m = \sqrt{\frac{2Ec_0}{\lambda_0 r G_c}} e^{\frac{-c}{2c_0}} \dot{\delta} \tag{2.12}$$

where λ_0 and c_0 are parameters obtained from the exponential fit of the compliance (see Equation 2.1). In principle, we should observe a decrease of the crack velocity with crack length over a characteristic length $c_0 \simeq 20$ mm. This is qualitatively correct, as observed in Fig. 2.12. However, as G_c slightly varies too, the agreement remains only qualitative. However, it allows to predict rather accurately the characteristic crack velocity for each test, that is defined using c = 60 mm in Eq. (2.12) and from an average of the experimentally measured crack speed in the regime 37 $\lesssim c \lesssim$ 70 mm.

Figure 2.16 shows a log-log plot of this characteristic crack growth velocity as a function of the loading rate in the range 10^{-7} m.s^{-1} $\leq \dot{\delta} \leq 10^{-4}$ m.s^{-1}. The experimentally measured crack speed and the one predicted theoretically from Eq. (2.12) shows an excellent agreement. In Fig. 2.16 the error bars represent the standard deviation of at least 3 test experiments at each loading rate. These finding show that Eq. (2.12) can be a useful tool to target a given crack velocity by selecting the appropriate load rate.

Optimal fit of the crack growth law $G_c(v)$

Achieving an accurate determination of the value of fracture energy at some given velocity remains a challenge. With the previously proposed methodology, one can achieve a precision of about 20% that is typical of experimentally determined toughness values. To improve our precision, we propose to compile several fracture tests and analyze them together through a common post-treatment procedure.

Our method relies on the assumption that the fracture properties are charac-

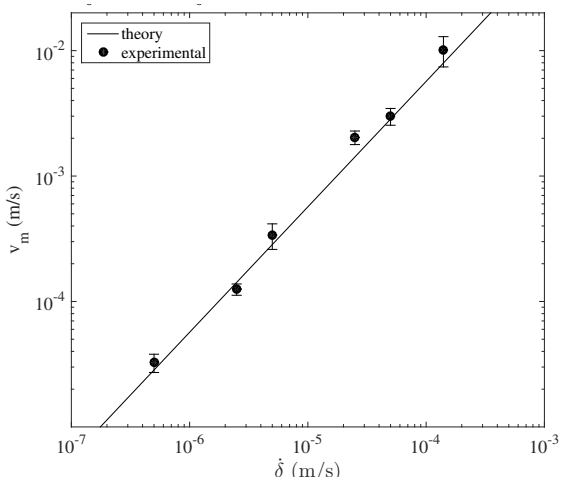

Figure 2.16: Log-log representation of the average crack velocity as a function of the applied loading rate. The straight line corresponds to Eq. (2.12), where the parameters $c_0 = 0.021$, $\lambda_0 = 4.81$, and r = 0.8 were calculated from the finite element simulations while the values $Gc = 380$ J.m^{-2} and $E = 1.82$ GPa are the characteristic fracture energy and Young's modulus for the PMMA as measured in our experiments. The Equation (2.12) is applied in c = 60 mm while the characteristic crack speed for each test is obtained from an average of the instantaneous velocity over the range $37 \lesssim c \lesssim 70$ mm.

terized by a crack growth law $G_c(v)$. Here we assume a power law variations and we are going to seek for the optimal parameter values of the crack growth law that reproduces the experimental measurements of $F(\delta)$.

By observing the nature of the $G - v$ curve, we assume a power-law behavior (solid line in Figure 2.15) according to the following equation:

$$G_c(v) = G_{c0} v^{\gamma} \tag{2.13}$$

where G_{c0} and γ are parameters of the numerical fit. Note that this type of power law behavior has already been reported in fracture experiments on PMMA [105] and has been largely assumed for other materials like rocks [90] or glass [106]. Our method then follows in three steps: (i) assume of G_{c0} and γ values for $G(v)$; (ii) from this crack growth law, predict numerically the complete evolution of crack length with time and in particular the mechanical response $F(\delta)$ of our TDCB specimens for some given loading rate; (iii) compare with the experimentally measured $F(\delta)$ curve. The three steps are repeated until the best parameter values G_{c0} and γ have been determined.

For achieving step (ii), we use Eq. 2.9 and write static crack propagation law as

$$G = G_c(v_m) \tag{2.14}$$

$$\Longrightarrow \frac{\delta_F^2}{\lambda_F(c)^2}\frac{d\lambda_F}{dc}(c) = G_{c0}\left(\frac{dc}{dt}\right)^{\gamma} \tag{2.15}$$

where δ_F and λ_F are the displacement and the compliance at the point of application of the force. We then choose $\delta_F = r(c)\dot{\delta}t$ to reproduces the experimental loading conditions. Equation (2.15) is then a first order differential equation that can be solved numerically to obtain the crack length evolution $c(t)$[9]. Once $c(t)$ is known, one can predict the force as a function of the imposed displacement $\delta(t)$ using the compliance $\lambda[c(t)]$ determined from finite element. The obtained $F(\delta)$ curve is then compared with the experimental data points. Figure 2.17(a) shows a comparison of the experimentally measured $F(\delta)$ curve with the one predicted numerically using the crack growth law parameters $G_{c0} = 1.98\text{x}10^3$ and $\gamma = 0.204$ for a TDCB fracture test with an imposed displacement rate of 2.5μm/s.

Determination of the optimum parameters of the crack growth law

To determine the optimum parameter values of the crack growth law, one must first quantify the difference between the numerical and experimental results that determines the relative error on fit of the $G-v$ curve. Interestingly, a small variation in the parameter G_{c0} or γ can induce a large error in the prediction of the $F-\delta$ curve. We define the error ϵ_{k} between the numerical and experimental $F(\delta)$ curve for the experiment k as

$$\epsilon_k = \sqrt{\sum_{\delta_i}\left[\frac{F_{num}(\delta_i) - F_{exp}(\delta_i)}{F_p}\right]^2} \tag{2.16}$$

where F_p is the half of the peak value of the experimental force and is used to normalize the error. Then, we use different experiments corresponding to different loading rates $\dot{\delta}$ to define a cumulative error as

$$\epsilon = \sqrt{\sum_{k=1\ldots n}\frac{\epsilon_k^2}{n}} \tag{2.17}$$

We finally find a minimum value of the error and the optimum values of the parameters G_{c0} and γ. The error as a function of γ and G_{c0} is shown in Figure 2.18 for the four experiments shown in Fig. 2.15 corresponding to loading rates in the range $0.5\mu\text{m.s}^{-1} \leq \dot{\delta} \leq 50\mu\text{m.s}^{-1}$. We observe a clear minimum that allow us to determine the parameters of the law accurately, *i.e.* $G_{c0} = 1.98\text{x}10^3$ and $\gamma = 0.204$. Figures 2.17(b) to (d) present the comparison between the numerical

[9]We solve Eq. (2.15) using an explicit scheme from the following discretization: $dc/dt = \mathcal{F}[c(t)] \Rightarrow c(t+\delta t) = c(t) + \mathcal{F}[c(t)]$. From the crack position at time t, one can then predict the crack position at time $t+\delta t$.

predicted and the experimentally measured crack length, crack velocity and energy release rate, respectively, using the optimum parameter values. Along with the results of crack length evolution in time, we also plot c predicted by the analytical formula of Eq. (2.2). We see that the same analysis performed using the exponential approximation for the compliance provides a good match till $\frac{c}{L} = 0.7$,[10] which is due to the fact that the compliance follows indeed an exponential behavior over a limited range of crack length values as described in section 2.2. Finally, we observe an agreement between the numerical and the experimental approaches that supports the methodology proposed here.

Overall, the compilation of several fracture tests performed at different loading rate in our post-processing procedure allows to significantly reduce the error made on the determination of G_c.

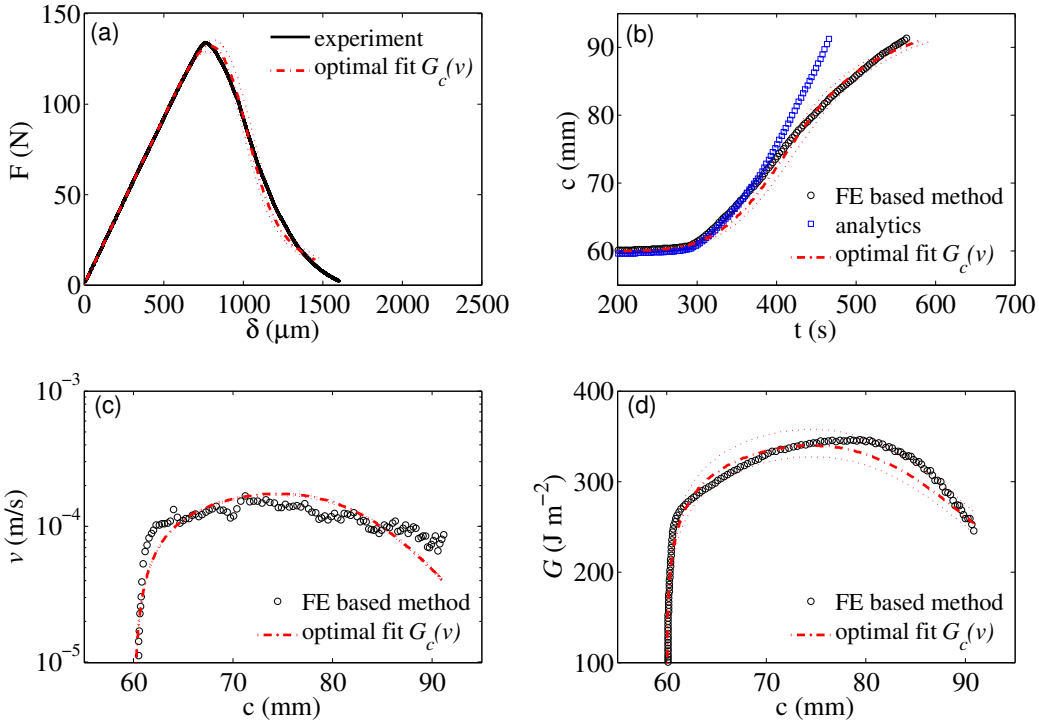

Figure 2.17: Comparison of the fracture response of the TDCB specimen of PMMA as predicted numerically from Eq. (2.15) using the crack growth law parameters G_{c0} = 1.98x10^3 and $\gamma = 0.204$ with the experimental measurements for $\dot{\delta} = 2.5\mu$m/s: $F vs \delta$ in (a); c *vs* t in (b); v *vs* c in (c); and G *vs* c in (d). In (c) an analytic prediction of crack length according Eq. (2.2) is also displayed. The two thin dashed lines in each graph represent the 10% error bars in respect to the parameters of the numerical fit.

[10]Where c is the crack length at a certain time interval and L is the length of the specimen.

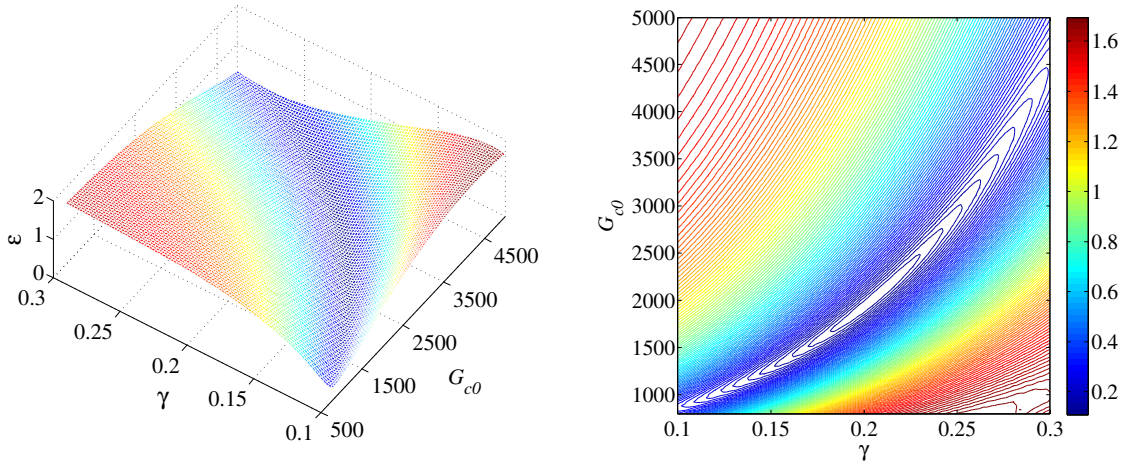

Figure 2.18: Error plot ϵ as function of the crack growth law parameters (left); and the contour representation of the error, where it is interpreted as heights with respect to the G_{c0}-γ plane (right). This procedure provides the parameters $G_{c0} = 1.98\text{x}10^3$ and $\gamma = 0.204$ used in Fig. 2.17 for a direct comparison between the numerically predicted and the experimentally measured fracture behavior of a TDCB specimen of PMMA at the imposed loading rate $\dot{\delta} = 2.5$ μm/s.

2.4 Alternative approaches for estimating material toughness and crack tip position

The methodology proposed previously is relevant for numerous applications in the field of materials characterization. However, for some of them it might be impossible to use connected devices like clip gauge to record displacements data, *e.g.* when submitting materials to extreme temperatures to explore its effects on the fracture energy or when working with extremely weak or soft materials, in which just fixing the device to the specimen may break or deform it. Thus, alternative methods such as optical measurement techniques might be more appropriate. They take into account the whole sample without handling and cluttering yet enabling to obtain information close to the boundaries. In this section, two examples are explored. In the first one, we make use of the PMMA transparency with basic image post-processing from the pictures taken during the test that allow us to extract crack length as function of time. The second one is the so called Digital Image Correlation (DIC). In particular, we performed a study using a recently developed method, the Integrated DIC [107, 108] that enables to extract relevant mechanical information during the experiment.

Image analysis approach for tracking crack growth in transparent materials

Pictures acquisition were performed with one CMOS camera (Baumer HXC20 digital monochrome full progressive scan camera, 2048x1088 pixel, up to 337 fps). A Zeiss fixed lens (100mm F2, model Makro-planar T*) and a Nikon extension tube (52.5 mm, model PN-11) are used, aiming at the target (transparent specimen surface). The working distance, around 70 cm, is acceptable in terms of cluttering. The pixel size corresponds to about 4μm on the target with this magnification. Figure 2.19 displays a typical picture of the specimen's surface target acquired for the image analysis.

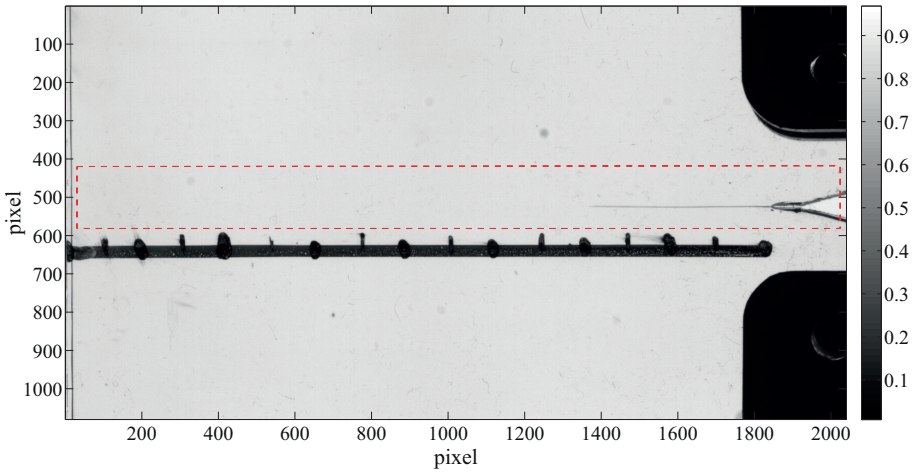

Figure 2.19: Picture example of a TDCB specimen lateral surface during crack propagation. We use here a transparent material, the PMMA, that enabled the application of this crack tip detection algorithm. Dashed line shows the region of interest selected for the analysis.

The region of interest (ROI) covers part of the image whose size is 1080 x 2040 pixels with 8 bits digitization, which means that their gray levels can have at last $2^8 = 256$ different values from white (1) to black (0). They were analyzed with frame rate set varying between 1 to 10 Hz according to the sample load velocity imposed. We adopt one pixel by a vertical index i and a horizontal j, both of them are integers. Then image $\mathrm{I}(i, j)$ corresponds to the gray level of pixel (i, j). Finally, the tip position will be $\mathrm{h}(i, t)$ where t is time (step between images), i the tip pixel, so the coordinates $(i, h(i))$ of a gray level $\mathrm{h}(i, h(i))$.

Image analysis enabled us to extract the crack tip position from a numeric image. The algorithm developed here works to provide the position of the crack in each image taken. Then, the general idea to do so is to have a binary image where we will identify 2 simple regions (objects) in black and white: a cracked and non-cracked

one. First, we define a region of interest (ROI), which will be analyzed indeed[11]. Then, we need to define a threshold looking at the gray level values along the crack path. Figure 2.20) presents a picture of the region surrounding the initial crack path in (a) and its corresponding gray level profile in (b). The high values of gray level correspond to the darker zone, *i.e.* the cracked region, and the low values correspond to the lighter zone, *i.e.* the non-cracked part. Thus, the region where the gray level starts to to change abruptly defines the threshold.

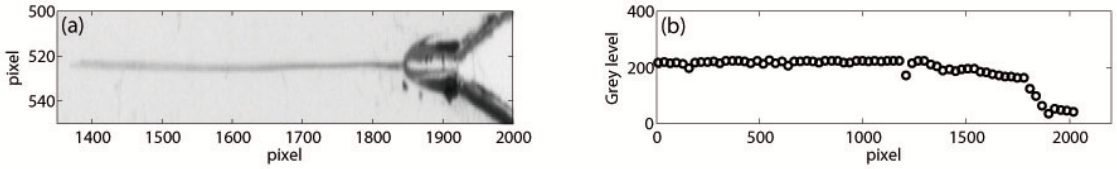

Figure 2.20: (a) Zoomed region of the zone surrounding the crack path. (b) gray level profile along the crack path.

Once we have fixed the threshold value of the gray levels along the crack path, the next step is to convert the gray level image to black and white, so determining the tip position comes down to find the coordinates of the most advanced black element along the crack path. Figure 2.21 displays the sequence of binary image processing that precedes the extraction of the crack length. As we have imperfections in the images that may come from different sources, *e.g.* heterogeneity in lightening the target or dust in the surface, it is necessary to eliminate them as illustrated in Fig. 2.21(d). In the end, all images are processed to become similar to the one presented in Figure 2.21(e) so they allow for a straightforward determination of the crack length.

Fracture tests under three different external loading conditions were analyzed using this imaging technique to compare with compliance methods based on the full finite element results. Figure 2.22 displays the variations of crack length $\Delta c{=}c(t) - c_{\text{ini}}$ as function of time. In particular, we can observe that the correlation between both method loses accuracy when slowing down the applied load and, for this cases, the image analysis response says that the fracture supposes to propagate slightly faster. This can be explained by the fact that the crack is so thin close to the tip that we certainly do not succeed to identify it when approximating to the very end of the experiment. However, all the results of the experimental test allied to FE simulations present a reasonably good agreement with the image analysis based measurements.

The previous results suggests that this methods is promising and can be used as an alternative to the compliance based method. Indeed, it can be further improved

[11]

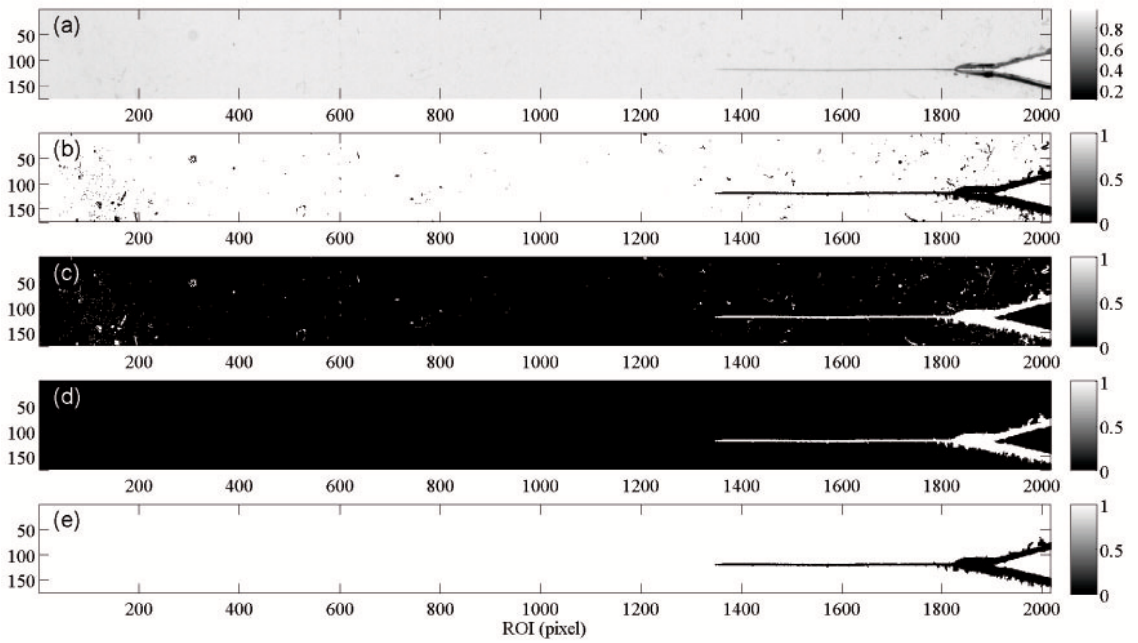

Figure 2.21: Illustration of the crack tip detection algorithm.

by, for example looking at the crack from a different angle position with respect to the normal of the sample surface, so we can see the crack front and surface advancing. In other words, one can takes into account the fact that the crack front does not advance perfectly normal to the surface, though being more precise when identifying the tip position.

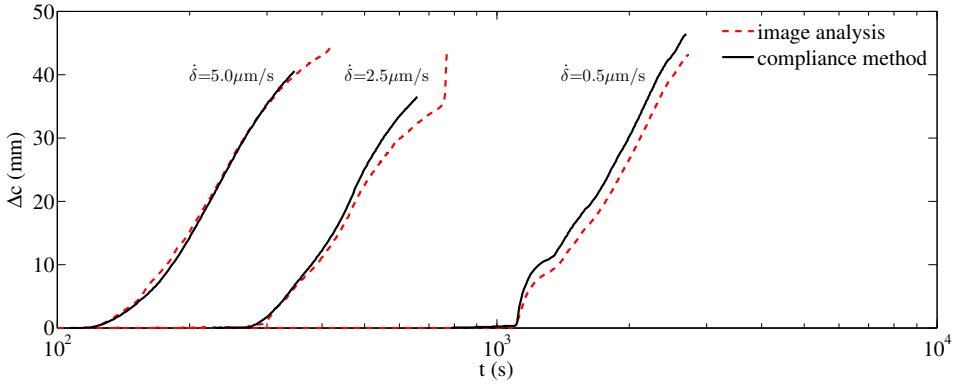

Figure 2.22: Variation of crack length Δc as function of time for PMMA specimens tested at different loading rates. Comparison of c measured by image analysis, and by the compliance method.

Estimation of stress intensity factors from an Integrated Digital Image Correlation (IDIC) technique

In this section, we present a method of determination of the fracture properties using digital image correlation (DIC)[109, 110]. This can be an interesting alternative to the compliance method proposed previously when a clip gauge cannot be used (for example for high temperature test, for dynamic fracture or for very peculiar types of materials). TDCB fracture tests were performed at the same laboratory conditions described in section 2.3. Picture acquisition follows the same routine described previously in the image analysis approach. The only difference regards to the specimen's surface that was covered with a black and white speckle pattern. An Integrated Digital Image Correlation (I-DIC) algorithm[107, 108, 111] was performed in a collaborative work with François Hild and Jan Neggers at the *Laboratoire de Méchanique et Technologie* (LMT) of the *Ecole normale supérieure de Cachan* (ENS Cachan), in France.

The objective here is to demonstrate a set of results obtained with a different technique and thus we will rapidly describe the fundamentals of the I-DIC methodology followed by some data results without going deep in the full theory. DIC has been successfully used for various problems of experimental mechanics [109, 110] since 1980's.

The integrated digital image correlation approach evaluates the amplitudes of the displacement fields in Williams' series [112]. In other words, the parameters are chosen to get the displacements that better describes the experiment, where the sought amplitudes are directly evaluated at the pixel level. Basically, DIC and I-DIC are grounded on the gray level conservation between two images - a reference, f, and a deformed one, g. Meaning, in the absence of noise, that f can be written as function of g and $u(x)$ - a vector representing the displacements for each position in the image - as following

$$f(x) = g(x + u(x)) \tag{2.18}$$

We seek to determine the displacement field u that minimizes the difference between both terms. This difference is written as the sum of squared differences over the region of interest (ROI) and follows

$$\phi = \sum_{ROI} (f(x) - g(x + u(x)))^2 \tag{2.19}$$

The displacement fields u may be expressed based on shape functions. For example, a series of mechanically meaningful fields Ψ_i (e.g. Willliams' series) with unknown amplitudes ν_i (e.g. SIFs) as the parameters

$$u(x) = \sum_i \nu_i \Psi_i(x) \tag{2.20}$$

so ϕ will depends on the vector ν gathering all amplitudes ν_i.

According to Mathieu *et al.*[113], assuming crack path along the negative x axis, and crack tip position at the origin, the displacement fields can be then rewritten as

$$u(z) = \sum_{j=I}^{II} \sum_{n=pi}^{pf} \omega_n^j \psi_n^j(z) \tag{2.21}$$

where the vector fields defined in the complex plane are

$$z = x + yi = rexp(i\theta) \tag{2.22}$$

with, $j = I$ for a mode I fracture regime

$$\psi_n^I = \frac{A(n)}{2\mu\sqrt{2\pi}} r^{\frac{n}{2}} [\kappa exp(\frac{in\theta}{2}) - \frac{n}{2} exp(\frac{i(4-n)\theta}{2}) + (-1^n + \frac{n}{2}) exp(-\frac{in\theta}{2})] \tag{2.23}$$

and $j = II$ for a mode II regime

$$\psi_n^{II} = \frac{iA(n)}{2\mu\sqrt{2\pi}} r^{\frac{n}{2}} [\kappa exp(\frac{in\theta}{2}) + \frac{n}{2} exp(\frac{i(4-n)\theta}{2}) + (-1^n - \frac{n}{2}) exp(-\frac{in\theta}{2})] \tag{2.24}$$

where κ is $(3-\nu)/(1+\nu)$ for plane stress conditions, μ the Lamé's constant, ν the Poisson's ratio, r the distance from the crack tip, θ the angular position, and $A(n)$ defined as

$$A(n) = \cos(\frac{n\pi}{2})^2 + \sin(\frac{n\pi}{2}) \tag{2.25}$$

The sensitivity fields, obtained from equations 2.23 and 2.24 above, multiplied by the amplitudes ω_i^j provide the sought displacement fields. The amplitudes ω_0^I and ω_0^{II} correspond to rigid body motions (Fig. 2.23(a) and (d)). Amplitudes ω_1^I and ω_1^{II} give access to SIFs for mode I (K_I) and mode II (K_{II}), respectively (see Fig. 2.23(b) and (e)). The amplitude ω_2^I provides the T-stress component (Fig. 2.23(c)) and the ω_2^{II} gives rigid body rotation (Fig. 2.23(e)).

The crack tip position is then found following on a criterion that is the vanishing of the first super-singular term's amplitude of the Williams' expansion, *i.e.* the field ψ_{-1}. From Eqs. 2.23 and 2.24 within negatives values of n, super-singular terms of the Williams' series arise near the crack tip [111, 114]. Thus, crack tip position is

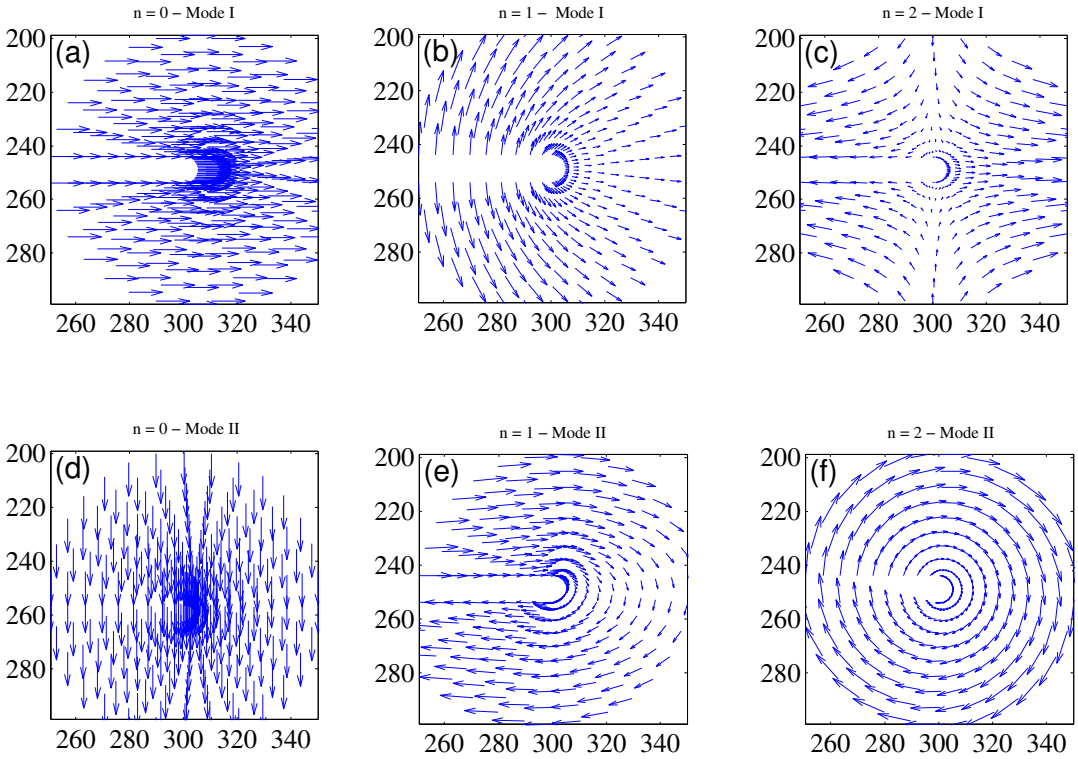

Figure 2.23: Displacement fields for mode I and II: The ones related to rigid body translations ψ_0^I (a) and ψ_0^{II} (d); the stress intensity factors ψ_1^I (b) and $\psi_1^{II}(e)$; and the so called T-stress ψ_2^I (c) and rigid body rotation ψ_2^{II} (f).

obtained by canceling out the amplitude ω_n^I when $n = -1$ and $r = 0$

$$da = \frac{2\omega_{-1}}{\omega_1} \tag{2.26}$$

providing a crack tip shift to find the correct solution. Figure 2.24 displays the singularity at the crack tip when the first super-singular fields are ψ_{-1}^j.

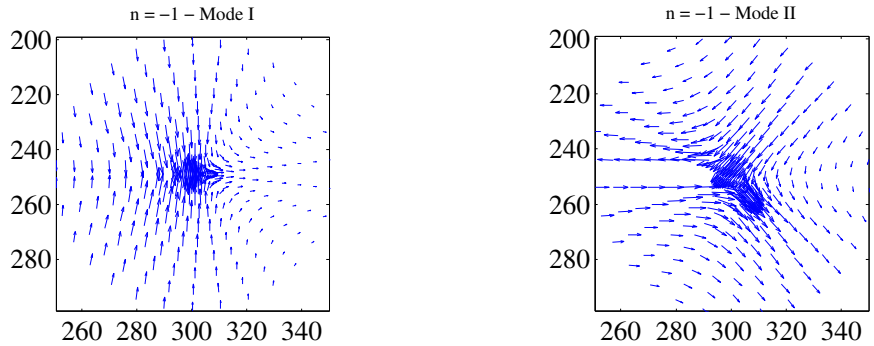

Figure 2.24: Williams' fields ψ_{-1}^I (left) and ψ_{-1}^{II} (right) that shows the singularities close to the crack tip (image center). The amplitude of these terms vanishes when the crack tip is located at the proper position.

Let us highlight here that this approach computes sub (n $<$ 0) and super (n

> 0) singular displacement fields of order n in the range p_i to p_f. In other words, as described in Eq. (2.21), the series has to be truncated (between p_i and p_f) so we can solve it numerically. Although, super singular terms are optional, the proposed approach accounts for $p_i = -1$ to estimate the crack tip position as presented in Eq. (2.26), and $p_i = -3$ to evaluate the process zone size [115]. On the other hand, the sub singular terms accounts for the fact that the crack extends itself up to a finite length. In a previous study, Henninger *et al.* [115] showed that for a square specimen of a material prescribed to as very small hardening regime with an elastic-plastic behavior the stress intensity factor results were stable for $p_f = 8$. Nevertheless, as our experiments relates to a different class of material (the PMMA), we carried out the influence of the number of terms. Figure 2.25 displays typical K_I and crack length determinations[12] for selected positions along a set of pictures (*i.e.* along the propagating crack). These results highlight that adding more fields improves the convergence values. In general, $p_f = 9$ seems to describe well the experiments in TDCB specimens of PMMA, although in the case of image 60 the results starts to converge only after $p_f = 10$. It is worth nothing that image 60 corresponds to a few seconds prior to the end of the test, which means that the crack extension is approximating to the boundary and test results becomes less precise.

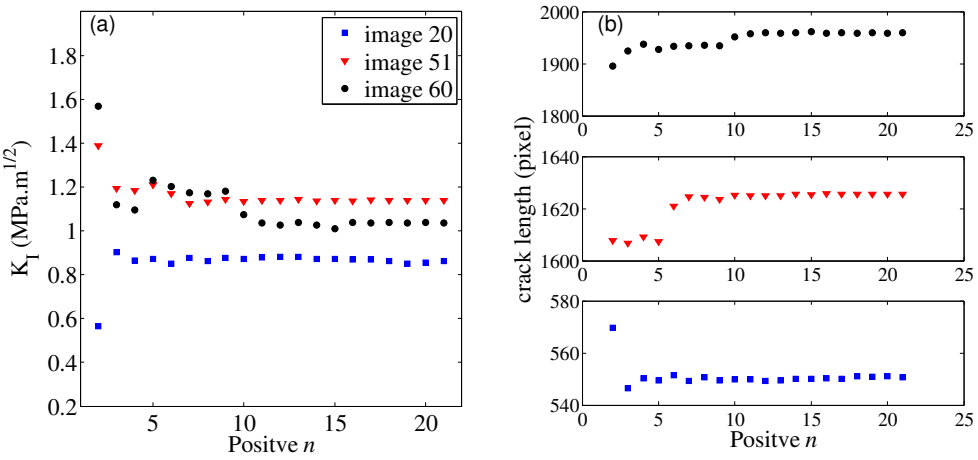

Figure 2.25: Stress intensity factor K_I and crack length at different loading phases after crack initiation vs. maximum order n in Williams' fields.

Figure 2.26 displays the evolution of crack length, SIFs and T-stress for a specimen tested at 5μm/s opening rate with an initial crack length of 60 mm (induced by the pre-load cracking procedure). In general, when comparing the IDIC to the compliance methods, both approaches present similar results but, with some additional fluctuations on the values of T-stress and K_I obtained using the IDIC method. K_I remains almost constant around 1 MPa.m$^{1/2}$ after crack initiation. This is con-

[12]Corresponding to three different pictures among 66 in total that were considered for this analysis.

sistent with the nearly constant crack velocity. This value is in agreement with the fracture energy measured from the compliance method, after using Irwin's relation $K_I = \sqrt{EG_c}$. As demonstrated before, this approach allows to compute the presence (or absence) of mode II fracture as well. Here, we find that K_{II} equals roughly to zero all along propagation. This is consistent with the criterion of local symmetry [116, 117] that predicts that cracks propagates along a path that satisfies $K_{II} = 0$ (here, a straight path perpendicular to the loading axis).

We also measure through I-DIC a positive T-stress, T $\simeq$ 2 MPa, that indicates a tensile state of stress. This value is consistent with the T-stress determined from finite element using the fit of the numerical solution with Eq. (2.8). Note that a positive T-stress is often assumed to give rise to non-straight crack path [116, 118]. In our experiments, we observe that a positive T-stress do not necessarily imply a non-straight crack trajectory. We believe here that crack path stability is ensure by the value of the parameter A in Eq. (2.8) that is found to be negative in our finite element simulations, and so that stabilizes the crack.

Let us now highlight that our IDIC results show some variations of the SIF with crack length that we could not explain oscillations on the mechanical response. For example, considering the branch of c values between 65 to 90 mm that corresponds to a plateau of SIF results according to the compliance method, we observe K_I fluctuations of about 0.3 MPa.m$^{1/2}$. In a recent work, Réthore [111] also observed small fluctuations on SIF and T-stress values that he could not explain. This particular point would deserve further work.

But overall, our IDIC analysis show promising results and appears as a reliable method to determine the fracture toughness of our materials in the TDCB configuration. Let us note that this method has already been successfully employed to determine fracture properties of different brittle [107, 108, 119] or ductile [113, 114] materials. Nevertheless, in the particular case of the TDCB geometry in PMMA demonstrated above, it appears to be less precise than the direct measurement through the compliance method assisted by FE calculations.

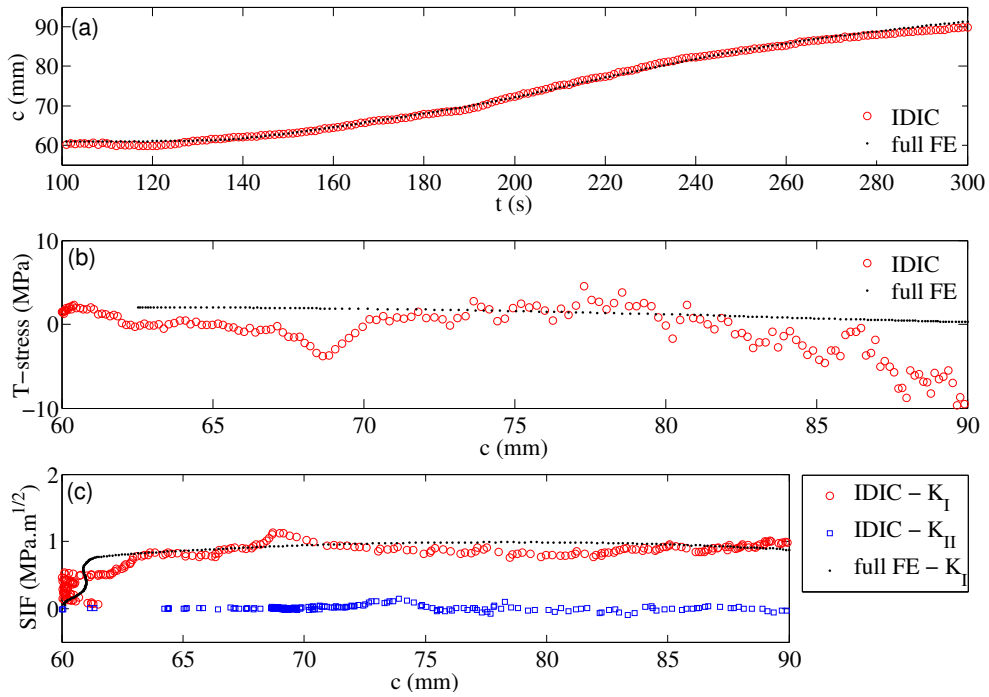

Figure 2.26: Crack length as function of time (a), stress intensity factor (b) and T-stress (c) as function of crack length obtained by IDIC and compared to the full FE methodology.

2.5 Concluding remarks

This chapter reports a combined theoretical and experimental methodology using a new simple geometry - based on tapered double cantilever beam - to study mode I tensile fracture in brittle materials. We confirm that the tapering geometry makes the crack growth extremely stable, which allow us to measure the energy release rate accurately. Also we have shown an exponential dependence of the compliance with crack length, which explain why the geometry is really stable. The experimental TDCB fracture test has also been useful to obtain the $G_c(v)$ kinetics of the material. We have demonstrated with just a few tests that it is possible to explore a large range of crack velocities and energy release rate determinations. Furthermore, we have proposed an optimization based strategy to calculate the optimum parameters of the $G_c(v)$ characteristics. This method has enabled us to predict the fracture properties of the material numerically minimizing the error, which was proved by a satisfactory accordance with the direct experimental $F - \delta$ response and the experimentally measured fracture parameters based on the compliance method.

Furthermore, two alternative approaches have given even more arguments to the validity of this proposed TDCB methodology. First, an image analysis that track the crack tip positioning during the experiment in transparent materials confirmed the crack length determinations acquired by the compliance method using the finite

element solution for the tapering geometry. Then, a more sophisticated imaging technique - the IDIC - have also determined mechanically meaningful parameters rather than only crack positioning. Its measurements of stress intensity factor K_I, T-stress, and crack length had a satisfactory agreement with our FE based method. Also, $K_{II} \simeq 0$ obtained with the IDIC technique has allowed us to endorse the absence of mode II in our experiment.

Chapter 3

Hydration properties of cement pastes with recycled inclusions

The heterogeneity of CDW is one of the major concerns in the effectiveness of its applicability in structures and materials related to civil engineering. After a series of state-of the-art reports [30, 32, 37] it is possible to assert that an amount superior to 70% of the CDW's total mass is composed by concrete and ceramic materials. In a comparison to recycled aggregates from different sources, Lima *et al.* [58] emphasize the same mineralogical composition of CDW and the possibility of new cementing materials as advantages. Therefore, find solutions to achieve homogeneous wastes is an important topic to further analysis and comparison to the cementing raw materials characterization. Furthermore, recycling CDW with only one crushing action - by a jaw or impact crusher - produces coarse and fine aggregates in similar proportions of approximately 50 wt% exhibiting high levels of a remaining dust powders (particles < 75 μm) [63].

In the present work, we stick the objective on the influence of these fine powders as supplementary cementitious material. Therefore, we first depict the origin, the recycling and crushing processes, and the selection of each recycled material. Then, their physico-chemical properties are experimentally obtained.

In order to understand the robustness of our propositions, we confront the evolution of three recycled powders on the properties of cement pastes, since the anhydrous mixture until their maturity with reference pastes without any recycled inclusion. A particular section is devoted to depict the mixture composition of the five cement pastes studied as well as the experimental methods of characterization. Finally, this chapter is closed with a general discussion about the effects of the recycled powders on the hydration-related properties of cement pastes.

3.1 Materials and methods

In this work, the recycled materials were originated from two different construction components: concrete and masonry. As heterogeneity is a central concern when reusing CDW[1], the raw materials selected to be recycled come from sources with known information: (i) a laboratory concrete beam structure; and (ii) clay bricks for masonry construction. The objective here is to implement a fundamental research about the influence of recycled demolition waste on understanding its effects on cement blends.

A class G cement with no mineral addition[2] [120, 121] was adopted to better qualify the effects of the recycled additions as supplementary cementitious materials. Deionized water was used in the production of cement pastes. Lastly, a quartz powder was used to produce one mixture with a recognized inert[3] material and confront its influence against the ceramic and concrete wastes.

3.1.1 Recycling procedure

As mentioned previously, the recycled powders were originated from concrete and ceramic. Thus, the first is derived from the crushing of six reinforced concrete beams (see Fig. 3.1(a)) developed for study the cyclic behavior of strengthened structural elements by Vaz [122]. Detailed information about the mix-design and the mechanical behavior of the original concrete is presented in Appendix B. Then, the recycled ceramic powder came from the crushing of two different types of red ceramic bricks: face and hollow (or perforated) (illustration in Fig. 3.1(b) and (c), respectively). Both brick types are commercially available in the metropolitan area of Rio de Janeiro and usually adopted in Brazilian building constructions.

Before crushing the concrete rubble from the demolition of the beams, they were homogenized. During this process, the material is distributed in homogeneous layers throughout a defined length onto a plastic sheet. Starting from the middle section, the layers were subdivided in several sections denominated cells characterized by homogeneous constituent part types. This method comes from the iron ore treatment guidelines reported by the *Centro de Tecnologia Mineral* (CETEM) in *Rio de Janeiro*. It has already been adopted to homogenize recycled rubble from the demolished structure of a hospital (see details in Ref. [123]).

Quartz rocks, concrete waste[4], and ceramic bricks were crushed using the same

[1] In which has concrete and masonry wastes as its major constituents.

[2] Nowadays in Brazil, the commercialization of Portland cement type I becomes unusual, then obtain it could be such a hard task. Therefore, a special cement for well cementing industries - Brazilian CPP Class G cement - was chosen since it is really pure as well.

[3] Controversy might exists about the certainty of quartz being inert depending on the fineness of the material.

[4] After the homogenization procedure.

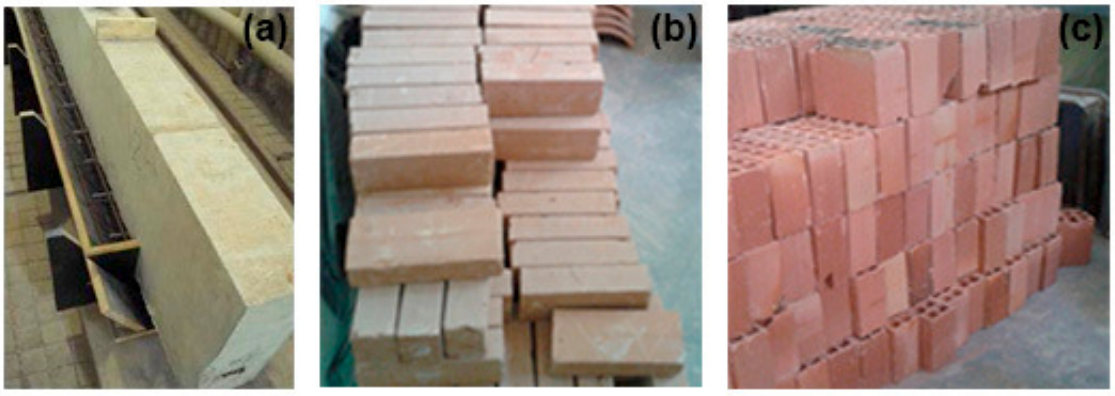

Figure 3.1: Construction components used to produce the mineral additions. Laboratory concrete beam (a), face brick (b), and hollow brick (c).

methodology[5]. An automatic jaw crusher[6] was manually feed crushing any material into two particle size fractions: fine and coarse. In order to acquire the equivalent aggregate size particles in accordance to Brazilian standard NBR 7211 [124], the coarse content was sieved between meshes nº 3/4 and 3/8 in (19 and 9.5 mm) and meshes nº 3/8 in and nº 4 (9.5 and 4.75 mm). The fine content was here sieved between meshes nº 4 and 200 (4.75 and 0.075 mm). Then, the particles of each material passing through mesh 200 were storage to study its behavior as supplementary cementitious material. All the coarse particles retained in the 3/4 mesh were, at that point, re-crushed until fit some of the defined particle size fractions. Finally, all particle fractions were also homogenized[7] before its characterization. To classify all the recycled material fractions generated after the crushing and homogenization procedure the following nomenclature was defined in Table 2 as a schematic description.

Table 3.1: Particle size d classification (in mm) and schematic description of the fractions generated by the crushing and homogenization process. The materials highlighted in bold are the ones to be investigated in the present work.

Source material	Size classification			
	$19 < d < 9.5$	$9.5 < d < 4.8$	$4.8 < d < 0.075$	$d <$ **0.075**
Recycled concrete	RC1	RC2	RCS	**RCP**
Face brick	FB1	FB0	FBS	**FBP**
Hollow brick	HB1	HB0	HBS	**HBP**
Quartz	Q1	Q0	QS	**QP**

In this work, our goal is to understand the effects of microstructural variations

[5]In order to obtain similarity between particles.

[6]The automatic jaw crusher (named as Queixada 200) is an equipment for small grinding plant. It is commercially available in Brazil by the Vegedry company (detailed information could be found in www.vegedry.com.br).

[7]According to the same procedure described in the last paragraph.

on the hydration-related and fracture properties of cement-based materials. Thus, we stick on the micro particles of $d < 75$ μm to asses its effects as supplementary cementitious materials in cement pastes. Although an abbreviation has been suggested in Table 3.1 for the different particle size classes, as we will work with only one class, let us simplify the nomenclature of these particles along the remaining of the manuscript using the proper name of their sources when referring to one of them.

3.1.2 Characterization of the supplementary cementitious materials (SCM)

Table 3.2 shows the chemical composition of the materials measured semi-quantitatively using X-ray fluorescence analyzer (Philips PW 2440 with 3 kW tube and rhodium target). Of particular interest is the high levels of silicon dioxide, calcium oxide and aluminium oxide of the recycled concrete powder. Ferric oxide as well as potassium oxide are also presented. The powders from ceramic bricks (both face and hollow) reveal high levels of silicon dioxide, aluminium oxide, and ferric oxide besides some other metal oxide impurities. Regarding the chemical composition of quartz, it is about a material of high level of purity (94.36 wt.% of Sio_2).

Specific gravity was conducted using a helium (He) gas pycnometry (Accupyc model, Micrometrics). The method consist in determine the volume of a known sample mass through the gas pressure variation in a standardized volume. The results are summarized in Table 3.2. While the crushed and sieved materials present values raging between 2500 to 2800 kg/m^3, the cement particles present 3270 kg/m^3.

BET specific surface area was determined using a nitrogen adsorption apparatus (ASAP 2020 V.3.01 from Micrometrics). Before the analysis, the samples were degassed at 200°C for 16 h at a heating rate of 10°C/min. In particular, the recycled concrete powder was treated up to 100°C to avoid any phase decomposition. Of particular interest, the BET results clearly indicate that recycled powders have higher specific surface area than the quartz powder of same size range and cement particles, especially the ones coming from clay bricks.

X ray diffraction analyzes were performed to characterize the crystalline phases by using a Bruker D8 Focus model diffractometer with monochromatic copper radiation ($Cu_{K\alpha}, \lambda = 1,5418$Å), operating at 30 kV and 40 mA. Angular scanning speed of 0.02°/s, aquisition time of 1 second, and measurement intervals between Bragg angles (2θ) of 3° and 60° were used. Samples were compacted in the equipment specimen's holder. Figure 3.2 shows the X-ray diffraction patterns, where it highlights (in (a)) for the absence[8] of C_3A, which defines the cement type as resistant to

[8]It is worth noting that colorimetry analysis would reveal low levels of C_3A.

Table 3.2: Physical characteristics of the materials: (ρ) Specific gravity; (BET) BET specific surface area; (d) D_{50} particle size. And the chemical composition (wt.%) in terms of oxides of the raw materials.

Characteristic	Cement	Concrete	Face brick	Hollow brick	Quartz
ρ (kg/m^3)	3270	2560	2750	2770	2730
BET (m^2/g)	0.43	6.19	24.45	21.40	0.36
d (μm)	17.45	37.77	34.83	42.82	33.24
Oxides (wt.%)					
SiO_2	18.80	44.56	50.06	48.51	94.36
Al_2O_3	-	11.59	35.97	37.12	4.31
Fe_2O_3	5.74	4.90	6.36	8.30	0.06
CaO	69.95	29.59	0.58	0.48	0.77
K_2O	0.59	3.70	3.87	1.59	-
SO_3	4.15	2.51	1.40	1.41	-
MnO	-	-	0.13	-	-
P_2O_5	-	1.89	-	0.97	-
TiO_2	0.23	0.81	1.42	1.38	-
SrO	0.29	-	-	-	-
ZrO_2	-	-	0.13	-	-
LOI[a]	0.22	17.76	0.97	1.59	0.43

[a] Loss on ignition

sulfate attack [125]. For the fine powder of concrete beam waste (see Fig. 3.2(b)), the data shows that quartz is the major crystalline phase and a few peaks of biotite and sanidine are the other phases. Nevertheless, the portlandite and calcite phases should be highlighted, thus indicating the existence of hydrated cement grains. The X ray diffraction of the ceramics (see Fig. 3.2(c) and (d)) presents quartz as their major crystalline phase and illite as a common both ceramic materials. Microcline is another phase presented in the face brick powder.

The morphology of the materials was qualitatively characterized with the aid of scanning electron microscope (SEM) images. The micrographs were taken under backscattered electrons mode using a FEI Quanta 400 equipment operated under an accelerating voltage ranging from 10 kV to 20 kV. A gold layer coating was done in order to enable samples to become conductive. The analysis were realized in the *Laboratório Multiuso de Caracterização Tecnológica* of CETEM. Figure 3.3 displays the morphology of all particles, indicating irregularly shaped grains and a wide range of sizes. In particular, we can highlight the rough surface of the recycled concrete and brick particles.

It is of relevance in this study to figure out how the crushed particles were dis-

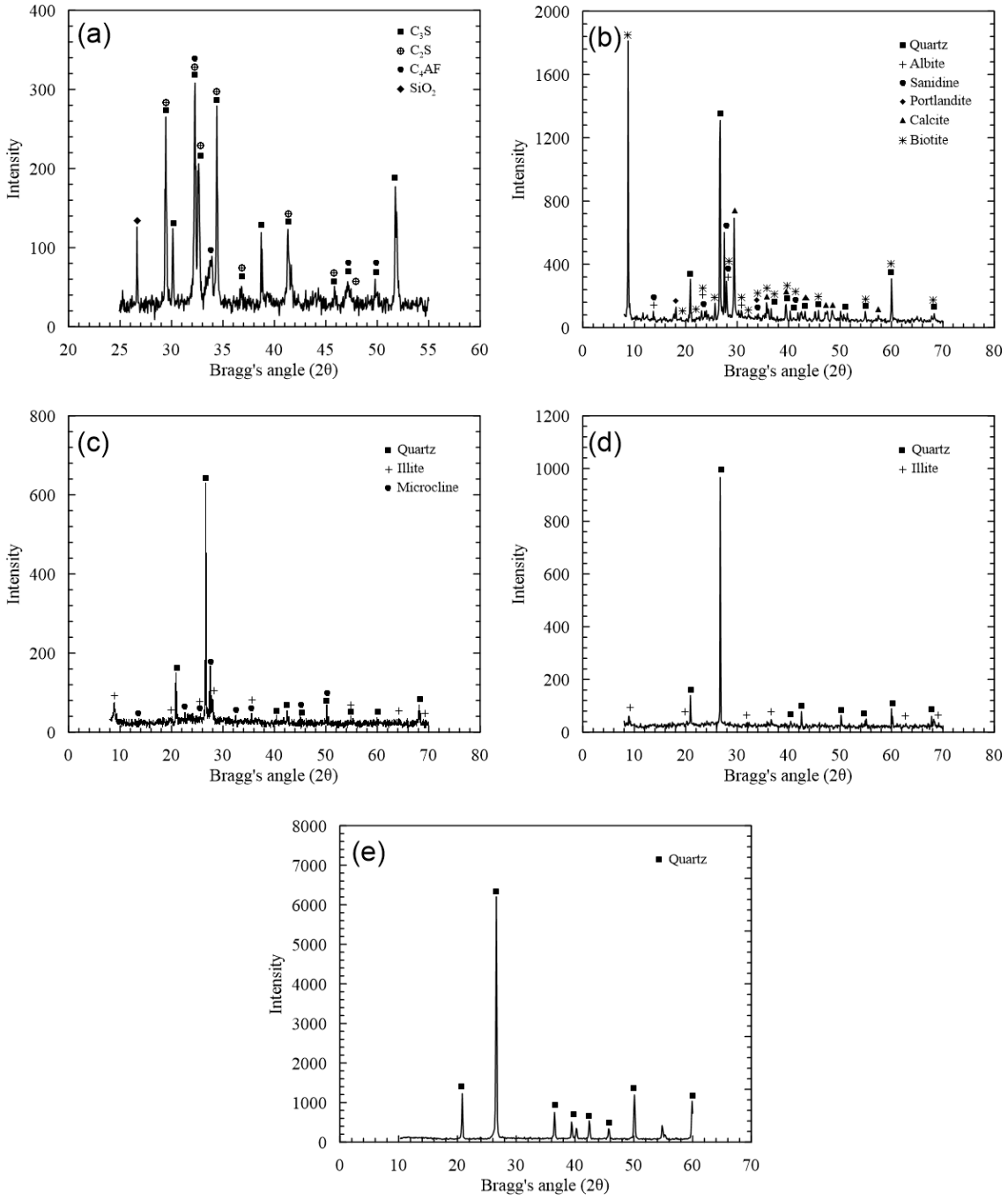

Figure 3.2: X-ray diffraction pattern of the materials. Portland cement (a), recycled concrete (b), face brick (c), hollow brick (d), and quartz (e).

tributed in comparison to each other and, particularly, to compare them with the cement particles. The particle size distribution of cement and supplementary cementitious materials were realized using a laser diffraction particle analyzer (Malvern Mastersizer 2000) with lens 100 (0.5 – 180 μm) in liquid mode[9] and ultrasonic agitation for 60 seconds. Concluding the powders characterization, Figure 3.4 shows the

[9]With analytical-grade ethyl alcohol as dispersant for the cement, and deonized water for the supplementary cementitious materials

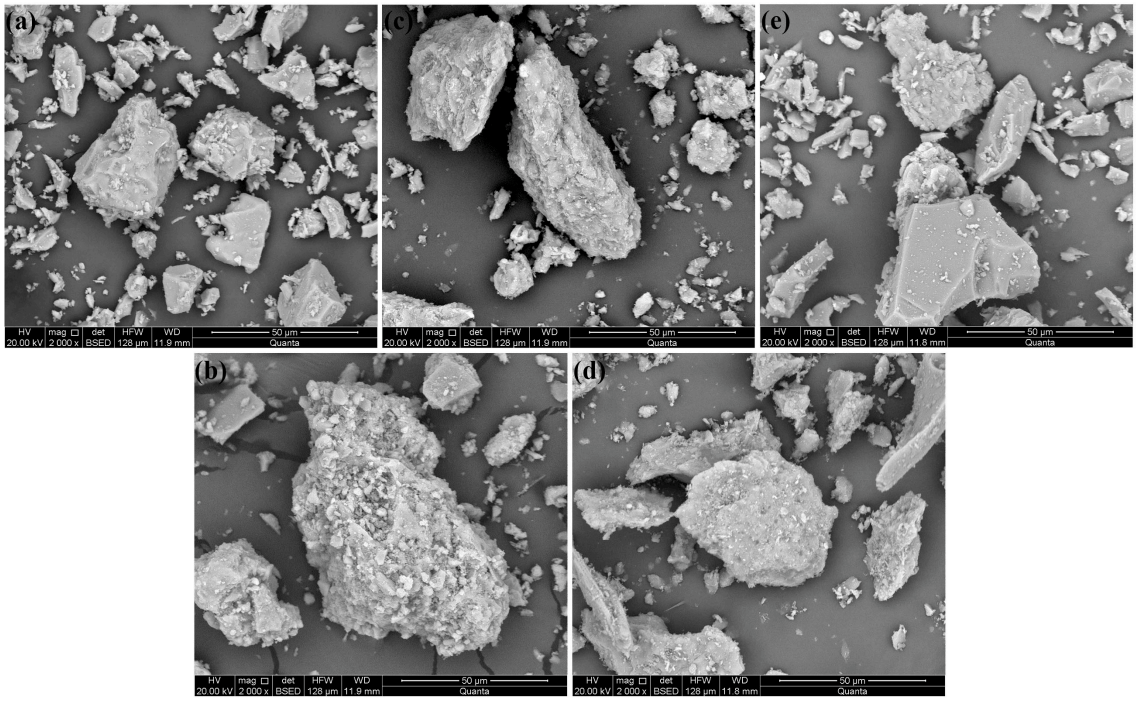

Figure 3.3: SEM images of the materials: cement (a), recycled concrete (b), face (c) and hollow (d) bricks, and quartz particles (e). Magnification of 2000x.

particle size distribution of the materials. Overall, the same crushing and sieving procedures generates similar fraction sizes of SCM, which contributes to evaluate their effects - independently of their singular sizes - when include into cement systems. In particular, Table 3.2 displays that their median size d are about 15-25 μm (47.5 - 59 %) larger than the cement particles.

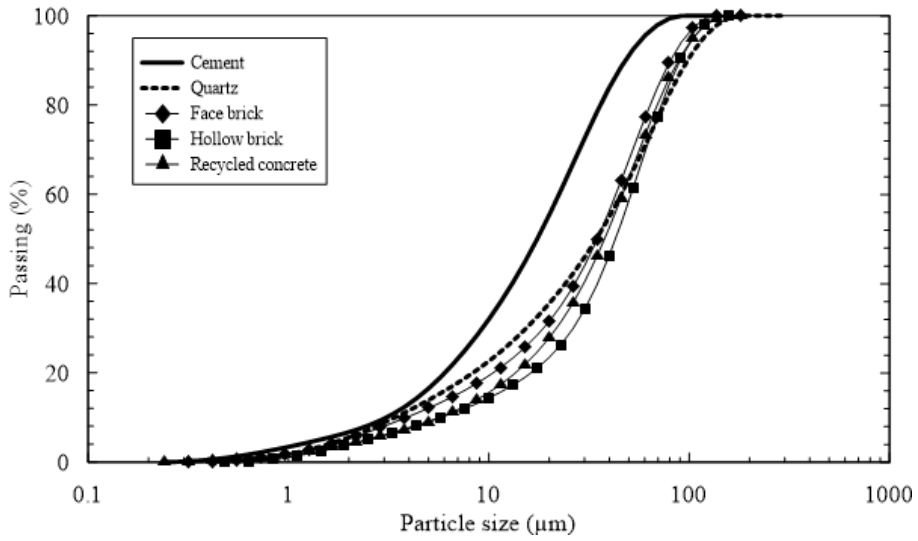

Figure 3.4: Particle size distribution of cement and the supplementary cementitious materials.

3.1.3 Mix proportions and preparation of specimens

A reference paste without any addition was prepared with water-cement (w/c) ratio of 0.4. For the pastes with recycled or quartz powder a 10% substitution rate (in mass) of Portland cement was determined maintaining the water-cementitious materials (w/cm) ratio of 0.4. The cement pastes were produced in a planetary mixer (2 liters capacity) under lab-conditions with a controlled temperature of $21^oC \pm 1^oC$. The mixing process predicts that the powder materials pass through a homogenization process in an agate mortar before mixing with water in a low rotation velocity for 2 minutes. Then, a pause for 30 seconds followed by a 2 minutes final mixing in a high rotation velocity. Finally, the specimens were cast, sealed with a plastic wrap and maintained under saturated lime water for curing up to the test time.

3.1.4 Methods of characterization of the hydration-related properties of cement pastes

Isothermal conduction calorimetry

The study associated to the hydration phases of cement pastes was conducted using a isothermal conduction calorimetry. The calorimeter measure the heat flow related to the hydration reactions taking place in the cement paste after the mixing procedure.

The hydration process of cement materials and the development of its microstructure are associated to the released heat flow and according to Taylor [26] is convenient to consider the whole process by the following stages: (i) the initial reactions period, described by the initial peak (1) attributable to an exothermic wetting and the early stage reaction; (ii) inductions period, related to minimal hydration rates after the premature reaction of the initial period; (iii) accelerating period, characterized by the main peak (2) when the middle stage reactions occur, in which the main products are C-S-H and CH; (iv) the decelerating period, that begins when the main peak (2) starts to decrease and a more definite peak (3) occur at about 16h, representing the renewed ettringite formation, which could take its amplitude influenced by pozzolanic reactions and; (v) the slow reactions period (see Fig. 3.5).

The rates of heat evolution of the cement pastes were measured by an isothermal conduction calorimeter (TAM-Air-314, an 8-channel heat flow calorimeter from TA Instruments) with 60 mW measuring range, and glass ampules filled with 2.5g of deonized water as reference. The mixing process was realized with a glass stick for about 1 minute outside the equipment. Then, glass ampules were utilized to put the fresh samples into the calorimeter in less than 300 seconds after the very first contact of cement with water. All samples were tested up to about 240 hours (10 days) at 23°C. The glass ampules were handled with insulating gloves, ensuring small

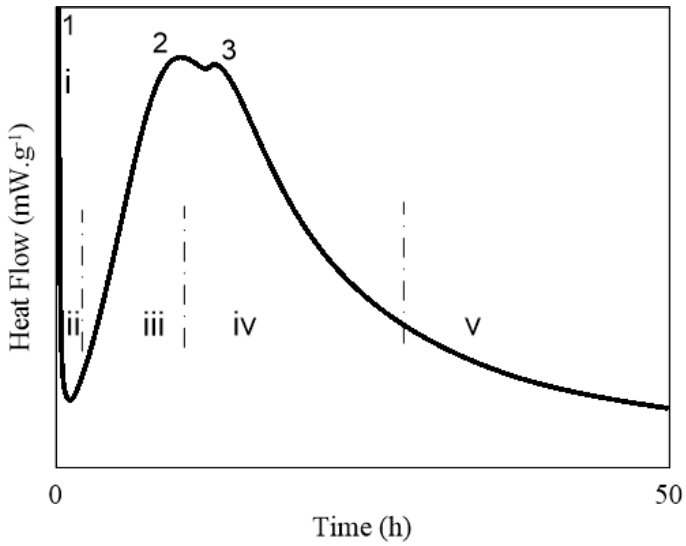

Figure 3.5: Rate of heat flow evolution for a typical Portland cement pastes determined by isothermal conduction calorimetry.

external temperature disturbances of the samples. The weight of the cement pastes measurements was about 5 g. The cumulative heat of hydration was calculated by integrating the measured rate of heat flow evolution.

Uniaxial compression test

Uniaxial compressive strength experiments were performed to investigate the strength evolution of the pastes with time and, at 28 days, the stress-strain behavior in compression was evaluated as well as its fracture properties. The latter will be later discussed in the next chapter and its analysis follows the methodology developed in chapter 2.

The uniaxial compressive strength tests of cement pastes were conducted using cylindrical specimens of 25 mm diameter and 50 mm height. The pastes were evaluated after 1, 7, 14, 28 and 91 days of curing with 4 samples for each age-mixture. The tests were carried out in a Wilkeham Ferrance universal test machine with displacement rate at 0.1 mm/min. At 28 days, the stress-strain behavior was also obtained by using two diametrically opposed extensometers fixed to the central region of the specimens to measure the longitudinal and transversal displacements (Figure 3.20). The Poisson's ration and Young's modulus (E_c) were calculated considering linearity of the stress-strain curve for stresses in the range of $50.10^{-6}E_c$ to $0.4\ f_c$[10].

Compressive strength test results were validated by statistical testing using analysis of variance (ANOVA) and Duncan's Multiple Range Tests [126], if necessary[11]. Significant differences were considered when the probability ≤ 0.05. All results are

[10]Where f_c is the compressive strength.

[11]In other words, the Duncan's test is performed when the ANOVA finds significant differences.

expressed as average of 4 specimens (± standard deviation).

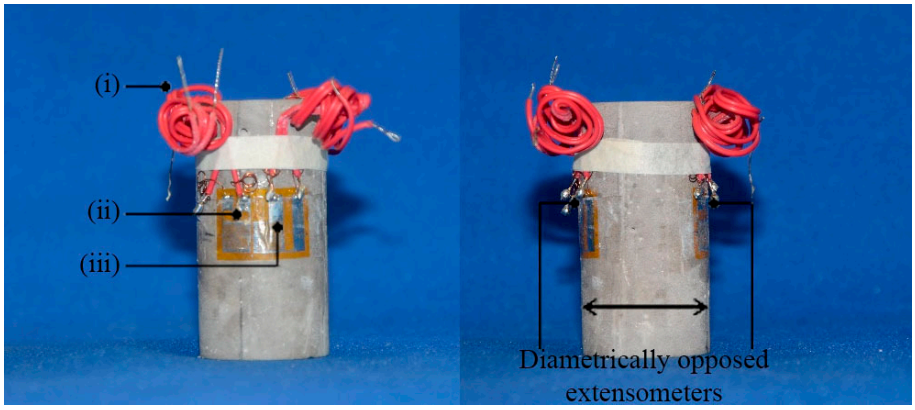

Figure 3.6: Cylindrical samples setup for the 28 days compressive strength experiments: (i) wire connection to the data acquisition system, (ii) extensometer for longitudinal displacements measurement and, (iii) extensometers to measure the transversal displacements (a); Setup positioning of extensometers (on right).

Mercury intrusion porosimetry

The hydrated cement paste have its physical and mechanical properties affected by the porosity. The porosity is classified according the pore size distribution and related to some material properties as following [26, 127]:

- Large capillary pores and air content: pore diameter $>$ 1000 nm, which directly affect the mechanical strength of the material;
- Large capillary pores: 50 nm $<$ pore diameter $<$ 1000 nm, affecting the mechanical strength and permeability;
- Medium capillary pores: 10 nm $<$ pore diameter $<$ 50 nm, which have influence on the mechanical strength, permeability, creep, and shrinkage over high relative humidity conditions;
- Gel pores: diameter $<$ 10 nm, affects the creep and shrinkage behavior.

Mercury (Hg) intrusion porosimetry is one of the most applied techniques to quantitatively describes the pore distribution of a solid. This method bases itself on the concept that a liquid with high surface energy (in comparison to the solid) will only penetrate the material under pressure. In this particular case, the pore size distribution is obtained by the volume of Hg that penetrates the samples in a certain pressure. For Hg, the surface energy y is 0.483 Nm^{-1} and the contact angle θ is between 117^o and 140^o. The maximum pressure applied is typically 400 MPa, which allows pores of nominal diameter down to about 3.5 nm to be intruded [26].

Pore size distribution and porosity of all cement pastes were investigated within mercury porosimetry. Measurements were realized according ISO 15901-1 [128] (equipament AutoPore IV - Micrometrics) at the *Laboratório de Caracterização Tecnológica* of the *Universidade de São Paulo* by Prof. Carina Ulsen and co-workers. The volume of mercury intruded in the sample is function of the applied hydro-static pressure, which is related to the pore diameter D_p by the Washburn [129] equation

$$D_p = \frac{-4y\cos(\theta)}{P} \tag{3.1}$$

where y is the surface energy of the liquid, θ is the contact angle, and P is the applied pressure. Samples of about 1000 mm^3 were extracted from the central region of cylindrical specimens (25 mm of diameter and 50 mm height) of cement pastes at 28 days of curing. The measures were realized considering $\theta = 130^o$ and maximum applied pressure of 275 MPa.

3.2 Effect of the powders inclusion on the properties of cement pastes

Hydration kinetics

Figure 3.7 presents the rate of heat flow normalized by the cement content[12] as function of time obtained by isothermal calorimetry. The initial peak - as (1) described in Fig. 3.5 - is attributed to the cement wetting and dissolution process during the first minutes of hydration as well as hydration of aluminate phases, *i.e.* formation of a gelatinous coating and rods of ettringite phase allied to a possible rehydration of hemihydrate to give gypsum [26]. A brief word may be added concerning potential complications to the measurements of this peak due to the outside mixing procedure. Therefore, the first period that we evaluate is the one of induction though, where the three pastes with recycled powders display slightly higher rate of heat generation than both the reference and the paste with quartz as well as a shorter duration of this early slow reaction period.

In the neat of the reference and quartz pastes the acceleration period starts after 3.5 hours. In general, the 10% substitution rate of Portland cement by an inert quartz keeps the slope of the heat flow-time curve nearly all the acceleration period, *i.e.* any significant effect on the early hydration kinetics have been observed. Nevertheless, the two following maximum heat flow peaks - (2) and (3) described in Fig. 3.5 - reach, respectively, 3.01 and 2.86 mW/g at about 10 and 13 hours of

[12]In figures 3.7 and 3.8 the unit in y axis defines the normalization of heat (flow or evolved) by cement content as g_{cement}, however, in the sequence of the manuscript, whenever it is written the unit mW/g it reads g as gram of cement as well.

hydration for the reference, while for the quartz paste both peaks reach heat flow values of about 0.1 mW/g higher at the same time of the reference ones. This behavior is expected since we have now a dilution effect provided by the cement replacement, *i.e.* a higher effective w/c ratio.

Let us highlight the case of the paste with concrete waste, in which the acceleration period starts about half an hour earlier than the reference paste at the same rate of heat flow (0.94 mW/g) with the slope of the curve slightly less steeper up to 4 h of hydration (see the bottom inset in Fig. 3.7). From this point on it displays similar trend as the reference paste until reach the same maximum heat flow peak of 3.01 mW/g (top inset in Fig. 3.7). Thus, in this particular case the dilution effect is less pronounced due to an indefinite change in slope and a lack of enhancement of the main hydration rate peak.

In the case of pastes with both ceramic materials, the maximum hydration rate increases whereas the time to reach this main rate peak decreases. The time to reach the maximum hydration rate peak decreases in about 20 minutes. Also, the degree of reaction of the Portland cement component during the main hydration peak is enhanced in about 5%, mostly by the dilution effect provided by the substitution of cement. Nevertheless, the cement replacement by face and hollow brick wastes suggests that these powders - even at larger particle size - could provide extra nucleation sites for C-S-H [].

In addition, the results of the three pastes with recycled powders display an accentuated peak (3) - the one that represents the formation of renewed ettringite - in comparison to both the reference and quartz paste (see top inset in Fig. 3.7). This fact could be explained by the quantity of aluminium oxide [26] presented in these recycled materials, especially by the ceramic ones (see Table 3.2).

Figure 3.8 shows the released heat normalized to the amount of Portland cement starting from 30 minutes of hydration. The cement paste with quartz starts to release more heat compared to the reference paste after 12 hours of hydration, which is mostly related to the dilution effect in the paste promoted by the new higher w/c ratio. In the case of pastes with recycled concrete, it starts to release more heat than the reference one about 6 hours earlier due to a shorter and less pronounced induction period. This effect is also observed in the pastes with recycled ceramics, although their curves start to display an expressive increasing in the released heat within time. Therefore, indicating that, despite the dilution effect, the ceramic powders should provide changes in the hydration properties of the pastes, *e.g.* some pozzolanic reaction [67, 72].

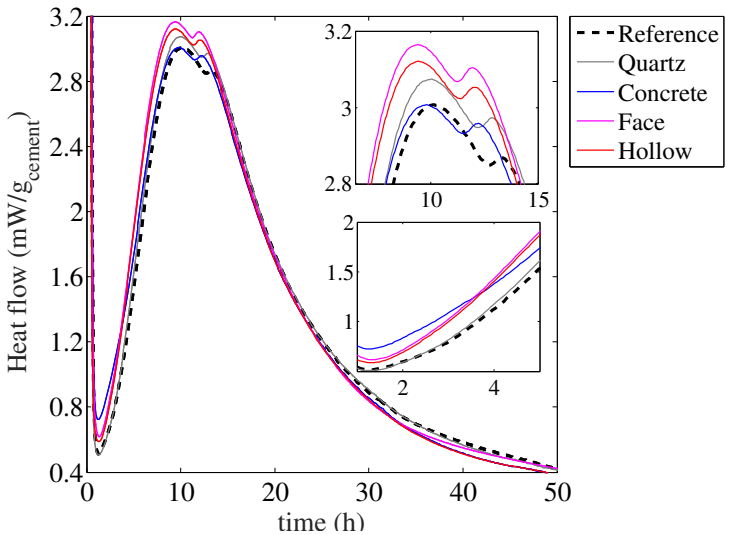

Figure 3.7: Effect of the different powders inclusion on the hydration kinetics of Portland cement paste. Bottom inset shows in detail the transition from the induction to the acceleration period, and the top inset displays a zoom at the main peaks (2) and (3). The main panel display the whole heat flow up evolution to 50 hours.

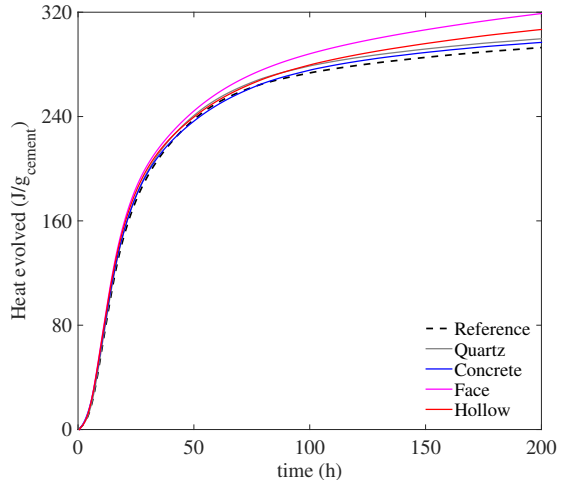

Figure 3.8: Effect of the different powders inclusion on the released heat normalized by the amount of Portland cement at 23^{o}C up to 7 days.

Compressive strength evolution in time

In the following, the compressive strength evolution with time is investigated to understand how the recycled inclusions affect the strength of the material. Table 3.3 and Figure 3.9 shows the average compressive strength results with standard deviation. A 10 % Portland cement's replacement by quartz - an inert inclusion - clearly reduces the compressive strength independently of the curing time due to less cement content.At 1 and 7 days of curing the effects of quartz inclusion are remarkably high, when f_c is about 35 % lower than reference paste. Since we have now less cement content, this is expected due to the intensive reactions at the early

hydration period [26, 127, 130] of Portland cement blends.

When substituting 10% of cement by recycled concrete powder, the compressive strength decreases due to none (or low) reactivity of this component. According to analysis of variance the strength results of the reference were higher than the recycled concrete paste in all ages studied. Let us now evaluate its result after 90 days of hydration; when the compressive strength increases from around 63 MPa at 28 days to 76 MPa. Thus, considering that the recycled concrete and quartz pastes behaves similarly up to 28 days (see Fig. 3.9), when comparing these ages, we observe that while quartz paste presents a strength evolution rate in time from around 1.4 %, the concrete paste's strength increases about 17%, which is even higher than the trend presented by the reference paste (around 11 %). Thus, leading us to guess about possible reactivity of non-hydrated cement grains presented in the recycled concrete powder (see for example Refs. [63, 131]).

Table 3.3: Compressive strength evolution with time of cement pastes (standard deviation values indicated within parenthesis).

Mixtures	Compressive strength (MPa)				
	1 day	7 days	14 days	28 days	90 days
Reference	11.97 (± 1.54)	49.70 (± 2.70)	53.28 (± 7.83)	72.76 (± 2.92)	81.68 (± 1.39)
Quartz	7.75 (± 0.43)	33.01 (± 1.71)	45.34 (± 2.51)	59.53 (± 0.84)	60.35 (± 2.98)
Concrete	8.75 (± 0.45)	38.48 (± 0.37)	47.88 (± 0.53)	63.14 (± 1.58)	76.07 (± 0.26)
Face brick	9.01 (± 0.39)	35.74 (± 0.57)	48.35 (± 0.39)	69.85 (± 1.60)	80.59 (± 5.17)
Hollow brick	9.32 (± 1.23)	39.51 (± 0.96)	47.68 (± 1.55)	71.36 (± 2.17)	81.36 (± 7.42)

In the early ages, both mixtures with face and hollow brick wastes decrease the compressive strength due to the low reactivity of the material. Thus, according to the analysis of variance, the strength values of the reference paste were around 25% higher than these recycled ceramic pastes at 1, 7 and 14 days. Nevertheless, at 28 and 90 days a significant enhancement of the compressive strength compared to the paste with quartz is observed. They reach the same range of compressive strength results shown by the reference paste. This suggests the existence of pozzolanic activity by the fine powder from this red ceramic waste [67]. From this first analysis on the mechanical behavior of cement pastes, the recycled powders from demolished concrete and ceramic materials appear as a feasible option to partially replace Portland cement.

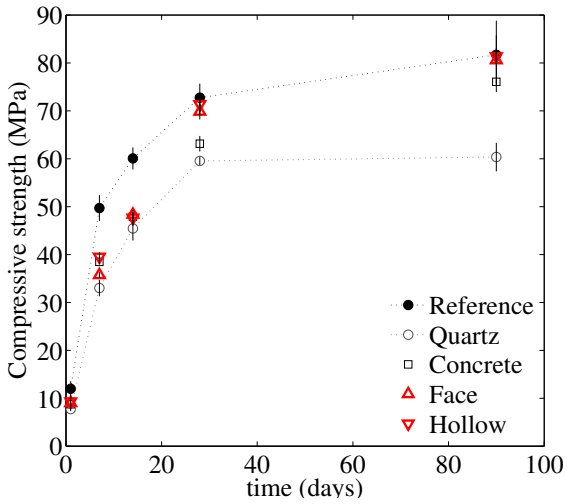

Figure 3.9: Compresive strength evolution of cement pastes. Pastes with recycled concrete and bricks are confronted to the reference paste and to paste with inert quartz.

Stress-strain behavior

Figure 3.10 displays typical stress-strain curves at 28 days of all pastes for axial and lateral displacements and Table 3.4 summarizes the average results of this stress-strain responses: strain at peak stress ε_c, Young's modulus E, and Poisson's ratio ν. In accordance to statistical analysis, no significant difference exists regarding the Poisson's ratio results of all samples. The Young's modulus result decreases in the order of 1.5 to 2.5 GPa when substituting Portland cement by quartz or recycled powders. Let us highlight the average result of the concrete waste paste that shows value 13 % smaller than the reference. However, no statistical difference exists between E results of all recycled and quartz pastes. Regarding the results of strain at peak stress, the substitution of Portland cement by quartz or concrete have no significant effect, although the inclusion of red ceramic waste increases the deformation capacity of the paste of about 30 %.

Overall, we observe that the compressive stress-strain response of paste with concrete waste behaves in a similar manner to the paste with quartz, while both pastes with red ceramic wastes shows the same behavior. These trends were also indicated in the previous discussions about hydration kinetics and the compressive strength evolution with time.

Pore size distribution

Figure 3.11 displays mercury pore size against the intruded volume of Hg curves at 28 days of all pastes. Table 3.4 summarizes the pore distribution according their size classification and the total porosity ϕ of all cement pastes. We observe that

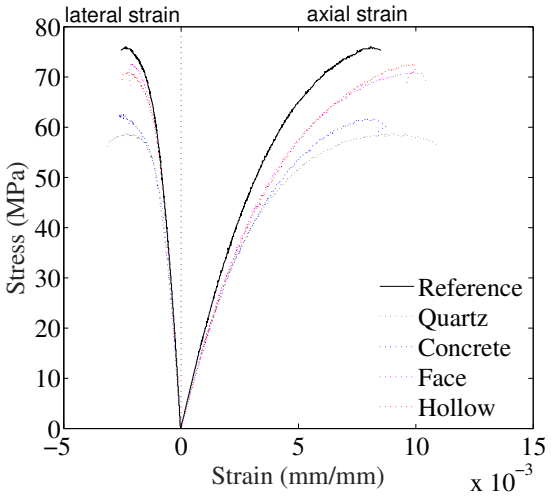

Figure 3.10: Compressive stress as function of axial and lateral strain of all cement pastes at 28 days.

Table 3.4: Mechanical characteristics of cylinder specimens tested in compression at 28 days for all cement pastes (standard deviation values indicated within parenthesis).

Mixtures	ε_c (mm/mm)	E (GPa)	ν
Reference	0.0076 ($\pm$ 0.0004)	17.5 ($\pm$ 1.07)	0.25 ($\pm$ 0.02)
Quartz	0.0074 ($\pm$ 0.0010)	15.4 ($\pm$ 0.86)	0.24 ($\pm$ 0.02)
Concrete	0.0082 ($\pm$ 0.0010)	15.2 ($\pm$ 0.39)	0.25 ($\pm$ 0.01)
Hollow brick	0.0096 ($\pm$ 0.0006)	15.9 ($\pm$ 0.48)	0.24 ($\pm$ 0.02)
Face brick	0.0100 ($\pm$ 0.0009)	15.7 ($\pm$ 0.48)	0.24 ($\pm$ 0.02)

even reducing the amount of gel pores in 24 %, the quartz paste provides a pore refinement in the capillary scale, *i.e.* it increases the amount of medium pores, while decreases the amount of the larger ones, in comparison to the reference paste. Let's also consider that the amount of large pores and air content (diameter >1 μm) increases about 80 % as well as the total porosity that goes from 21 to 25 %.

Looking at the porosity results of Table 3.5, it seems that the paste with concrete powders presents a larger porous structure than the reference one. Although, the pore size distribution of both reference and concrete pastes remains nearly the same (see Fig. 3.11).

The mercury porosimetry results of the pastes with both ceramic wastes display a small discrepancy between their total porosity results of about 2 %. Nevertheless, the pore size distribution reveals a similar mesh refinement of their porous structure in comparison to the reference paste; thus, the data presents an amount of gel and medium capillary pores around 25 and 30 % higher than the reference, respectively. This porous refinement at 28 days also contributes to the assumption of pozzolanic activity of these recycled ceramic powders.

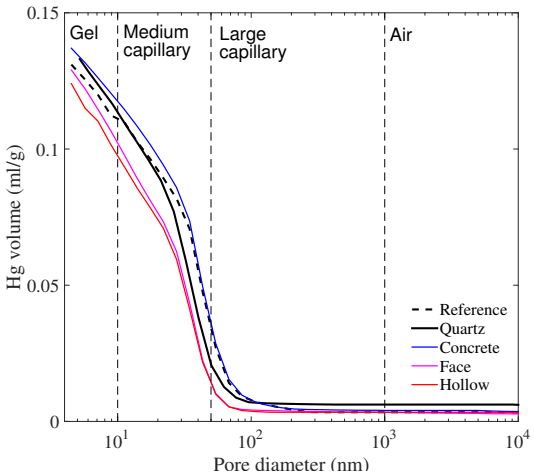

Figure 3.11: Mercury intrusion porosimetry experimental results for all cement pastes.

Table 3.5: Pore size classification from porosimetry results for the cement pastes - (gel) gel pores and hydrated phases; (M) medium capillary pores; (L) large capillary pores; (air) big capillary pores and air content; and (ϕ) the total porosity.

Mixtures	gel (%)	M (%)	L (%)	air (%)	ϕ (%)
Reference	14.2	49.5	33.7	2.6	21.0
Quartz	10.8	59.1	24.0	4.7	25.0
Concrete	12.1	51.8	33.1	3.0	22.3
Hollow brick	18.1	64.4	14.8	2.7	22.3
Face brick	17.4	65.3	14.7	2.6	19.4

3.3 Concluding remarks

In this chapter, the hydration-related properties of cement pastes with recycled or inert supplementary cementitious materials have been investigated. This study was motivated to characterize the main features of their microstructural development as well as their strength, though they can support the fracture investigation in the next chapter. A sequence of experimental techniques that allows to comprehend the hydration kinetics, strength development, and porosity have been studied systematically for plain cement pastes, and blends with inert quartz, recycled concrete or bricks from the red ceramic industry. Thus, the main conclusions of these experimental results can be summed as follows:

(i) The isothermal calorimetry results indicate an important dilution effect provided by the replacement of 10% of cement mass. This is the main reason that explain the differences found between the reference and the pastes with SCMs. More precisely, both concrete waste and quartz pastes were simply affected by this effect, which indicate low reactivity by the concrete powder. This was then contradicted by the late strength increasing rate observed for

the concrete paste from 28 to 90 days of curing. Nevertheless, this matter needs further investigation to asses properly this very late reaction ability. On the other hand, the pastes with both ceramic powders display evidences of pozzolanic activity, or more effective physical effects *e.g.* when rising the total heat released with time increasing.

(ii) The compressive strength evolution with time was observed to be highly affected by the cement substitution at the early ages (from 1 to 14 days). This is expected since the hydration reactions are intensified during this period [26]. At 28 and 90 days the effects of the pozzolanic activity of the ceramic [67, 70, 72] wastes enhanced the compressive strength of the pastes reaching the values of the reference paste. Although the compressive strength of the concrete waste paste has evolved similarly to the quartz paste, from 28 to 90 days it presented gains of 17%, which approximates to the trend showed by the pastes with ceramic powders.

(iii) The total porosity of the pastes at 28 days were around 20%. An exception was the paste with quartz that showed 25%. The reference and concrete pastes presented almost the same pore size distribution. Despite the total porosity has been similar to the reference, the refinement of the pore size distribution in the pastes with ceramic material confirmed the first evidences of pozzolanic activity of these SCM. It has been observed an expressive reduction (about 20%) of the large capillary pores, and consequently an increase in medium capillary and gel pores (about 25 and 4%, respectively).

This analysis have focused on the regular characterization of cement-based materials to set the scene about the type of material we are dealing. Overall, we addressed that the different particles slightly larger than cement may affect the cement blend by reducing their strength and increasing porosity such as in the quartz case; or refining the porous structure and mantainig the strength capacity as the ceramic based particles.

Finally, we investigate in the following chapter the fracture properties of these five cement pastes taking into account the complexity of the microstructural variations promoted by the different supplementary cementitious materials. To achieve such a characterization, we use the experimental methodology developed in chapter 2 to asses properly the toughness of the materials.

Chapter 4

Fracture Properties of cement pastes

During the last five decades, scientists have focused on understanding the fracture phenomena in cement based materials. Many attempts have been done using different theoretical frameworks yet large uncertainties remains even among results reported by researches using the same methodology [23]. Since the pioneering work of Kaplan [22], many effort have been done to experimentally characterize these materials using the principles of LEFM.

In the previous chapters, the validation of a fracture test methodology as well as a substantial characterization of blended cement pastes have been realized. In the first one, an extensive experimental campaign in PMMA specimens has provided a trustful method to identify fracture parameters such as crack length, crack velocity, fracture energy, and toughness in brittle failure.

The second one, showed how inert and reactive powders - different heterogeneities integrated into the material microstructure - affect the behavior of a cement paste regarding its hydration kinetics, porous structure, and compressive strength. The present chapter addresses the following questions: Does these SCMs at the microscale of the cement paste affect the macroscopic fracture properties? If yes, are these effects the same with inert and reactive materials?

We start by presenting the experimental setup and the modifications adopted to adapt the TDCB fracture test to cement pastes. Then, we will discuss the typical mechanical response of the plain hydrated cement paste (the reference material) and predict its fracture behavior using the methodology developed in chapter 2 for fracture property characterization - fracture experiments plus finite element simulation - based on the LEFM framework. At last, we investigate the effect of the presence of small inclusions in the cement paste composition on the toughness: we study first inert quartz inclusion that works as micro-aggregates, *i.e.* heterogeneity in the microscale of the material, followed by recycled inclusions of concrete and ceramic

wastes that may work as micro heterogeneity as well, although they have showed reactivity potentials when mixed in cement blends as presented in chapter 3.

4.1 Materials and methods

Preparation of TDCB specimens of hardened cement pastes

First, a steel mold were designed to cast the TDCB specimens of cement paste. It is totally detachable (see Fig. 4.1) so the sample can be safely demolded[1], and before its assembly, their internal surfaces and pins are coated with a chemical form-release agent. Once the mold is ready, it is filled with the fresh mixture that is cured in a 100% R.H. environment for two days. Then, after demolding, the specimens are set to curing up to the test age at 28 days (see the last chapter for detailed information about the mixing and curing procedures described in subsection 3.1.3). Let us highlight the notch's preparation: the base of the mold exhibits a pointed tip that provides a sharp ending, and before testing we use a razor blade prolongation to eliminate possible defects from demolding process and sharpen even more the initial notch. This strategy is similar to the one shown in Fig. 2.11 of chapter 2. At the end of this process, the initial crack length of the cement paste specimens is 36.5 mm.

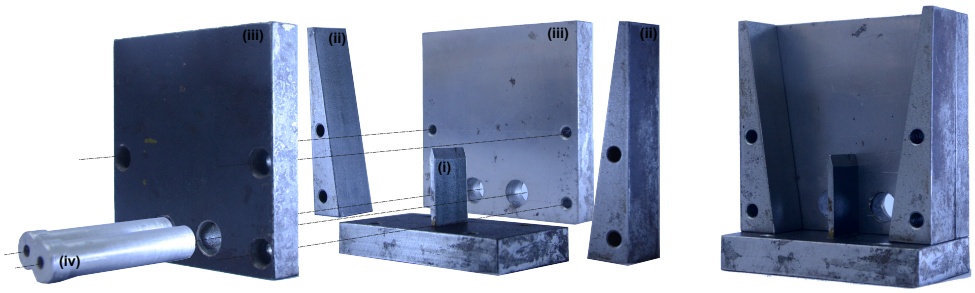

(a) **(b)**

Figure 4.1: Steel mold for cementitious TDCB specimen's preparation. In (a) an exploded view: where the dashed giding lines indicate the fixing screw points; (i) is the bottom base with pointing tip for notch's induction; (ii) the tapered sides; (iii) front and back sides; and (iv) two stainless steel pins for hole's preparation. (b) shows an inside view of the mold assembly.

A brief word may be added about the differences between the geometry used for

[1]The brittleness of cement paste materials turn the cast of peculiar geometries (like TDCB) in a difficult task. Therefore, before the final design of this steel mold, a few attempts to produce the TDCB specimens were realized extracting it from cubic samples of the hardened cement pastes with a stationary circular saw machine with diamond cutter, and a core drill machine. Among its problems were: (i) the difficult to obtain a sharp notch since the saw left a round ending of same thickness; (ii) drill the two holes, in which the force is applied, caused damage around the notch region, and often broke the specimen as well.

the cement pastes and the one used in PMMA samples presented in chapter 2. Here the grips of the machine that hold the sample and apply the force have larger pins, thus the holes in the specimens' geometry are larger too (diameter of 12.4 mm). As mentioned previously, this material is very brittle and cast beam samples of only 8 mm as in PMMA is quite unsafe, considering the demolding process and general handling operations prior to the experiment. Therefore, these samples are three times thicker (24 mm thick). One last difference is related to the fact that working with narrow and small sections is also unreliable, then we need to use two steel plates on the top of the lips of the crack (see Fig. 4.2) to connect the clip gauge device. Thus, as it is a manual operation, the distance between these plates changes for every single sample. Let us also highlight that these geometrical changes concerning the increasing in hole's size and the variations of Δ for each specimen tested have been implemented into the FE simulations used to interpret the experimental data.

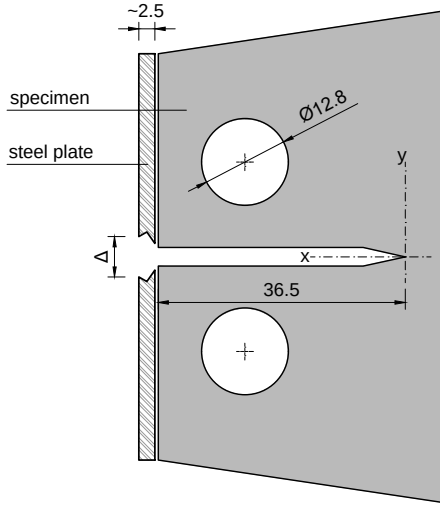

Figure 4.2: Geometrical changes designed for cement paste specimens (all dimensions in mm): Fixed initial crack length of 36.5, hole with larger diameter of 12.4, and the two steel plates for clip gauge connection. Attention must be paid for the variability of Δ due to manual fixing.

Experimental setup

Fracture tests on TDCB samples of cement pastes were carried out on 3 specimens of each of the five mixtures according the experimental procedure described in **??** at the Laboratory of structures and materials of COPPE at the Federal University of Rio de Janeiro. All the experiments were controlled by constant displacement of the machine stroke imposed at 0.01 mm/min.

Figure 4.3 displays the typical F-δ response of the reference paste. Crack initiates when the curve deviates from linear behavior at 96 % of the peak force (142.5 N)

and it propagates during the force decreasing regime up to displacements of 68 μm. Let us note the high levels of brittleness of this type of material, which presents a small 12 μm, so crack opening displacement about 1/6 of the total displacement, (see inset in Fig. 4.3) that is reminiscent of a rather low fracture energy.

Note also that we achieve a stable and well controlled crack growth regime, despite the high brittleness and stiffness of the material investigated. This stable regime is crucial to achieve a reliable determination of the toughness value.

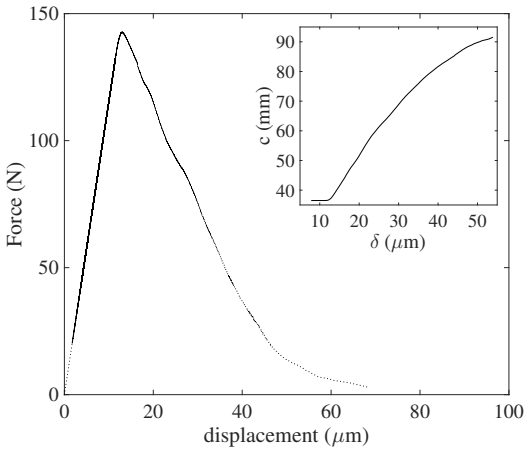

Figure 4.3: Typical experimental F-δ curve of the reference cement paste loaded at a displacement rate of machine crosshead of 0.01 mm/min. Top right inset displays the crack length evolution as function of COD.

Before presenting our results on the fracture properties of each paste, we would like a regular path. In other words, the crack deviates from the straight line initiated from the notch tip, and though leaves a particularly irregular and rough surface (see *e.g.* Fig. 4.4(b)). This observation questions the validity of our approach and our post-processing procedure: here, the fracture mode might be complex and some significant shearing (mode II and/or mode III) is also applied to the specimen in addition to the dominant mode I loading. This process leads to an increase of the fracture energy, as reflected by the tortuous fracture surfaces shown in Fig. 4.4(b). As a consequence, we disregard these tests in the following, and focus on samples submitted to pure mode I loading conditions.

The origin of this roughness might be twofold: a slight misalignment of the sample in the test machine might induce some spurious mode II or mode III shearing. But it also seems that this large scale roughness emerges from some large defects present in the cement structure, like entrapped air (bubbles). These flaws are common in cement based material, and we perform a cast procedure to eliminate large voids and achieve a rather homogeneous material composition. Despite this procedure, some samples contain defects of a few millimeters that significantly affect the

fracture toughness. These defects are a consequence of (bad) casting procedure during specimen preparation - mixing, curing, and demolding - *i.e.* manual work issues such as excessive use of the form-release agent, exudation or particle segregation in the fresh mixture stage during specimen assembly, needless effort when demolding, among others. In the following, only tests that show fracture path like the one of the example in Fig. 4.4(a) are used for the toughness determination.

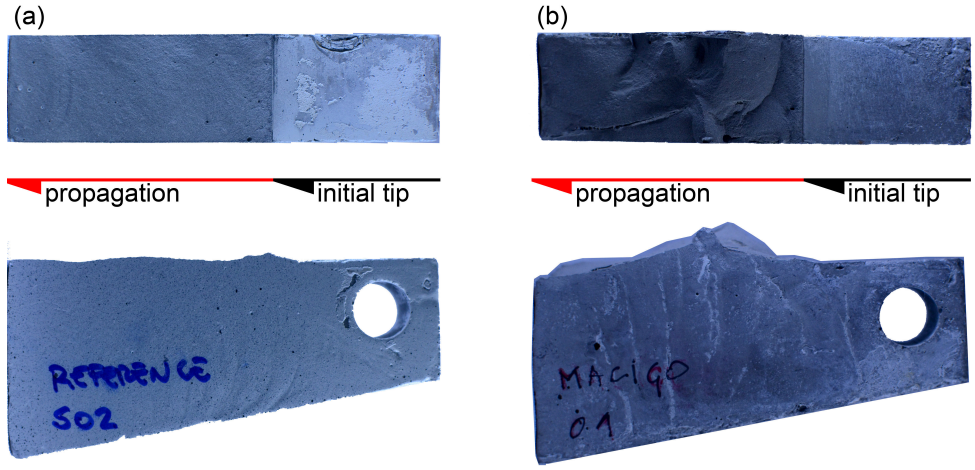

Figure 4.4: (a) A typical example of the rather straight crack path and surface of the cement pastes after fracture test in a TDCB specimen (a). (b) Irregular path chosen by the crack due to large defects presented in cement microstructure that lead to invalid experiments (b).

Table 4.1: Summary of TDCB fracture experiments on Portland cement pastes: (y) means that test are valid; and (-) represents the discarded ones.

Mixtures	specimen 1	specimen 2	specimen 3
Reference	-	y	y
Quartz	y	-	-
Concrete	y	y	y
Hollow brick	y	-	-
Face brick	-	y	-

4.2 Fracture behavior of hardened cement paste

The fracture parameters of crack length, crack velocity and fracture energy of the reference paste are presented in Figures 4.5(a)-(c). Let us first depict the crack propagation behavior observed from two valid test experiments[2]:

[2]One of the three samples was discarded according to the qualitative criterion of irregular crack path displayed in Fig. 4.4. For instance, as expected, this particular case presented an overestimation on G_c results.

(i) Starting with Fig. 4.5(a), we observe that crack keeps a rather constant velocity (of the order of 10^{-1} mm.s^{-1}) a few millimeters after initiation and over a rather broad range of crack length, typically 40 mm <c <70 mm. In the following, we use this range to measure the fracture toughness that corresponds to a stable and well controlled fracture process. At shorter crack length, *i.e.* less than a few millimeters from the notch, the crack front may be far from straightness, as crack initiation may take place somewhere along the initial notched, and not uniformly along it. A few millimeters are then needed for the crack to recover a straight front geometry, and for the fracture energy to reach a plateau. At larger crack length c > 70mm, *i.e.* beyond the range of validity of the exponential decay of the elastic energy release rate $G \sim \ \mathrm{e}^{-\mathrm{c}/\mathrm{c}_0}$ (see chapter 2) when the fracture process is less stable, we observe variations in the value of G_c from one sample to another (see Fig. 4.5). It seems that a less stable crack growth renders the toughness measurement less reliable, so we also disregard this large crack length regime.

(ii) From Fig. 4.5(b), the fracture energy is equal to 1.5 $\pm$ 0.5 J.m^{-2} in the range of interest 40 $\leq$ c $\leq$ 70 mm. This value is consistent with the results of the literature [23] [3]. The variations of G in the regime show more or less a plateau, that supports our choice to keep only values in the range 40 $\leq$ c $\leq$ 70 mm. Let us note that an increase in energy release rate with crack length (R-curve behavior) is unexpected for cement pastes, so we interpret the increase of the elastic energy release rate for short crack lengths as signature of the complex geometry of the crack front close to initiation that may not be straight, and not as an increase of the process zone size, as observed in materials like concrete showing a significant R-curve behavior.

Before we proceed to the comparison between the reference paste and each material inclusion, let us give a brief overview on the fracture energy measurements of cement paste. As previously mentioned, the area under the $F - \delta_F$ curve represents the total mechanical energy injected in the specimen during the test, and so provide a rough estimation of the fracture energy, named here as G_c^A. Then, from the curves of the selected specimens, we compare the experimentally measured values based on the compliance formula with these total area method in Table 4.2. Even though, we observe a small overestimation when using the value G_c^A obtained from the area under the force-displacement curve, the comparison shows a rather convincing agreement.

Note, however, that measuring only the area under the $F - \delta_F$ curve may lead to

[3] This value is also consistent with the estimated toughness determined from the total area under the $F - \delta_F$ curve.

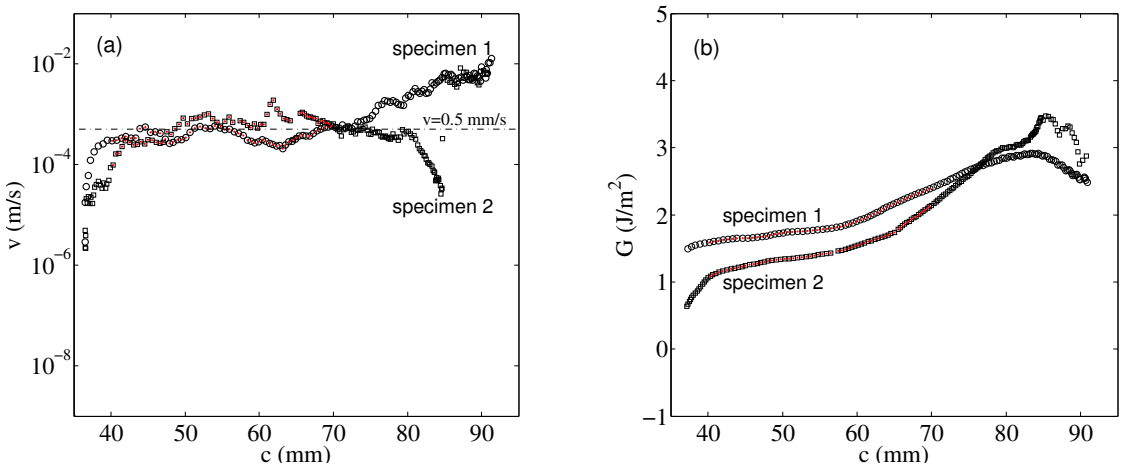

Figure 4.5: Fracture behavior of the reference paste. (a) Crack velocity as function of crack length, and (b) the variations of energy release rate with crack length.

Table 4.2: Fracture energy (G_c) experimentally measured on TDCB specimens with the compliance method, and the rough determination of the fracture energy (G_c^A) as the total work of fracture determined from the area under the experimental $F - \delta_F$ curve. G_c is computed as the average of G in the reliable range of crack length $40 \leq c \leq 70$ mm for the specimens presented in figures 4.8, 4.11 and 4.13.

	Reference	Quartz	Concrete	Hollow brick	Face brick
G_c (J.m^{-2})	1.8	4.1	2.8	2.8	2.7
G_c^A (J.m^{-2})	2.0	4.7	3.0	2.9	2.7

wrong estimate of the toughness in the general case. Here, we used the same TDCB geometry under the same loading rate $\dot{\delta}_F$ 0.01 mm/min for all the fracture tests. This ensures that crack speed is close to 0.5 mm/s for all the materials tested, as illustrated in Fig. 4.5(a) for the reference cement paste[4]. As a result, we compare here the toughness of all the materials at the same crack speed. It would have been interesting to investigate the variations of G_c with v_m for each materials. But as we focus here on the comparison between the fracture properties of materials with different composition, we keep v_m constant and explore the variations of G_c with the material composition only.

A word may be added here about the high complexity of the cement paste microstructure itself. From scanning electron microscope analysis of the polished surface of non-fractured samples, one can observes unhydrated cement particles as well as a dense matrix, but we also see voids that are like defects of different sizes. Let's take as example the Fig. 4.6 to illustrate how a large void (entrapped air >100 μm) in the microscale of the cement paste can be a source of flaws (microcracks). Indeed,

[4]We indeed measured a crack speed $v_m \simeq 0.5$ mm/s in all our tests. This is due to the fact that the proportionality factor between the crack speed v_m and loading rate $\dot{\delta}_F$ depends on the Young's modulus and the fracture energy G_c (see Eq. (**??**)) that do not vary much from one sample to another.

this mechanism should be present in all our samples, irrespective of the composition. In general we try to avoid large defects like this one, *i.e.* we expect that they are very rare, tough probably not affecting the toughness (except if the crack meets them, that is rather unlikely). Instead, they might control the strength of cement paste that is ruled by crack nucleation and so defects like this one.

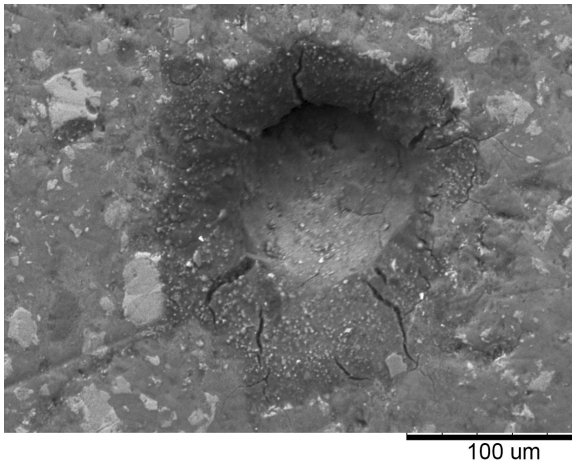

Figure 4.6: SEM micrograph of an void into the reference cement paste microstructure. It highlights to the very complex system with the unhydrated cement particles (in light gray), a dense matrix composed by hydration products (dark gray), and in particular, a large void of about 100 μm of diameter (highlighted in the center) nucleating several microcracks.

We now present our results on the fracture properties of cement paste containing different types of inclusions. The next section is devoted to the inclusion of quartz particles, the next one to the inclusion of recycled ones. In the end, a discussion section is devoted to the microscopic toughening mechanisms that may explain variations in the value of toughness from one type of cement paste to another. We also discuss how strength and toughness are correlated for these different materials.

4.3 Effects of inert quartz particles inclusion

In the previous section, the behavior of a plain cement paste has been described according the fracture methodology developed so far, *i.e.* from a fracture experiment in mode I plus a finite element solution for the TDCB geometry. Within the hypothesis of quasi-static crack propagation and the path chosen by the crack considered as reliable up to c $\approx$ 70 mm, the fracture energy of pure pastes is determined to $G_c \approx$ 1.5 J.m^{-2} (toughness $K_{Ic} \approx$ 0.2 MPa.m$^{1/2}$).

In this section, we characterize the fracture properties of Portland cement pastes when an inert particle with different properties is introduced even at small quantities (*e.g.* 10% wt.). Thus, the objectives here are: (i) to explore quantitatively the

particle effect on the fracture behavior; (ii) to discuss the physical origin of these properties.

The typical mechanical response ($F-\delta$ curve) of pastes with quartz is displayed in Fig. 4.7. It shows a rather different behavior, with a peak force about 100 N higher than the reference paste. Note also that the crack starts to propagate at the and of the linear elastic regime at displacement values close to 20 μm that is a bit larger that the reference. During the force decrease regime crack progresses up to displacements around 90 μm.

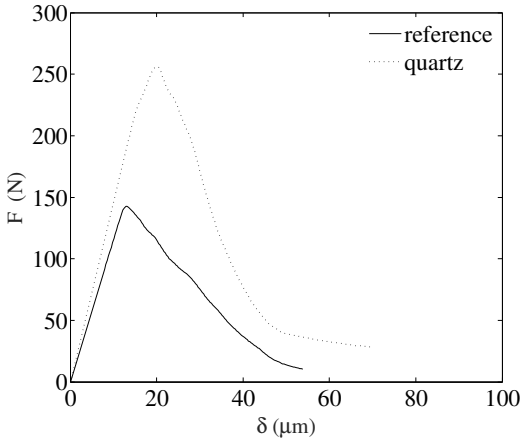

Figure 4.7: Typical F-δ curve of the cement pastes with quartz powder inclusion in comparison to the reference paste.

Figure 4.8 displays the variation of energy release rate with crack length. The addition of 10% of quartz particles substantially increases the fracture energy of cement pastes. An average value of G_c= 4.6 J/m^{-2}, considering the experimental data of the quartz paste, is more than two times greater than the average G_c of the reference mixture. Considering c $\leqslant$ 70 mm as the reliable range for the determinations of G results, the quartz paste reaches a plateau of around 4 J.m^{-2}.

When introducing a defect in a relatively homogeneous system it normally tends to become tough, thought the explanation to this increasing toughness possibly lies on two mechanisms: the quartz particle acting as a micro aggregate allows to nucleate microcracks due to low interfacial fracture energy between the quartz inclusions and the cementing matrix - at least lower than the unhydrated cement grain or CH crystal. Also the paste with quartz is possibly a way to arrest crack by attenuating the stress singularity. The quartz is, *in nature*, tougher than cement paste, its fracture energy is $G_c \simeq 70$ J.m^{-2} ($K_c \simeq 3.5$ MPa.m$^{1/2}$) [83], which ensure that the path chosen by the crack throughout the cement matrix deviates around the stronger particle of quartz.

From one typical region of a polished surface sample of the quartz paste in

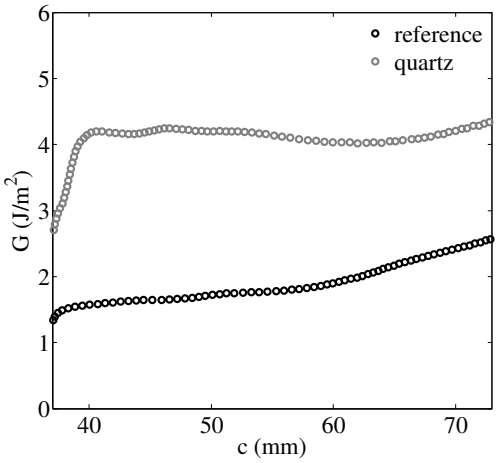

Figure 4.8: Effects of the Portland cement's substitution by quartz on the variations of energy release rate G with crack length c.

Fig. 4.9, one observes that although the Portland cement paste is itself porous (see, *e.g.* the porous structure topic addressed in section 3.2), the interface between the quartz grain and the cementing matrix presents less dense areas, with successive voids (dark black areas in the image). Thus, confirming the hypothesis that the inclusion of quartz particles is a strong source for nucleating flaws. In detail, Fig. 4.9(b) displays a zone of multiple microcracks surrounding one quartz grain, and also highlights a single microcrack (see the red arrows) that extends up to 120 μm from the neat interface zone and breaks into the matrix.

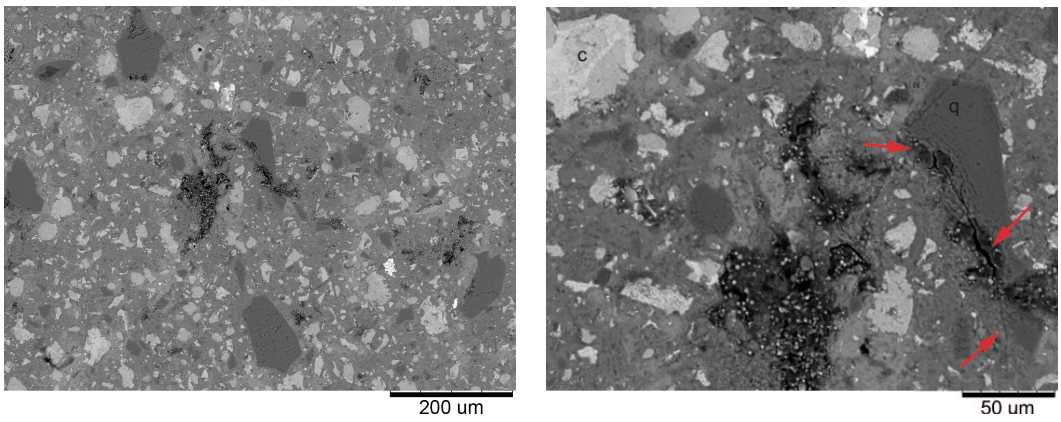

(a) (b)

Figure 4.9: Typical example of SEM image of the Portland cement paste with fine particles of quartz. Magnification of 200x (a) and 600x (b), image size of 1280 x 1040 px (8445 x 688 μm). Light gray areas are the unhydrated cement grains (c), dark gray regions are the quartz grains (q), dark (black) zones are voids, and the more homogeneous gray zone are the hydrated cement matrix. The red arrows point out a microcrack extending from the interface zone to the matrix.

4.4 Effects of recycled concrete particles inclusion

Figure 4.10 depicts the typical $F-\delta$ response of paste with recycled concrete particles. In a direct comparison with the reference paste, the peak force increases from 142 N to 225 N, the corresponding crack opening displacements are almost the same (13 and 12.4 μm, respectively). At the end of the force decreasing regime, the COD reaches around 70 μm for both the reference and concrete paste. These data also highlights some differences in the slope of the linear elastic regime, *i.e.* the Young's modulus E, that will be further discussed in this chapter.

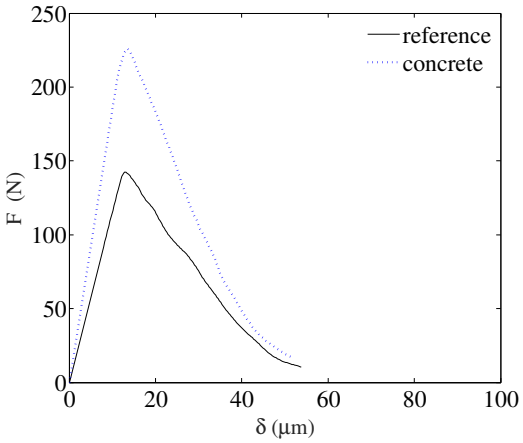

Figure 4.10: Typical F-δ curve of the cement pastes with concrete waste powders in comparison with the cement paste with no inclusion.

The inclusion of fine concrete waste affects the fracture energy of Portland cement pastes. Indeed, an average $G_c = 3$ J.m^{-2} indicates that these particles[5] work as micro aggregates[6] such as quartz particles do. Nevertheless, taking into account the range of fracture energy values given for concrete - 30-80 J.m^{-2} (see *e.g.* [9]) - we can explain why it is tougher than the reference, but weaker than the quartz paste. Let us take Figure 4.11 to depict a typical $G-c$ curve of concrete paste from crack initiation to 70 mm. After crack initiates, $G = G_c$, G values remains constant (around 2.5 J.m^{-2}) for $40 \leqslant$ c $\leqslant 60$ mm. Then, from 60 mm on, we observe a more pronounced increasing G with c, reaching 3.5 J.m^{-2} at c = 70 mm. As previously stated, R-curve behavior is unexpected for our experiments in cement pastes and this trend is attributed to some imperfections in the specimen, therefore, in this particular case we shall consider only results corresponding to c $\leqslant 60$ mm.

[5]Mainly composed by cement grains that have already hydrated

[6]Apparently, according to the isothermal calorimetry results presented in the last chapter, they are nonreactive when introduced in the cement paste mixture.

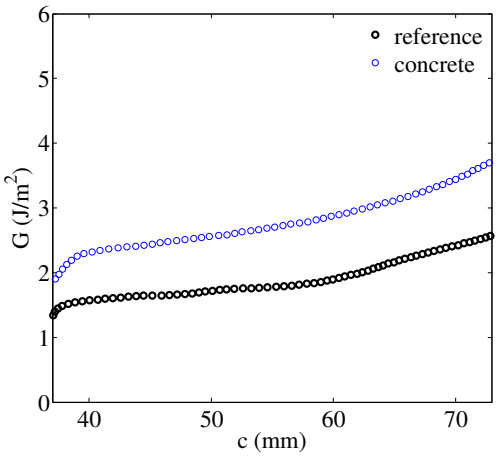

Figure 4.11: Effects of the Portland cement's substitution by recycled concrete waste on the variations of energy release rate G with crack length c.

4.5 Effects of recycled ceramic brick particles inclusion

Figure 4.12 displays the experimental response on fracture tests in TDCB specimens of the cement pastes with red ceramic brick wastes (both face and hollow) in comparison with the reference. It is worth mentioning that for each set of three experiments on pastes with recycled brick, only one sample reported acceptable results according our criterion previously defined on section 4.1 (see Fig. 4.4 and Tab. 4.1). Now, let us start depicting the behavior of the cement paste with face brick. The slope of the linear elastic regime clearly declined[7] in comparison to the reference (and to all the other mixtures). Then, this curve starts to deviate from the linearity at about 90% of the peak force (158.5 N), when the crack begins to propagate. During the force decreasing regime, two small perturbations are observed around $\delta = 32$ and 36 μm, respectively. Indeed, they represent small defects on the cracked surface - air bubble of about ≤ 1 mm - however, the crack path remains straight up to 47 μm, when a large perturbation occurs and the crack finally change direction up to the complete failure. The inset in Fig. 4.12 correlates the crack opening displacements to their corresponding crack lengths and helps identify the position of each problem. This is easily confirmed by visual observations on the fracture surface.

The single valid test specimen of hollow brick paste presents a clearer response, and easier to interpret, *i.e.* the crack growth straight for a longer range of crack

[7]Even though we have discarded the two other tested specimens for the general analysis, it is worth noting that both of them presented similar slope during the linear elastic regime. Nevertheless, this decrease of Young's modulus is unexpected since we have valid data from compressive strength analysis in the previous chapter, but we will see that the fracture parameters results looks rather convincing.

lengths. Also, the linear elastic regime goes up to approximately 95% of the peak force ($\approx$ 210 N), with a slope, and so a Young's modulus, similar to the reference paste. During crack propagation, it progresses till displacements around 60 μm.

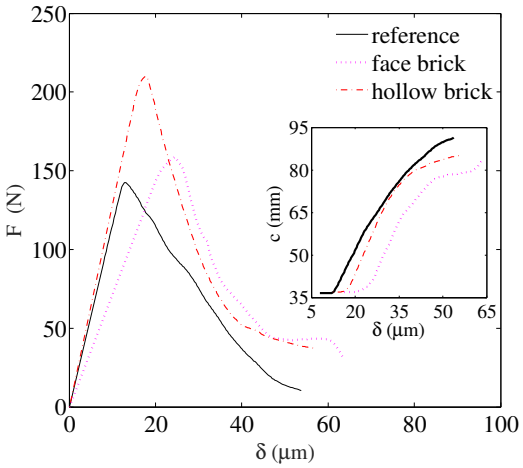

Figure 4.12: Typical $F-\delta$ curves of the cement pastes with red ceramic powder inclusions in comparison with the reference mixture. The right inset displays the variations of crack length with crack opening displacements δ for all three pastes.

Figure 4.13 shows the variations of energy release rate with crack length for the cement pastes with red ceramic waste. Comparing both face and hollow brick pastes results, one observes that the initial fracture energy $G^{\text{ini}} = G_c^{\text{ini}}$ values is nearly the same for both recycled brick pastes (around 3.1 J.m^{-2}). Furthermore, the respective crack length is around 39 mm for these experiments. Then, within the reliable range of crack lengths, G values oscillates between 3.2 and 2.4 J.m^{-2} for the face brick paste. It is worth noting that these oscillations arise from the small perturbations observed in the crack surface, previously addressed in the discussion of $F-\delta$ curve in Fig. 4.12. In the case of the hollow brick paste, one observes that G results progress more constant surround 3 J.m^{-2}.

4.6 Discussion

This experimental investigation of the cement pastes' properties have shown so far that as we add inclusions in the original matrix, we introduce weak interfaces. These interfaces are like defects that allow crack to nucleate even at early loading levels, which is deleterious for the mechanical strength. This is consistent with the observations made in chapter 3. On the other hand, this improves toughness, which can be mainly related to two reasons: (i) the crack deflects along the weak interfaces and, therefore, takes a longer way to propagate in the material, thus increasing fracture energy. Also, deflected cracks requires higher loading to propagate, as they grow

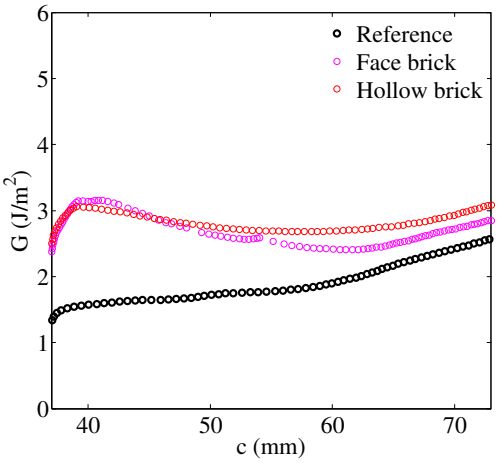

Figure 4.13: Effects of the Portland cement's substitution by recycled red ceramic bricks on the variations of energy release rate G with crack length c.

under mixed mode loading conditions that are more costly from a fracture energy point of view than pure mode I loading conditions; (ii) It induces more cracking in the material microstructure, that means when the main crack is nearby some additional microcracks may nucleate form the weak interfaces[8]. To assess correctly the reason of this mechanism, we have to estimate the fracture process zone size at the tip of the main crack. We discuss here further the physical origin of this toughening generated by the introduction of micro particles in the cement paste mixtures. This final section is devoted to the correlation between strength and toughness in a form of an Ashby diagram.

Fracture process zone size

Let us now explore the second scenario proposed in the previous section, namely that toughening may be induced by the presence of microcracks nucleating at the weak interface between inclusions and matrix. We can assess the extent of the zone in front of the main crack where microcracks may exist, *i.e.* the so-called process zone, from Eq. (1.17) reintroduced here as

$$l_{pz} = \frac{\pi}{8}\left(\frac{K_{Ic}}{\sigma_{tc}}\right)^2 \tag{4.1}$$

where σ_{tc} is the strength (the subscript t denotes that is tensile strength and the subscript c denotes critical).

Here, we assess toughness from the fracture energy experimentally measured in TDCB specimens with the compliance method using Irwin's relation $K_{Ic} = \sqrt{EG_{Ic}}$,

[8]The stress field generated by the main crack when it is passing throughout the material *activates* micro cracking [132].

for G_{Ic} computed as the average G in the range of reliable crack lengths defined previously as $40 \leq c \leq 70$ mm; and strength σ_{tc} from its relation with the compressive strength σ_c, since we have experimentally measured the compressive strength of the pastes in chapter 3. Here, we take the 28 days compression result (see Tab. 3.3) and assume the lower bound of the ratio $0.07 \leq \frac{\sigma_{tc}}{\sigma_c} \leq 0.11$ given in the technical literature of concrete material [127][9].

Using Eq. (4.1), we can estimate the size of the process zone. The corresponding values are listed in Table 4.3 for one broken sample of each cement paste type. They are all at least 1 order of magnitude higher than the largest particle size inside the system. This picture attests that microcrack nucleation governs the failure mechanism of cement pastes overall [18, 23, 26, 27]. The reference paste shows the smallest process zone size in comparison to all other mixtures. This is related to the particle diameter within the matrix. Only unhydrated cement particles of about 17μm are present in this case. In addition, despite the intrinsic heterogeneous nature of Portland cement pastes, as this reference composition is the more homogeneous case among our five mixtures, it leads to the lowest results of toughness, and the highest strength. Therefore, it is possible to confirm that its microstructure is less affected by weak interfaces[10]

Since the differences between the median particle diameters (d) are less than 10μm among the four inclusion types, we shall consider them equal in respect to their size when comparing to the Portland cement, and consequently asses their influences on the pastes' behavior neglecting these small variations. For example, even though we might relate the increase in l_{pz} to the addition of large particles (inert and recycled ones) that can work as micro aggregates, when comparing the results of the cement pastes with the inclusion of the four different particles with the reference, one observes that their process zone sizes increase at different levels, and that is independent to the small differences between the size of each particle. As depicted in Table 4.3, the smallest process zone size is the one with respect to the pastes with red ceramic waste, followed by the mixtures with concrete, and then

[9]It is worth noting that several empirical formulae connecting both tensile and compressive strength have been suggested for concrete [130], many of them of the following type $\sigma_{tc} = k(\sigma_c)^n$, where k and n are coefficients. A few correlations are found between the measures of splitting tensile strength and the square root of the compressive strength. Values of $1/2 \leq n \leq 3/4$ have been suggested by the American Concrete Institute [133], or for example Ref. [134]. However, as this work deals specifically with cement pastes and no relation has been defined for it yet, we assume the lower bound of 7% of σ_c defined above that is also among the possible results suggested in Refs. [133, 134]

[10]As addressed previously in section 1.2, simple hardened Portland cement systems (*i.e.* Portland cement plus water only) has as its main source of defects the interface between unhydrated cement particles and their hydration products. For instance, at 28 days, the crystals of calcium hydroxide often cover the majority of the paste area, and (micro)cracks will occur through the CH rich and C-S-H phases. It is worth noting that as the pastes reach maturity, it becomes more homogeneous and less porous though the fracture path might becomes more direct as well [23].

with quartz.

In particular, we can observe that the substitution of 10% of cement by quartz provides l_{pz} (estimated using Eq. (4.1)) three times larger than the process zone of the reference paste. This allows us to confirm that the size of the process zone plays a crucial role in the fracture toughness of the material. Since the larger the l_{pz}, the more toughening events are able to take place, the higher the K_{Ic} [], one would directly explain why the toughness value of the cement paste with quartz is the highest among all mixtures. Let us come back to the example of Fig. 4.9, where it highlights a more damaging zone in the neat interface between the quartz particle and the matrix. In other words, multiple microcracks are observed, and their presence implies that these weak interfaces may act as stress concentrators, inducing to more (micro)cracking upon the loading sample, and consequently increase the size of l_{pz}.

Table 4.3: Parameters for calculating process zone size (l_{pz}) according Eq. (4.1): (K_{Ic}) Toughness; (σ_t) estimated splitting tensile stress (lower bound). We also highlight here the median size (d) of the particles of cement (common to all mixtures, displayed in the line corresponding to the Reference) and the inclusions in respect to each corresponding mixture.

Mixtures	K_{Ic} (MPa.m$^{1/2}$)	σ_t (MPa)	l_{pz} (μm)	d (μm)
Reference	0.18 ($\pm$0.010)	5.1 ($\pm$0.20)	480	17.45
Quartz	0.25 ($\pm$0.002)	4.1 ($\pm$0.06)	1440	33.24
Concrete	0.21 ($\pm$0.009)	4.4 ($\pm$0.11)	865	37.77
Hollow brick	0.21 ($\pm$0.004)	5.0 ($\pm$0.15)	700	42.82
Face brick	0.20 ($\pm$0.009)	4.9 ($\pm$0.12)	685	34.83

As previously discussed, the concrete waste particles behaves similarly to the quartz particles, acting as a micro aggregate, since it has none or very low ability to react again within the Portland cement system. Nevertheless, the size of the process zone in the cement pastes with concrete is smaller than the quartz paste, as well its toughness though indicating that the interface between the matrix and waste particle might be stronger than with quartz.

Once again the pastes with both types of red ceramic particles presents similar results. Their process zone sizes are considered the same (differences of 15 μm, smaller than the median particle diameter). In this case, we can directly attribute the smaller effect on the l_{pz} - in comparison to the reference - to the suggested pozzolanic activity of these materials. This leads to a pore refinement in the microstructure of the pastes as well as gain in strength in the mature paste (see the discussion in section 3.2). Let us note here the consequence of it, that is both the strength and toughness are less affected by the ceramic particle inclusions.

Overall, the previous analysis based on the process zone size suggests that mul-

tiple microcracks exists in the cement matrix, and that is expected in cement based materials as demonstrated by the size of the process zone[11] $l_{pz} > d$ of the cement particle. Furthermore, when introducing micro particles from different sources they naturally induces the creation of new interfaces within the Portland cement matrix. Our work demonstrates the key role played by weak interfaces in the fracture properties of the pastes. To conclude we now explore the correlation between the fracture energy measured experimentally and the splitting tensile strength determined theoretically.

Mechanical properties correlation

As weak interfaces promote microcrack nucleation, they may affect both the toughness and the strength of the cement pastes.

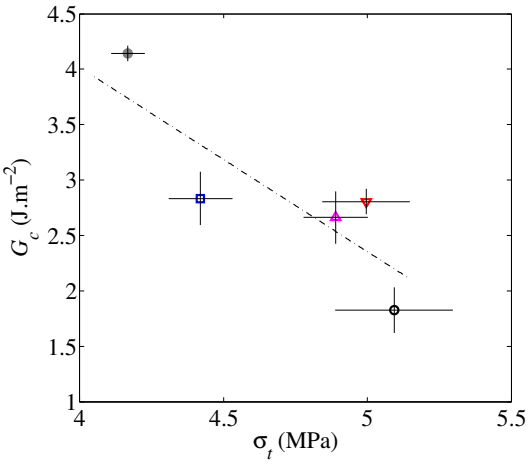

Figure 4.14: Correlation between the toughness and strength of the cement pastes (Plotted results correspond to data of Tab. 4.3). (○) Reference; Quartz paste (●); (□) Concrete paste; (△) Face brick paste; (▽) Hollow brick paste. The slope of the dashed line is 1.7.

The material properties chart (in the form of an Ashby diagram in Fig. 4.14) of the cement pastes illustrates that the strength and toughness are actually anti-correlated and that they may approximated by a linear function in the form of $G_c = \mathcal{L}.\sigma_t + G_c^I$, where $G_c^I = 1.7$ J.m^{-2} and $\mathcal{L} = 10.7$ μm are the parameters. As a general trend, we observe that the material strength decreases when increasing toughness. This seems consistent with what it observed in a large range of materials where, since toughness and strength optimization are usually incompatible [132]. Here, introducing weak interfaces in the paste microstructure by adding supplementary cementitious materials is detrimental to the strength as it promotes crack

[11] Of the reference cement paste.

nucleation but it beneficial to toughness as it increases dissipation within the process zone size at the crack tip. In addition, the more inert the particles, the larger are the both effects, that's why it is more pronounced for quartz than for concrete particles for example.

Conclusion

This study has investigated the fracture and hydration-related properties of particular cement-based materials produced with reactive or inert inclusion. In particular, we have focused on fine ground particles of recycled CDW and quartz as supplementary cementitious materials to investigate their effects on cement blends.

To achieve such a fracture characterization, a stable fracture is required in terms of trajectory and propagation of the crack. Therefore, we have first designed (and validated) a combined theoretical and experimental methodology for fracture test in mode I using a tapered double cantilever beam geometry to determine precisely the fracture toughness of the materials. The choice of a TDCB inspired geometry leads us to achieve a great stability of the whole fracture process, which is desired for highly brittle materials like cement-based ones. To validate the whole procedure, a model - easy to obtain and machine - PMMA material have been studied. First, we have confirmed the crack growth stability of the geometry trough a finite element study that showed for a certain range of crack lengths, far enough to the boundary, the compliance can be fitted by an exponential function. Then, a set of experimental TDCB fracture tests varying the external loading rate have been used to shown how the energy release rate increase with velocity. Their values - crack speed (within the range $10^{-5} - 10^{-3}$ m.s^{-1}) and fracture energies (from 200 - 600 J.m-2) - have provided the crack growth law, the so-called $G_c(v)$ kinetics of the material. We have then proposed a optimization strategy to reproduce the experimental measurements assuming a power law behavior of this $G_c(v)$ characteristics. This analysis have given optimum crack growth law parameters $G_{c0} = 1.98.10^3$ and $\gamma = 0.204$.

Moreover, from a direct correlation between the applied loading rate and the average crack growth velocity, we have provided a useful tool - see Eq. (2.12) - to target a particular crack velocity by selecting the appropriate external driving force.

The stability of our fracture test has also been emphasized by image-based determinations of the crack tip positioning - enabled by the transparent surface of PMMA samples - that showed good agreement to the crack length measurements based on the finite element solution of the TDCB geometry. Also, our FE based determinations of SIF and T-stress have agreed with the direct measures of an integrated digital image correlation (IDIC) algorithm, although some oscillations (around 3

MPa.m$^{1/2}$ for typical K_I results) have appeared in the mechanical response of the IDIC. Interestingly, IDIC has confirmed that the crack propagated along a straight path that satisfies $K_{II} = 0$. Overall, IDIC analysis have showed promising results for crack tip positioning and toughness, in our modified TDCB experiments.

The experimental characterization of the hydration-related properties of the cement pastes have demonstrated the viability of using recycled concrete and ceramic as supplementary cementitious materials. More precisely, calorimetry results have shown that the main mechanism affecting the early hydration of cement pastes is the dilution effect provided by the substitution of cement by SCM, although the ceramic materials have shown evidences of pozzolanic activity. Therefore, no deleterious effects have been added due to the introduction of these materials.

The mechanical properties in compression have been affected by the substitution of cement by SCM as follow: in comparison to a plain cement paste, from 1 to 14 days, the strength decreases for all other mixtures. The quartz and concrete paste maintained lower strength values for further ages of analysis, but at 90 days the paste with concrete surprisingly achieved average strength only 7% lower than the reference paste. Furthermore, the reactivity capacity of the ceramics has been confirmed by the strength gains at 28 and 90 days, when the mixtures showed compressive strength values similar to the plain cement paste. In general, when evaluating the stress-strain behavior, we have observed that 10% of cement mass replacement does not affect the Poisson's ratio, and that the Young's modulus slightly decreased around 2 GPa.

The pore structure of the pastes at 28 days of curing has been refined by the ceramic materials, though endorsing the findings on their mechanical response and calorimetry, *i.e.* attesting the hypothesis of pozzolanic activity. The concrete waste inclusion have not affected the microstructural porosity of cement pastes. Furthermore, the inclusion of quartz have increased the total porosity mainly increasing the quantity of medium capillary pores, which may indicate a weak bond behavior between the particle and the cement matrix in comparison to unhydrated cement particles.

Our study has been mainly devoted to the influence of small quantities of recycled and inert inclusions on the behavior of cement pastes. In general, the material toughness have increased when replacing 10% of cement mass by any other SCMs. This was more pronounced in the case of quartz substitution that showed the weakest interface with the cement matrix, and consequently presented the largest fracture process zone size. This was confirmed by SEM micrographs that displayed microcrack branching surrounding some particles of quartz. Also, this can possibly explain the higher total porosity of the quartz paste in comparison to the reference. The case of concrete waste as SCM have shown similarities with the behavior presented

by the quartz but, however, the toughness values, the porosity and the size of process zone were closer to the ceramic pastes. This was definitely affected by presence of old hydrated cement particles (confirmed by X-ray diffraction analysis) that despite being nonreactive like quartz, these results suggested a better bond behavior with the matrix. Even though, the recycled material have promoted toughening mechanisms as well, their effects were less pronounced due to the reactivity of the red ceramic materials that have led to a more homogeneous mixture, toughness and strength quantities similar to the reference, and a less expressive increase in the process zone size.

Finally, we have obtained a simple picture on the fracture properties of the cement pastes. Overall, we have confirmed the highly brittleness of the plain material that showed fracture energy $G \simeq 2$ J.m^{-2} smaller than glass [9] for an common ratio of w/c = 0.4. It have been found that the complex microstructure of cement systems - pores, hydration products, and unhydrated cement - is a natural source of (micro)cracks that might govern the failure of the material. And overall, a simple relation have confirmed that strength decreases with increasing toughness, which is useful when design materials.

Bibliography

[1] BENTUR, A., MINDESS, S. *Fibre Reinforced Cementitious Composites*. Taylor & Francis Group, 2007. ISBN: 10:0–415–25048–X.

[2] RODRIGUES, F. A., JOEKES, I. "Cement industry: sustainability, challenges and perspectives", *Environmental Chemistry Letters*, , n. 2, pp. 151–166, 2011.

[3] BARCELO, L., KLINE, J., WALENTA, G., et al. "Cement and carbon emissions", *Materials and Structures*, v. 47, n. 6, pp. 1055–1065, 2014.

[4] LAMPMAN, S. *Characterization and failure analyses of plastics*. Materials Park, Ohio, ASM International, 2003. ISBN: 0871707896.

[5] GRIFFITH, A. A. "The phenomena of rupture and flow in solids", *Phil. Trans. Roy. Soc. Lond.*, v. A221, pp. 163–198, 1920.

[6] INGLIS, C. E. "Stresses in a plate due to the presence of cracks and sharp corners", *Trans. Inst. Naval Arch.*, v. 55, pp. 219–239, 1913.

[7] SWAMY, R., KAMESWARA RAO, C. "Fracture mechanism in concrete systems under uniaxial loading", *Cement and Concrete Research*, v. 3, n. 4, pp. 413–427, 1973.

[8] MARDER, M., FINEBERG, J. "How Things Break", *Physics Today*, v. 49, n. 9, pp. 24, 1996.

[9] LAWN, B. *Fracture of brittle solids*. 2nd ed. Cambridge, Cambridge University Press, 1993. ISBN: 0 521 40176 3.

[10] RICE, J. "Thermodynamics of the quasi-static growth of Griffith cracks", *Journal of the Mechanics and Physics of Solids*, v. 26, n. 2, pp. 61–78, 1978.

[11] IRWIN, G. R. "Analysis of the stresses and strains near the end of a crack traversing a plate", *Journal of Applied Mechanics*, v. 24, pp. 361–364, 1957.

[12] SIH, G. C. *Handbook of stress intensity factors*. Institute of fracture and solid mechanics, 1974.

[13] FETT, T., MUNZ, D. *Stress intensity factors and weight functions*. Southampton, UK Boston, Mass. USA, Computational Mechanics Publications, 1997. ISBN: 1-85312-497-4.

[14] JOHNSON, J. A., JONES, D. W. "The mechanical properties of PMMA and its copolymers with ethyl methacrylate and butyl methacrylate", *Journal of Materials Science*, v. 29, n. 4, pp. 870–876, 1994.

[15] BARENBLATT, G. I. "The mathematical theory of equilibrium cracks in brittle fracture", *Adv. Appl. Mech.*, v. 7, pp. 55–129, 1962.

[16] RICE, J. "A path-independent integral and the approximate analysis of strain concentration by notches and cracks", *J. Appl. Mech.*, v. 35, pp. 379–386, 1968.

[17] LAWRENCE, F. V., YOUNG, J. F. "Studies on the hydration of tricalcium silicate pastes I. Scanning electron microscopic examination of microstructural features", *Cement and Concrete Research*, v. 3, n. 2, pp. 149–161, 1973.

[18] "Studies on the hydration of tricalcium silicate pastes II. Strength development and fracture characteristics", *Cement and Concrete Research*, v. 3, n. 5, pp. 497–508, sep 1973.

[19] YOUNG, J., BERGER, R., LAWRENCE, F. "Studies on the hydration of tricalcium silicate pastes III. Influence of admixtures on hydration and strength development", *Cement and Concrete Research*, v. 3, n. 6, pp. 689–700, nov 1973.

[20] BROWN, J. H., POMEROY, C. D. "Fracture toughness of cement paste and mortars", *Cement and Concrete Research*, v. 3, n. 4, pp. 475–780, 1973.

[21] MINDESS, S., LAWRENCE, F. V. "The J-Integral as a fracture criterion for fiber reinforced concrete", *Cement and Concrete Research*, v. 7, pp. 731–742, 1977.

[22] KAPLAN, M. F. "Crack Propagation and the Fracture of Concrete", *ACI Journal Proceedings*, v. 58, n. 11, 1961.

[23] MINDESS, S. "Fracture toughness testing of cement and concrete". In: A. Carpinteri et al. (Ed.), *Fracture mechanics of concrete: Material characterization and testing*, Martinus Nijhoff Publishers, cap. 3, pp. 67–110, 1984.

[24] BAZANT, Z. P. "Concrete fracture models: Testing and practice", *Engineering Fracture Mechanics*, v. 69, pp. 165–205, 2002.

[25] RADJY, F., HANSEN, T. C. "Fracture of hardened cement paste and concrete", *Cement and Concrete Research*, v. 3, n. 4, pp. 343–361, 1973.

[26] TAYLOR, H. F. W. *Cement Chemistry*. London, Academic Press Limited, 1990. ISBN: 012683900X.

[27] BERGER, R. L. "Calcium Hydroxide: Its Role in the Fracture of Tricalcium Silicate Paste", *Science*, v. 175, pp. 626–629, 1972.

[28] CROW, J. M. "The concrete conundrum", *Chemistry World*, , n. March, pp. 62–66, 2008. ISSN: 14737604.

[29] WRAY, P. "Straight talk with Karen Scrivener on cements, CO2 and sustainable development", *American Ceramic Society Bulletin*, v. 91, n. 5, pp. 47–50, 2012.

[30] NIXON, P. J. "Recycled concrete as an aggregate for concrete- a review", *Matériaux et Construction*, v. 11, n. 5, pp. 371–378, 1978.

[31] NIXON, P. J. "The use of materials from demolition in construction", *Resources Policy*, v. 2, n. 4, pp. 276–283, 1976.

[32] HANSEN, T. C. "Recycled aggregates and recycled aggregate concrete second state-of-the-art report developments 1945-1985", *Materials and Structures*, v. 19, n. 3, pp. 201–246, 1986.

[33] KEELER, M., BURKE, B. *Fundamentos de Projetos de Edificações Sustentáveis (from the original title: Fundamentals of Integrated Design for Sustainable Building)*. 1 ed. Porto Alegre, Bookman, 2010. ISBN: 9788577807109.

[34] ASTM C33/C33M-13. *Standard Specification for Concrete Aggregates*. Relatório técnico, American Society for Testing and Materials (ASTM International), 2013.

[35] ASTM C125-13B. *Standard terminology Relating to Concrete and Concrete Aggregates*. Relatório técnico, American Society for Testing and Materials (ASTM International), 2013.

[36] ACI COMITTEE 555 (ACI 555R-01). *Removal and Reuse of Hardened Concrete*. Relatório técnico, American Concrete Institute (ACI), 2001.

[37] HANSEN, T. v. 6. 1992. ISBN: 0203626451.

[38] EUROPEAN UNION – BRITE EURAM III. *Recycling lightweight aggregate concrete EuroLightCon Economic Design and Construction with Light Weight Aggregate Concrete*. Relatório técnico, Gouda, June 2000.

[39] B.C.S.J. *Proposed standard for the use of recycled aggregate and recycled aggregate concrete. Committee on Disposal and Reuse of Construction Waste. (English version published in June 1981)*. Relatório técnico, Building Contractors Society of Japan (BCSJ), 1977.

[40] CONAMA. *Resolução nº307. Estabelece diretrizes, critérios e procedimentos para a gestão dos resíduos da construção*. Relatório técnico, Conselho Nacional do Meio Ambiente (National Enviroment Council), Brasilia, 2002.

[41] ABNT NBR 15112. *Construction and demolition wastes - Selection areas - Lines of direction for project, implantation and operation.* Relatório técnico, Associação Brasileira de Normas Técnicas (Technical Standards Brazilian Association), Rio de Janeiro, 2004.

[42] ABNT NBR 15113. *Construction and demolition wastes - Landfills - Lines of direction for project, implantation and operation.* Relatório técnico, Associação Brasileira de Normas Técnicas (Technical Standards Brazilian Association), Rio de Janeiro, 2004.

[43] ABNT NBR 15114. *Construction and demolition wastes - Recycling areas - Lines of direction for project, implantation and operation.* Relatório técnico, Associação Brasileira de Normas Técnicas (Technical Standards Brazilian Association), Rio de Janeiro, 2004.

[44] ABNT NBR 15115. *Recycled aggregates of construction and demolition wastes - Construction of pavement layers - Procedures.* Relatório técnico, Associação Brasileira de Normas Técnicas (Technical Standards Brazilian Association), Rio de Janeiro, 2004.

[45] ABNT NBR 15116. *Recycled aggregate of solid residue of building construtions - Requeriments and methodologies.* Relatório técnico, Associação Brasileira

de Normas Técnicas (Technical Standards Brazilian Association), Rio de Janeiro, 2004.

[46] ABRELEPE. *Panorama dos Resíduos Sólidos no Brasil*. Relatório técnico, Associação brasileira de empresas de limpeza pública e resíduos especiais (International Solid Waste Association in Brazil), 2013.

[47] BRITO, J., ALVES, F. "Concrete with recycled aggregates: the Portuguese experimental research", *Materials and Structures*, v. 43, n. S1, pp. 35–51, 2010.

[48] XIAO, J. Z., LI, J. B., ZHANG, C. "On relationships between the mechanical properties of recycled aggregate concrete: An overview", *Materials and Structures*, v. 39, n. 6, pp. 655–664, 2006.

[49] XIAO, J., LI, W., FAN, Y., et al. "An overview of study on recycled aggregate concrete in China (1996-2011)", *Construction and Building Materials*, v. 31, pp. 364–383, 2012.

[50] LEITE, M. B. *Avaliação de propriedades mecânicas de concretos produzidos com agregados reciclados de resíduos de construção e demolição (in portuguese)*. Doctor thesis, Universidade Federal do Rio Gande do Sul (Federal University of Rio Grande do Sul), 2001.

[51] KATZ, A. "Properties of concrete made with recycled aggregate from partially hydrated old concrete", *Cement and Concrete Research*, v. 33, n. 5, pp. 703–711, 2003.

[52] LARRAÑAGA, M. E. *Experimental study on microstructure and structural behaviour of recycled aggregate concrete*. Doctor thesis, Univertat Politècnica de Catalunya, 2004.

[53] ETXEBERRIA, M., VÁZQUEZ, E., MARÍ, A., et al. "Influence of amount of recycled coarse aggregates and production process on properties of recycled aggregate concrete", *Cement and Concrete Research*, v. 37, n. 5, pp. 735–742, 2007.

[54] EVANGELISTA, L., DE BRITO, J. "Mechanical behaviour of concrete made with fine recycled concrete aggregates", *Cement and Concrete Composites*, v. 29, n. 5, pp. 397–401, 2007.

[55] GOMES, M., BRITO, J. "Structural concrete with incorporation of coarse recycled concrete and ceramic aggregates: durability performance", *Materials and Structures*, v. 42, n. 5, pp. 663–675, 2009.

[56] CACHIM, P. B. "Mechanical properties of brick aggregate concrete", *Construction and Building Materials*, v. 23, n. 3, pp. 1292–1297, 2009.

[57] BERNDT, M. L. "Properties of sustainable concrete containing fly ash, slag and recycled concrete aggregate", *Construction and Building Materials*, v. 23, n. 7, pp. 2606–2613, 2009.

[58] LIMA, P. R. L., LEITE, M. B., SANTIAGO, E. Q. R. "Recycled lightweight concrete made from footwear industry waste and CDW", *Waste Management*, v. 30, n. 6, pp. 1107–1113, 2010.

[59] YANG, J., DU, Q., BAO, Y. "Concrete with recycled concrete aggregate and crushed clay bricks", *Construction and Building Materials*, v. 25, n. 4, pp. 1935–1945, 2011.

[60] KANELLOPOULOS, A., NICOLAIDES, D., PETROU, M. F. "Mechanical and durability properties of concretes containing recycled lime powder and recycled aggregates", *Construction and Building Materials*, v. 53, pp. 253–259, 2014.

[61] KOSHIRO, Y., ICHISE, K. "Application of entire concrete waste reuse model to produce recycled aggregate class H", *Construction and Building Materials*, v. 67, pp. 308–314, 2014.

[62] PEPE, M., TOLEDO FILHO, R. D., KOENDERS, E. A. B., et al. "Alternative processing procedures for recycled aggregates in structural concrete", *Construction and Building Materials*, v. 69, pp. 124–132, 2014.

[63] SCHOON, J., DE BUYSSER, K., VAN DRIESSCHE, I., et al. "Fines extracted from recycled concrete as alternative raw material for Portland cement clinker production", *Cement and Concrete Composites*, v. 58, pp. 70–80, 2015.

[64] RIBAS, L., CORDEIRO, G. C., TOLEDO FILHO, R. D., et al. "Measuring the strength of irregularly-shaped fine particles in a microcompression tester", *Minerals Engineering*, v. 65, pp. 149–155, 2014.

[65] RIBAS, L. F. *Influência da cominuição da fração cerâmica dos residuos de construcão e demolicão na sua atividade pozolânica e nas propriedades físicas, mecânicas e durabilidade de argamassas de cimento*. Doctor thesis, Universidade Federal do Rio de Janeiro, 2014.

[66] O'FARRELL, M., WILD, S., SABIR, B. "Pore size distribution and compressive strength of waste clay brick mortar", *Cement and Concrete Composites*, v. 23, n. 1, pp. 81–91, 2001.

[67] AMORIM, L. V., LIRA, H. L., FERREIRA, H. C. "Use of Residential Construction Waste and Residues from Red Ceramic Industry in Alternative Mortars", *Journal of Environmental Engineering*, v. 129, n. 10, pp. 916–920, 2003.

[68] GONÇALVES, J. P., FILHO, R. D. T., FAIRBAIRN, E. D. M. R. "Estudo da hidratação de pastas de cimento Portland contendo resíduo cerâmico por meio de análise térmica", *Ambiente Construído*, v. 6, n. 4, pp. 83–94, 2006.

[69] PUERTAS, F., GARCÍA-DÍAZ, I., BARBA, A., et al. "Ceramic wastes as alternative raw materials for Portland cement clinker production", *Cement and Concrete Composites*, v. 30, n. 9, pp. 798–805, 2008.

[70] PACHECO-TORGAL, F., JALALI, S. "Reusing ceramic wastes in concrete", *Construction and Building Materials*, v. 24, pp. 832–838, 2010.

[71] DE OLIVEIRA, L. A. P., CASTRO-GOMES, J. P., SANTOS, P. M. "The potential pozzolanic activity of glass and red-clay ceramic waste as cement mortars components", *Construction and Building Materials*, v. 31, pp. 197–203, 2012.

[72] SILVA, J., DE BRITO, J., VEIGA, R. "Incorporation of fine ceramics in mortars", *Construction and Building Materials*, v. 23, n. 1, pp. 556–564, 2009.

[73] AHMARI, S., REN, X., TOUFIGH, V., et al. "Production of geopolymeric binder from blended waste concrete powder and fly ash", *Construction and Building Materials*, v. 35, pp. 718–729, 2012.

[74] CHEN, M., LIN, J., WU, S. "Potential of recycled fine aggregates powder as filler in asphalt mixture", *Construction and Building Materials*, v. 25, n. 10, pp. 3909–3914, 2011.

[75] MARCUS, H. L., SIH, G. C. "A crackline-loaded edge-crack stress corrosion specimen", *Engineering Fracture Mechanics*, v. 3, n. 4, pp. 453–461, 1971.

[76] GALLAGHER, J. P. "Experimentally determined stress intensity factors for several contoured double cantilever beam specimens", *Engineering Fracture Mechanics*, v. 3, n. 1, pp. 27–43, 1971.

[77] DAVALOS, J. F., MADABHUSI-RAMAN, P., QIAO, P. Z., et al. "Compliance rate change of tapered double cantilever beam specimen with hybrid interface bonds", *Theoretical and Applied Fracture Mechanics*, v. 29, n. 2, pp. 125–139, 1998.

[78] COUREAU, J.-L., MOREL, S., DOURADO, N. "Cohesive zone model and quasibrittle failure of wood: A new light on the adapted specimen geometries for fracture tests", *Engineering Fracture Mechanics*, v. 109, n. 0, pp. 328–340, 2013.

[79] QIAO, P., WANG, J., DAVALOS, J. F. "Tapered beam on elastic foundation model for compliance rate change of {TDCB} specimen", *Engineering Fracture Mechanics*, v. 70, n. 2, pp. 339–353, 2003.

[80] BLACKMAN, B. R. K., HADAVINIA, H., KINLOCH, A. J., et al. "The calculation of adhesive fracture energies in mode I: revisiting the tapered double cantilever beam (TDCB) test", *Engineering Fracture Mechanics*, v. 70, n. 2, pp. 233–248, 2003.

[81] FMC, R. T.-. "Determination of Fracture Energy of Mortar and Concrete by Means of Three-Point Bend Tests on Notched Beams." *Materials and Structures*, v. 18, n. 106, pp. 285–290, 1985.

[82] MOREL, S., DOURADO, N., VALENTIN, G., et al. "Wood: A quasi-brittle material. R-curve behavior and peak load evaluation", *Int. J. Frac.*, v. 131, pp. 385–400, 2005.

[83] HILLEMEIER, B., HILSDORF, H. K. "Fracture mechanics studies on concrete compounds", *Cement and Concrete Research*, v. 7, pp. 523–536, 1977.

[84] NARA, Y., KOIKE, K., YONEDA, T., et al. "Relation between subcritical crack growth behavior and crack paths in granite", *Int. J. Rock Mech. Min. Sci.*, v. 43, pp. 1256–1261, 2006.

[85] ASTM E1820-15A. *Standard test method for measurement of fracture toughness*. Relatório técnico, American Society for Testing and Materials (ASTM International), 2015.

[86] E399-12E3, A. *Standard Test Method for Linear-Elastic Plane-Strain Fracture Toughness KIc of Metallic Materials*. Relatório técnico, American Society for Testing and Materials (ASTM International), 2013.

[87] ISO 7539-6. *Corrosion of metals and alloys – Stress corrosion testing – Part 6: Preparation and use of precracked specimens for tests under constant load*

or constant displacement. Relatório técnico, International Organization for Standardization (ISO), Geneva, 2011.

[88] ASTM E647-15E1. Relatório técnico.

[89] SHYAM, A., LARA-CURZIO, E. "The double-torsion testing technique for determination of fracture toughness and slow crack growth behavior of materials: A review", *Journal of Materials Science*, v. 41, n. 13, pp. 4093–4104, 2006.

[90] ATKINSON, B. K. "Subcritical crack growth in geological materials", *J. Geophys. Res.*, v. 89, pp. 4077–4114, 1984.

[91] NARA, Y., KANEKO, K. "Study of subcritical crack growth in andesite using the double torsion test", *Int. J. Rock. Mech. Min. Sci.*, v. 42, pp. 521–530, 2005.

[92] SWANSON, P. L. "Subcritical crack propagation in Westerly granite an investigation into the double torsion test", *Int. J. Rock Mech. Min. Sci. Geomech. Abs.*, v. 18, pp. 445, 1981.

[93] EVANS, A. G. "A method for evaluating the time-dependent failure characteristics of brittle materials and its application to polycrystalline alumina", *J. Mater. Sci.*, v. 15, pp. 1137–1146, 1972.

[94] ISO 15024. *Fibre-reinforced plastic composites — Determination of mode I interlaminar fracture toughness, GIC, for unidirectionally reinforced materials*. Relatório técnico, International Organization for Standardization (ISO), Geneva, 2001.

[95] HASHEMI, S., KINLOCH, A. J., WILLIAMS, J. G. "The Analysis of Interlaminar Fracture in Uniaxial Fibre-Polymer Composites", *Proceedings of the Royal Society of London A: Mathematical, Physical and Engineering Sciences*, v. 427, n. 1872, pp. 173–199, 1990.

[96] BLACKMAN, B. R. K., DEAR, J. P., KINLOCH, A. J., et al. "The failure of fibre composites and adhesively bonded fibre composites under high rates of test", *Journal of Materials Science*, v. 30, n. 23, pp. 5885–5900, 1995.

[97] BLACKMAN, B. R. K., HADAVINIA, H., KINLOCH, A. J., et al. "The use of a cohesive zone model to study the fracture of fibre composites and adhesively-bonded joints", *International Journal of Fracture*, v. 119, n. 1, pp. 25–46, 2003.

[98] RIPLING, E. J., MOSTOVOY, S., CORTEN, H. T. "Fracture Mechanics: A Tool for Evaluating Structural Adhesives", *The Journal of Adhesion*, v. 3, n. 2, pp. 107–123, 1971.

[99] NEERHOFF, A. "Correlation between fracture toughness and zeta potential of cement stone". In: Kreijger, P. C. (Ed.), *Proceedings of the NATO Advanced Research Institute, Adhesion Problems in the Recycling of Concrete*, pp. 267–284, Saint-Remy-Les-Chevreuse, 1981. Plenum Publishing Corp.

[100] WILLIAMS, J. G. *Fracture mechanics of polymers*. Ellis Horwood series in engineering science. E. Horwood, 1984. ISBN: 9780853126850.

[101] MOREL, S., MOUROT, G., SCHMITTBUHL, J. "Influence of the specimen geometry on R-curve behavior and roughening of fracture surfaces", *Int. J. Frac.*, v. 121, pp. 23–42, 2003.

[102] LIEBOWITZ, H. Vol. 5 ed. New York, Academic, 1969.

[103] CASTEM. "CASTEM, a Finite Element package developed by CEA, FRANCE". .

[104] EWALDS, H. L., WANHILL, R. J. H. *Fracture Mechanics*. Edward Arnold Limited, 1985.

[105] MARSHALL, G. P., COUTTS, L. H., WILLIAMS, J. G. "Temperature effects in the fracture of PMMA", *J. Mater. Sci.*, v. 9, pp. 1409–1419, 1974.

[106] CHARLES, R. J. "Static fatigue of glass II", *J. Appl. Phys.*, v. 29, pp. 1554–1560, 1958.

[107] ROUX, S., HILD, F. "Stress intensity factor measurements from digital image correlation: Post-processing and integrated approaches", *International Journal of Fracture*, v. 140, n. 1-4, pp. 141–157, 2006.

[108] RÉTHORÉ, J., ROUX, S., HILD, F. "An extended and integrated digital image correlation technique applied to the analysis of fractured samples. The equilibrium gap method as a mechanical filter", *European Journal of Computational Mechanics*, v. 18, n. 3-4, pp. 285–306, 2009.

[109] CHU, T., RANSON, W., SUTTON, M. "Applications of digital-image-correlation techniques to experimental mechanics", *Experimental Mechanics*, v. 25, n. 3, pp. 232–244, 1985.

[110] SUTTON, M., MINGQI, C., PETERS, W., et al. "Application of an optimized digital correlation method to planar deformation analysis", *Image and Vision Computing*, v. 4, n. 3, pp. 143–150, 1986.

[111] RÉTHORÉ, J. "Automatic crack tip detection and stress intensity factors estimation of curved cracks from digital images", v. 103, n. 7, pp. 516–534, aug 2015.

[112] WILLIAMS, M. L. "On the Stress Distribution at the Base of a Stationary Crack", *Journal of Applied Mechanics*, v. 24, n. 3, pp. 109–114, 1957.

[113] MATHIEU, F., HILD, F., ROUX, S. "Identification of a crack propagation law by digital image correlation", *International Journal of Fatigue*, v. 36, pp. 146–154, 2012.

[114] MATHIEU, F., HILD, F., ROUX, S. "Image-based identification procedure of a crack propagation law", *Engineering Fracture Mechanics*, v. 103, pp. 48–59, 2013.

[115] HENNINGER, C., ROUX, S., HILD, F. "Enriched kinematic fields of cracked structures", *International Journal of Solids and Structures*, v. 47, n. 24, pp. 3305–3316, 2010.

[116] COTTERELL, B., RICE, J. R. "Slightly curved or kinked cracks", *Int. J. Frac.*, v. 16, pp. 155–169, 1980.

[117] GOL'DSTEIN, R. V., SALGANIK, R. L. "Brittle fracture of solids with arbitrary cracks", *Int. J. Frac.*, v. 10, pp. 507–523, 1974.

[118] KATZAV, E., ADDA-BEDIA, M. "Stability and roughness of tensile cracks in disordered materials", *Phys. Rev. E*, v. 88, pp. 052402, 2013.

[119] HILD, F., ROUX, S. "Comparison of Local and Global Approaches to Digital Image Correlation", *Experimental Mechanics*, v. 52, n. 9, pp. 1503–1519, 2012.

[120] ABNT NBR 9831. *Oil well cements - Specification and test methods*. Relatório técnico, Associação Brasileira de Normas Técnicas (Technical Standards Brazilian Association), Rio de Janeiro, 2008.

[121] ISO 10426-1. *Petroleum and natural gas industries — Cements and materials for well cementing — Part 1: Specification*. Relatório técnico, International Organization for Standardization (ISO), Geneva, 2009.

[122] VAZ, A. P. R. *Comportamento de vigas reforçadas submetidas a carregamento cíclico*. Phd thesis, Federal University of Rio de Janeiro, 2013.

[123] FERREIRA, J., GRABOIS, T., CALCADO, G., et al. "Stress-strain behavior of mortar mixtures containing construction and demolition waste as fine aggregate", *Key Engineering Materials*, v. 634, pp. 300–306, 2015.

[124] ABNT NBR 7211. *Aggregates for concrete - Specification*. Relatório técnico, Associação Brasileira de Normas Técnicas (Technical Standards Brazilian Association), Rio de Janeiro, 2009.

[125] ABNT NBR 5737. *Sulphate resistent Portland cements - Specification*. Relatório técnico, Associação Brasileira de Normas Técnicas (Technical Standards Brazilian Association), Rio de Janeiro, 1992.

[126] MONTGOMERY, D. C. *Design and analysis of experiments.* New York, Wiley, 1997.

[127] MEHTA, P. K., MONTEIRO, P. J. M. *Concrete: microstructure, properties, and materials*. 2006. ISBN: 0071589198.

[128] ISO 15901-1. *Evaluation of pore size distribution and porosity of solid materials by mercury porosimetry and gas adsorption - Part 1: Mercury porosimetry*. Relatório técnico, International Organization for Standardization (ISO), Geneva, 2016.

[129] WASHBURN, E. W. "The Dynamics of Capillary Flow", *Phys. Rev.*, v. 17, pp. 273–283, Mar 1921.

[130] NEVILLE, A. M. *Properties of Concrete*, v. Fourth. 2000. ISBN: 9780470235270.

[131] GASTALDI, D., CANONICO, F., CAPELLI, L., et al. "An investigation on the recycling of hydrated cement from concrete demolition waste", *Cement and Concrete Composites*, v. 61, pp. 29–35, 2015.

[132] EVANS, A. G. "Perspective on the Development of High-Toughness Ceramics", *Journal of American Ceramic Society*, v. 73, n. 2, pp. 187–206, 1990.

[133] ACI318-02. Relatório técnico, American Concrete Institute (ACI).

[134] OLOUKUN, F. A. "Prediction of concrete tensile strength from compressive strength: evaluation of existing relations for normal weigt", *ACI Materials Journal*, v. 88, pp. 302–309, 1991.

Appendix A

An extension in the IDIC algorithm for out-of-plane motions

In this appendix, we will give some complementary information about our study with the Integrated DIC approach. More precisely, our goal is to present one solution for two particular question that arose from empirical observations during the validation of the experiments on PMMA specimens: Is the sample rotates along an axis perpendicular to the optical one (*i.e.* it tilt rotates)? Is it translates out-of-plane along the optical axis? We will see in this section that these motions are possible, indeed. The assumption of a flat target (specimen surface) is used, though the same mathematical and numerical approaches as for in-plane (2D) displacements are kept since only small displacement magnitudes are considered.

The necessity to take into account rigid body motions (RBM) related to the camera coordinates system comes mainly from two particular facts about the experimental procedure: (i) the specimen is attached to the machine test by steel grips at only two points in the same side extremity close to the boundary (see Fig. 2.10); (ii) the specimen's thickness is 8 mm while the space between the arms of these grips (devoted hold the specimen) is 25 mm. In general, what may occur is the sliding of the specimen trough the pins that are connecting it to the grips, thus providing out-of-plane motions along the axes normal to the optical one $\underline{z}$.

In the present case, the IDIC approach for 2D cases displayed in chapter 2 is extended. Therefore, the displacement fields keep being computed as a combination of shape functions, though the general idea here is to just add extra modes corresponding to translations and rotations of the target along the coordinate system of the camera - $\underline{x}$, $\underline{y}$, $\underline{z}$. As the main approach (*i.e.* IDIC code) have already taken into account the rigid body translations in $\underline{\mathrm{x}}$ and $\underline{\mathrm{y}}$ as well as the rigid body rotation in $\underline{\mathrm{z}}$ (see description in section 2.4), our job here is to introduce the shape functions corresponding to one $\underline{\mathrm{z}}$ translation T_z and two ($\underline{\mathrm{x}}$ and $\underline{\mathrm{y}}$) tilt rotations R_x and R_y as presented in Fig. A.1.

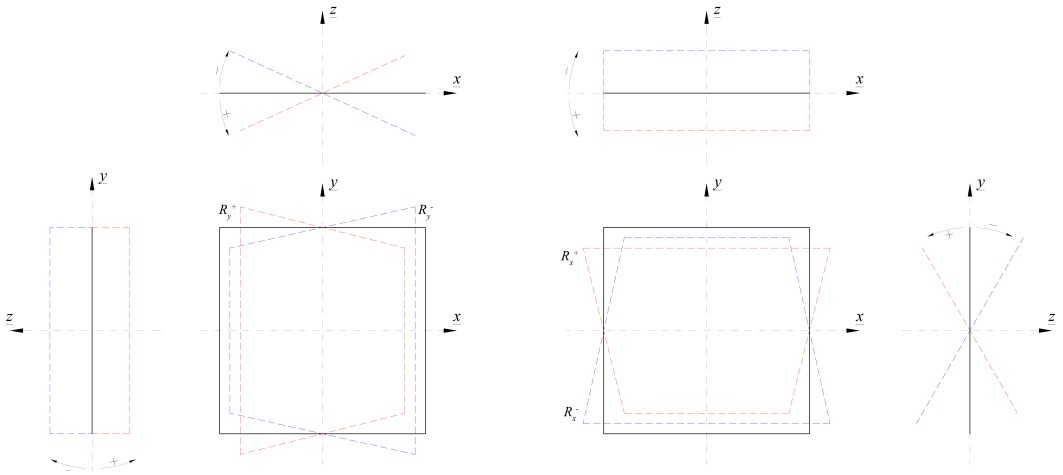

Figure A.1: Description of the tilt rotations of a flat surface along y (right) and x (left). R^+ and R^- denotes the positive and negative angle region, respectively.

Let us first introduce the simple expression of the function for the out-of-plane translation of the target surface perpendicular to the optical axis z

$$\Psi_i = x \cdot \underline{x} + y \cdot \underline{y} \tag{A.1}$$

Now, considering the two rotations along the axes normal to z, one induces displacements of the target in both x and y, which gives - in theory - some complexity to the shape functions. For instance, Figure A.1 illustrates it for both cases of R_x and R_y (*i.e.* rotation along x and y). If we take as an example the tilt rotations along y, although one observes a monotonic relation between the displacements and the angle in y, along x, this is no longer true. Therefore, to describe the increments of displacement in y we use two shape functions:

$$\Psi_i^- = -x^2 \cdot \underline{x} - xy \cdot \underline{y} \tag{A.2}$$

for the surface target in the negative angle region and

$$\Psi_i^+ = x^2 \cdot \underline{x} - xy \cdot \underline{y} \tag{A.3}$$

when the target is in the positive angle region. Then, analogously for displacements in x we have

$$\Psi_i^- = -y^2 \cdot \underline{y} - xy \cdot \underline{x} \tag{A.4}$$

and

$$\Psi_i^- = y^2 \cdot \underline{y} - xy \cdot \underline{x} \tag{A.5}$$

Thus, the description of all rigid body motions along the system coordinates of the camera is completed by the five shape functions depicted above. It is worth recalling

the Eq. 2.21, which is truncated between $n = p_i$ and p_f to be solved numerically, to explain that in this particular case we just add these extra modes to the truncation of the series.

Appendix B

Mix-design and mechanical characteristics of the recycled concrete beam

This appendix is devoted to give some complementary information about the structural concrete beams that were used to produce recycled aggregates and the supplementary cementitious material adopted in this work. These beams were studied in 2013 by Vaz [122] and all the data presented below is extracted from the the cited author. Our interest here is just give the general information about the mix-design and mechanical performance with respect to compressive and splinting tensile strength under static and cyclic loading conditions. Thus, to emphasize what type of material were included in the cement pastes developed in this work.

Figure B.1: Beam production phases. From left to right: first, the regular prismatic beam; the reinforcement casting procedure; and finally, the strengthened beam completed (courtesy of Vaz [122]).

The concrete beam was produced in two phases: A regular prismatic beam followed by an external reinforcement (Figure B.1). Both phases were designed to 30 MPa compressive strength and slump flow of 50 mm (± 10) with water-cement ratio of 0.6 and a mass content ratio of 1 : 2.71 : 3.58 (cement : fine aggregate : coarse aggregate). The mix-design composition is presented in Table B.1.

Table B.1: Concrete mix proportions of reinforced beams in kg/m^3. Different aggregate size classes were used in each phase. Coarse aggregate with D_{max} of 9.5 mm (CA1) in beam phase, and coarse aggregate of D_{max} = 19 mm (CA2) in reinforced phase. Fine aggregates (FA) were the same for both phases. Data is a courtesy of Vaz [122].

Production phases	Materials (kg/m^3)				
	Cement	CA1	CA2	FA	Water
Beam phase	300	-	1074	814	180
Reinforced phase	300	1074	-	814	180

Table B.3 presents the mechanical behavior (compressive strength – f_c, and splitting tensile strength - f_{ct}) of concrete at the initial static condition of beams without reinforcement. In the case of reinforced beams when submitted to load up to failure, Table A.3 shows the elastic modulus (E) as well and the mechanical properties related to the reinforcement phase.

Table B.2: Initial static properties of he concrete beams (courtesy of Vaz [122]).

Beam specimens	B1	B2	B3	B4	B5	B6
Ages (days)	60	60	37	37	30	37
f_c (MPa)	33.7	34.1	30.6	32.3	36.1	35.9
f_{ct} (MPa)	3.47	3.42	3.49	3.65	3.35	3.49

Table B.3: Concrete properties when reinforced beams were submitted to cyclic load and failure (courtesy of Vaz [122]).

Beam specimens	Beam phase					
	B1	B2	B3	B4	B5	B6
Ages (days)	677	295	123	183	192	208
f_c (MPa)	33.9	34.1	33.5	33.4	36.1	36.2
E (GPa)	25.2	25.8	25.1	24.8	27.4	27.6
f_{ct} (MPa)	3.61	3.49	3.56	3.68	3.64	3.65
Beam specimens	Reinforced phase					
	B1	B2	B3	B4	B5	B6
Ages (days)	543	135	75	135	116	132
f_c (MPa)	33.1	34.0	33.3	33.2	34.1	34.3
f_{ct} (MPa)	3.54	3.59	3.58	3.65	3.54	3.56

Appendix C

Publications

Publications following from thesis chapters:

(i) Ponson L., Grabois, T.M., Vasudevan, A.V., Cordeiro, G.C., Filho, R.D.T. A new simple geometry for the analysis of Mode-I tensile fracture. *In progress*, to be submitted to International Journal of Solids and Structures.

(ii) Grabois, T.M., Cordeiro, G.C., Filho, R.D.T. Hydration properties of recycled cement pastes. *In progress*, to be submitted to Cement and Concrete Research.

(iii) Ferreira, J.C., Grabois, T.M., Calcado, G.C.S., Filho, R.D.T. (2015). Stress-strain behavior of mortar mixtures containing construction and demolition waste as fine aggregate. Key Engineering Materials, 634, 300–306.

Other published work:

- Pepe, M., Grabois, T.M., Silva, M.A., Tavares, L.M., Filho, R.D.T. Mechanical characterization of lightweight, recycled and natural coarse aggregates using single-particle slow compression test. Submitted to *Materiales de Construcción*, August 13th, 2016.
- Grabois, T.M., Cordeiro, G.C., Filho, R.D.T. (2016). Fresh and hardened-state properties of self-compacting lightweight concrete reinforced with steel fibers. Construction and Building Materials, 104, 284–292.
- Grabois, T.M., Cordeiro, G.C., Filho, R.D.T. (2013). Mechanical Characterization of Self-Compacting Lightweight Concrete. Concrete Plant International (Print), 6, 146-153.